Aperture Array Photonic Metamaterials: Theoretical approaches, numerical techniques and a novel application

by

Eli Lansey

A dissertation submitted to the Graduate Faculty in Physics in partial fulfillment of the requirements for the degree of Doctor of Philosophy, The City University of New York.

2012

This manuscript has been read and accepted for the Graduate Faculty in Physics in satisfaction of the dissertation requirements for the degree of Doctor of Philosophy.

Prof. David T. Crouse

Date

Chair of Examining Committee

Prof. Igor L. Kuskovsky

Date

Executive Officer

Prof. Ronald L. Koder

Prof. Frederick W. Smith

Prof. Azriel Z. Genack

Prof. Michael A. Fiddy

Supervisory Committee

THE CITY UNIVERSITY OF NEW YORK

Abstract

Aperture Array Photonic Metamaterials: Theoretical approaches, numerical techniques and a novel application

by

Eli Lansey

Advisor: Prof. David T. Crouse

Optical or photonic metamaterials that operate in the infrared and visible frequency regimes show tremendous promise for solving problems in renewable energy, infrared imaging, and telecommunications. However, many of the theoretical and simulation techniques used at lower frequencies are not applicable to this higher-frequency regime. Furthermore, technological and financial limitations of photonic metamaterial fabrication increases the importance of reliable theoretical models and computational techniques for predicting the optical response of photonic metamaterials.

This thesis focuses on aperture array metamaterials. That is, a rectangular, circular, or other shaped cavity or hole embedded in, or penetrating through a metal film. The research in the first portion of this dissertation reflects our interest in developing a fundamental, theoretical understanding of the behavior of light's interaction with these aperture arrays, specifically regarding enhanced optical transmission. We develop an approximate boundary condition for metals at optical frequencies, and a comprehensive, analytical explanation of the physics underlying this effect. These theoretical analyses are augmented by computational techniques in the second portion of this thesis, used both for verification of the theoretical work, and solving more complicated structures. Finally, the last portion of this thesis discusses the results from designing, fabricating and characterizing a light-splitting metamaterial.

To my parents

Lill and Bob Lansey

for always encouraging me to ask questions

Acknowledgements

יראת ה׳ ראשית דעת [משלי א:ז] – תודה ושבח לא־ל בורא עולם!

There are many people who deserve my thanks for their help and assistance in achieving this milestone. My wife has put up with a lot during my educational adventures, especially over the last few months when I was writing this dissertation. Thank you, Stacy, for your love, exceptional patience, and constant encouragement. If I didn't have you cheering me along this whole time, I'm not sure I would have made it. To my sons, Moshe and Chanan, thank you for being there with a smile (or cry) to remind me about what's really important. To my parents, thank you for always encouraging, challenging, and believing in me; this thesis is truly a reflection of your efforts. I am fortunate to have two younger (although, taller) brothers, Yoni and Aryeh, who have always been happy to hear me explain my work, and offered helpful ideas at every stage. To my brothers, extended family and friends, thank you for all your support, love and friendship.

I would especially like to thank my advisor, Dr. David Crouse, for his mentoring me the three years I was in his group. I feel very fortunate to have studied under an expert of his caliber, and to have been part of such a diverse, exciting, and well-funded research group. I benefited greatly from his advice and expertise.

Much of the work in this dissertation came about through extensive collaboration with other students and researchers. To that end, I would like to thank my fellow graduate students, Amara, Isroel, Nafiseh, and Young, as well as all the other undergraduate and masters students and engineers, especially Amandeep, Daniel, Hannah, and Igor, for their friendship and help. It's been fun working (and grumbling) with all of you. The project described in this thesis was developed in conjunction with an extremely talented group of people at Phoebus Optoelectronics. Thank you Tom, Jonah, Chris, Roman, Boyan, Mike, and Ron. Additionally, thanks to the lab's support staff, Andrii, Kerry, and Martin, for your insights, organization, and help. The microwave structure described in Chapter 9 was fabricated and characterized by Ian Hooper in the research group of Alastair Hibbins at the Electromagnetics Materials Laboratory at the University of Exeter; I am extremely appreciative of his hard work.

I am grateful to my new employer, Riverside Research, for allowing me a flexible schedule to complete my doctoral research and write this thesis. I look forward to starting a full schedule soon.

The work described in Chapters 3, 5, 7, and 8 was supported in part by the Department of Defense (DOD)/Defense Advanced Research Projects Agency (DARPA) Small Business Innovation Research (SBIR) Program under Contract No. W31P4Q-10-C-0074. The material in Chapters 4 and 9 was supported in part by the DOD/DARPA SBIR Program under Contract No. W31P4Q-11-C-0238. The views, opinions, and/or findings contained in this article/presentation are those of the author/presenter and should not be interpreted as representing the official views or policies, either expressed or implied, of the Defense Advanced Research Projects Agency or the Department of Defense. It has been approved for public release, distribution unlimited. The work in Chapter 8 was carried out in part at the Center for Functional Nanomaterials, Brookhaven National Laboratory, which is supported by the U.S. Department of Energy, Office of Basic Energy Sciences, under Contract No. DE-AC02-98CH10886. Computational support for this work was provided by the CUNY Center for Advanced Technology's high performance computing cluster. The material in Chapter 9 was also supported in part by the Air Force Office of Scientific Research (AFOSR) Bioenergy project (FA9550-10-1-0350), the NSF Industry/University Cooperative Research Center for Metamaterials (IIP-1068028) and its Industry Advisory Board (IAB) members, and the EPSRC, UK funding through the QUEST project (ref: EP/I034548/1).

Contents

List of Tables

List of Figures

Chapter 1

Introduction

Metamaterials are artificially constructed materials whose extraordinary optical characteristics are primarily due to their structure, not their inherent material properties. That is, the particulars of a material's shape or periodicity, for example, have a greater influence on its optical behavior than its intrinsic, bulk physical properties, such as its conductivity or dielectric constant. The response of metamaterials are typically strongly dependent on frequency, angle of incidence, and polarization, and give rise to unique and interesting effects.

For example, materials such as photonic crystals artificially create an electronic band structure.[1, 2] Split ring resonators have allowed creation of negative index materials,[3, 4] and tunable response structures when combined with liquid crystals.[5,6] Recently, "cloaking" metamaterials have been demonstrated.[7–10] Light can be forced to weave around a structure,[11] split into different beams,[12,13] and even be focused as if by a “superlens.”[14–16] Finally, the transmission of light through subwavelength apertures in metal is enhanced with a periodic array.[17] These novel materials have applications in photonics, telecommunications, sensing, and countless other areas.

Until fairly recently, most metamaterial research involved structures responsive to microwave or low terahertz radiation. This is primarily due to the simplicity and relatively low cost of fabrication, and ease of modeling. The smallest feature sizes of metamaterial structures are typically on the order of magnitude of one-tenth of the wavelength. For microwave radiation, that is in the millimeter to centimeter range, and these structures can be made utilizing simple photo-lithography techniques originally designed for producing printed circuit boards, or milled out of metal using computer numerical control (CNC) machines. Even at low terahertz frequencies, the smallest length scale is on the order of 10-100 microns, which can still easily be made by ordinary photo-lithography.

Furthermore, at these frequencies most metals are excellent conductors. This makes it easy to theoretically and computationally model the structures and their ultimate optical response. The ease of simulation coupled with simplicity and affordability of fabrication has made microwave and terahertz metamaterials one of the most active areas of physics research.

However, for infrared (IR) and visible frequencies, the smallest lengths are on the order of 10 nm to 1 micron, which leads to devices are significantly more difficult and expensive to fabricate as compared the microwave structures. Typically, initial fabrication of these structures is via electron-beam lithography which is notoriously slow and expensive, or cutting-edge interference/holographic lithography which, while cheaper, is very limited in the type of structures which can be made. These technological and financial limitations increase the importance of reliable theoretical models and computational techniques for predicting the optical response of photonic metamaterials.

Furthermore, at these higher frequencies, the properties of metals are drastically different from lower frequencies. Metals no longer behave as nearly-perfect conductors; the optical color response of metals reflects this change, which is why gold *looks* different than silver, see Fig. 1.1. Furthermore, electromagnetic fields can penetrate metals with skin depths that are closer to the characteristic lengths of the optical structures. Therefore, many of the theoretical and simulation techniques used at lower frequencies are not applicable to this higher-frequency regime.

Nevertheless, optical or photonic metamaterials, which operate in the IR and visible frequency regimes, show tremendous promise for solving problems

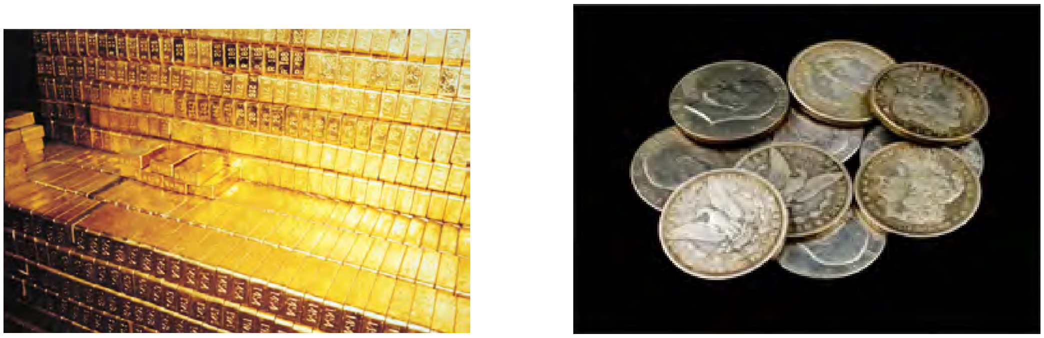

(a) Gold.[18]

(b) Silver.[19]

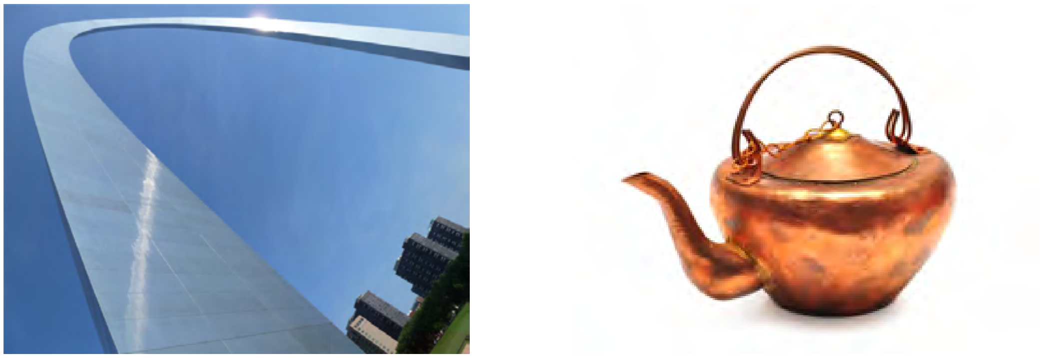

(c) Stainless steel.[20]

(d) Copper.[19]

Figure 1.1: The optical response of a few metals at visible wavelengths.

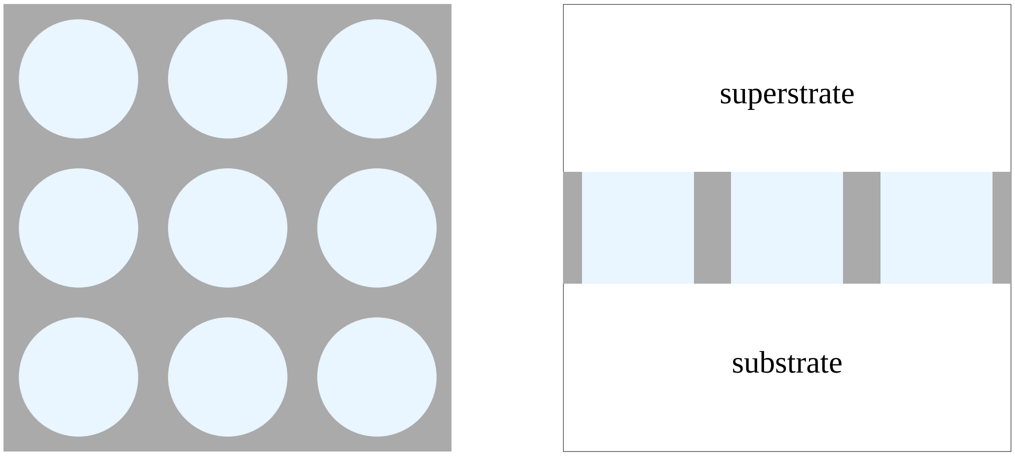

(a) Top-down view of a sample aperture array structure.

(b) Cross section of a sample aperture array structure.

Figure 1.2: Schematic of a sample aperture array structure from top down (a) and in cross section (b). The gray region represents the metal, and the light blue regions are the dielectric-filled apertures, and the white is the superstrate and substrate.

in renewable energy, imaging, defense, and telecommunications. Because of the cost of fabrication, the wide variety of applications, and the fundamentally interesting nature of their optical effects, it is important to have theoretical and computational approaches to understanding the behavior of these materials.

The class of metamaterials this dissertation primarily discusses are subwavelength aperture structures. These materials consist of metal films embedded or perforated with apertures or cavities which can be filled with dielectric materials, see Fig. 1.2 for a sample schematic. Individual apertures can be arranged in a periodic array, forming an "aperture array" metamaterial. The region above the metal film is termed the superstrate, and the region below the film (for apertures) is called the substrate.

The research presented in this thesis was motivated by our research group's interest in developing a horizontally oriented multi-junction solar cell. This device uses an aperture array metamaterial structure to spectrally and spatially split and concentrate light of different bandwidths into different physical regions of the material. Each of these regions can then be filled with an absorbing material whose absorption characteristics matches that of the cavity resonance. We discuss this application in greater depth in Chapter 7.

The research in the first portion of this dissertation reflects our interest in developing a fundamental, theoretical understanding of the behavior of light's interaction with these aperture arrays, specifically regarding enhanced optical transmission (EOT).[1] We outline the general physical and mathematical framework used in the remainder of this thesis in Chapter 2. These results are used in developing an approximate skin depth boundary condition (SDBC) for metals at optical frequencies, discussed in Chapter 3. The text there is largely based on work published in a paper and conference

---

[1] Enhanced optical transmission is often termed "extraordinary optical transmission" or "anomalous optical transmission". For the purposes of this thesis, these terms are interchangeable.

proceedings.[21, 22] We then develop an effective cavity resonance (ECR) model for EOT in Chapter 4, which is a comprehensive, analytical explanation of the physics underlying EOT through aperture arrays. This portion of the text is largely based on work submitted to Physical Review B. These theoretical analyses are augmented by computational techniques, both for comparison to our theoretical work and for solving more complicated structures. We develop a rigorous coupled wave analysis (RCWA) in Chapter 5 for calculating the optical response of aperture arrays, and in Chapter 6 we show how to adapt traditional finite element simulation techniques for simulating these structure in the optical regime. Finally, Chapter 7 discusses our goal of developing a light splitting and concentrating metamaterial for solar energy applications. One approach, ultimately limited in applicability, is discussed in Chapter 8, and another, more promising approach is described in Chapter 9. This former chapter is based in part on conference proceedings,[23] and the last chapter is largely based on work submitted to Optics Express.

Chapter 2

Summary of relevant physics

In this chapter we lay out a general physical and mathematical construct that will be used in the rest of this thesis.

2.1 From Maxwell's equations to a wave equation

The behavior of electromagnetic (EM) waves is governed by Maxwell's equations, a set of four, coupled differential equations, which relate the electric field, $\mathbf{E}$, and the magnetic induction, $\mathbf{B}$. For the remainder of this thesis we will assume that all materials are linear, isotropic, and, unless otherwise specified, non-dispersive. Furthermore, we neglect any magnetic effects, taking the permeability $\mu = 1$ for all materials. This allows us to use the macroscopic field quantities,[24]

$$\mathbf{D} = \epsilon\mathbf{E} \tag{2.1a}$$

$$\mathbf{H} = \mathbf{B} \tag{2.1b}$$

where, **D** is the electric displacement, ϵ is a material's dielectric constant, and **H** is the magnetic field. Note that here, and throughout this dissertation, unless otherwise specified, we use Gaussian (CGS) units for all quantities.

Maxwell's equations, in macroscopic form, are

$$\nabla \cdot \mathbf{D} = 4\pi\rho_{\text{free}} \tag{2.2a}$$

$$\nabla \cdot \mathbf{H} = 0 \tag{2.2b}$$

$$\nabla \times \mathbf{E} = -\frac{1}{c}\frac{\partial \mathbf{B}}{\partial t} \tag{2.2c}$$

$$\nabla \times \mathbf{H} = \frac{4\pi}{c}\mathbf{J}_{\text{free}} + \frac{1}{c}\frac{\partial \mathbf{D}}{\partial t}, \tag{2.2d}$$

where ρ_{free} is the free charge density and $\mathbf{J}_{\text{free}}$ is the free current density.[24] Both of these quantities are assumed to be zero for the situations we analyze. We further assume an implicit $\exp[-i\omega t]$ harmonic time dependence, i.e. a EM wave, where ω is the (angular) frequency. This allows us to simplify

Eqs. 2.2,

$$\nabla \cdot \mathbf{E} = 0 \tag{2.3a}$$

$$\nabla \cdot \mathbf{H} = 0 \tag{2.3b}$$

$$\nabla \times \mathbf{E} = i\kappa_0 \mathbf{H} \tag{2.3c}$$

$$\nabla \times \mathbf{H} = -i\epsilon\kappa_0 \mathbf{E}, \tag{2.3d}$$

where

$$\kappa_0 \equiv \frac{\omega}{c}. \tag{2.4}$$

Taking the curl of Eq. 2.3c, making use of vector identities and substituting Eqs. 2.3d and 2.3a gives

$$\left(\nabla^2 + \epsilon\kappa_0^2\right) \mathbf{E} = 0. \tag{2.5a}$$

Similarly, taking the curl of Eq. 2.3d, making use of vector identities and substituting Eqs. 2.3c and 2.3b gives

$$\left(\nabla^2 + \epsilon\kappa_0^2\right) \mathbf{B} = 0. \tag{2.5b}$$

Thus, both the electric and magnetic fields satisfy the Helmholtz wave equation in three dimensions.

From here on, we choose the z axis as the propagation direction of the EM wave. The remainder of this chapter involves solving this equation in particular geometries relevant to the rest of this dissertation. Within the hole of an individual aperture or cavity within an aperture array we write solutions to Eqs. 2.5 in terms of a linear combinations of orthogonal waveguide mode solutions. Similarly, in the superstrate and substrate – the regions above and below the metamaterial – we write solutions in terms of linear combinations of orthogonal Floquet modes, i.e. plane waves satisfying periodic boundary conditions.

2.2 Waveguide modes

Within the apertures, solving the wave equations Eqs. 2.5 reduces to a standard waveguide problem. Here we follow Jackson's general solution approach.[24] If we separate the fields into components parallel and perpendicular to the z (propagation) axis,

$$\mathbf{H} = \mathbf{H}_t + \hat{z} H_z \tag{2.6a}$$

$$\mathbf{E} = \mathbf{E}_t + \hat{z} E_z, \tag{2.6b}$$

the transverse field components, $\mathbf{H}_t$ and $\mathbf{E}_t$, are related to the z components, H_z and E_z by

$$\mathbf{H}_t = \frac{1}{\epsilon \kappa_0^2 - k_z^2} \left[\pm i k_z \nabla_t H_z + i \epsilon \kappa_0 \hat{z} \times \nabla_t E_z \right] \tag{2.7a}$$

$$\mathbf{E}_t = \frac{1}{\epsilon \kappa_0^2 - k_z^2} \left[\pm i k_z \nabla_t E_z - i \kappa_0 \hat{z} \times \nabla_t H_z \right], \tag{2.7b}$$

where the choice of sign is positive for upward propagating waves, and negative for downward propagation, and ∇_t represents the transverse gradient (i.e. we leave off the z-derivative). With an assumed $\exp[\pm i k_z z]$ dependence to the EM fields, we have

$$F_z(\mathbf{r}) = \psi(\mathbf{r}_t) \exp[\pm i k_z z], \tag{2.8}$$

where F_z is the z-component of the electric (magnetic) field for TM (TE) modes, and $\mathbf{r}_t$ is a position vector in the transverse direction. The function $\psi(\mathbf{r}_t)$ is a solution to the two-dimensional, transverse wave equation

$$\left[\nabla_t^2 + \left(\epsilon \kappa_0^2 - k_z^2\right)\right] \psi = 0. \tag{2.9}$$

We refer to a particular solution ψ_{mn} to this equation, subject to appropriate boundary conditions, as a waveguide mode.

In cylindrical apertures or cavities, the solutions are

$$\psi_{mn}(r, \phi) = e^{im\phi} J_m\left(\beta_{mn} r\right), \tag{2.10a}$$

where J_m is the m-th Bessel function of the first kind, and the values of m and the radial wavevectors β_{mn} are determined from boundary conditions. Due to the cylindrical symmetry in our structures, m is an integer.

In rectangular apertures or cavities, the solutions are

$$\psi_{mn}(x,y) = \left\{A\sin\left[\beta_m^{(x)}x\right] + B\cos\left[\beta_m^{(x)}x\right]\right\}\left\{C\sin\left[\beta_n^{(y)}y\right] + D\cos\left[\beta_n^{(y)}y\right]\right\}, \tag{2.10b}$$

where the value of the transverse wavevectors, $\beta_m^{(x)}$ and $\beta_n^{(y)}$, and the constants A, B, C, and D are determined from boundary conditions.

These modes, either rectangular or cylindrical, form a complete, orthogonal set of functions, which allows any arbitrary field inside the cavity to be written as a linear combination of these cavity modes.

2.3 Floquet modes

Within the superstrate and substrate, we assume plane wave solutions to Eqs. 2.5, where

$$F(\mathbf{r}) = \exp\left[i\mathbf{k}^f \cdot \mathbf{r}\right], \tag{2.11}$$

represents the spatial dependence of both the electric and magnetic fields and $\mathbf{k}^f$ is the propagation wave vector. The electric and magnetic fields' magnitudes and components are related to each other through Eqs. 2.3.

For the periodic aperture arrays this thesis discusses, each individual unit cell is indistinguishable from any other unit cell. Therefore, if the fields are known in one unit cell, they must be identical in every other unit cell throughout the structure. Thus, the plane waves above the apertures must satisfy periodic boundary conditions

$$F(\mathbf{r}) = F(\mathbf{r} + \Lambda_1 \hat{\mathbf{x}}_1), \tag{2.12a}$$

and

$$F(\mathbf{r}) = F(\mathbf{r} + \Lambda_2 \hat{\mathbf{x}}_2), \tag{2.12b}$$

where $\Lambda_i \hat{\mathbf{x}}_i$, for $i = 1, 2$, are the two-dimensional primitive translation vectors of the array; i.e. the fields must be identical upon translating the measurement point to the next unit cell. It can be shown by substituting Eq. 2.11 into Eqs. 2.12 that restricting the transverse wavevectors to

$$k^f_{1m} = \hat{\mathbf{x}}_1 \cdot \mathbf{k}^f_0 + \frac{2m\pi}{\Lambda_1}, \tag{2.13a}$$

and

$$k^f_{2n} = \hat{\mathbf{x}}_2 \cdot \mathbf{k}^f_0 + \frac{2n\pi}{\Lambda_2}, \tag{2.13b}$$

is sufficient to satisfy the periodic boundary conditions when m and n are integers and $\mathbf{k}^f_0$ is the incident wave vector. Note, that conservation of energy, or substituting these results in Eq. 2.5 gives

$$k^f_{zmn} = \sqrt{\epsilon \kappa_0^2 - \left(k^f_{1m}\right)^2 - \left(k^f_{2n}\right)^2}, \tag{2.13c}$$

with

$$\mathbf{k}^f_{mn} = k^f_{1m}\hat{\mathbf{x}}_1 + k^f_{2n}\hat{\mathbf{x}}_2 + k^f_{zmn}\hat{\mathbf{z}}. \tag{2.14}$$

We refer to a particular plane wave solution

$$F_{mn}(\mathbf{r}) = \exp\left[i\mathbf{k}^f_{mn} \cdot \mathbf{r}\right]. \tag{2.15}$$

to Maxwell's equations subject to periodic boundary conditions as a Floquet mode. These Floquet modes are the coherently interfered propagating diffracted (for real k^f_z) and evanescent (for imaginary k^f_z) modes.

These modes form a complete, orthogonal set of functions, which allows any arbitrary field in the superstrate or substrate to be written as a linear combination of these cavity modes. The particulars of the relationships between various components of **E** and **H** will be discussed in Chapter 5.

Part I

Theoretical Approaches

Chapter 3

The skin depth boundary condition

3.1 Introduction

In this chapter we develop an approximate surface boundary condition for electromagnetic fields at metal walls, applicable at optical frequencies. This serves two purposes. First, this boundary condition is an integral part of a comprehensive theoretical explanation of enhanced optical transmission (EOT), discussed in Chapter 4. Secondly, a boundary condition is required for use in the numerical technique discussed in Chapter 5, and the insights of this chapter are applied in Chapter 6 to increase simulation efficiency. This boundary condition is applied at the metal walls inside a cavity or aperture in a metal film, and is used with the waveguide solutions of Eqs. 2.10 to find the unknown coefficients.

In a perfect electric conductor (PEC), charges are free to move, without any impedance or loss, and instantly respond to any applied field in a manner which ensures there is no electromagnetic field inside the conductor.[24] In real metals, however, electrons have a characteristic relaxation time, and do not respond instantly to incident fields.[25] Nevertheless, at very low frequencies, the electron relaxation time is much smaller than the time variation of the fields, and the response time is effectively instantaneous. Nevertheless, there remain bulk resistive properties of metal which manifest themselves as surface losses; these effects cause the dominant differences between metals at radio or microwave frequencies.

At higher frequencies, however, the optical properties of metals change drastically. The simplest empirical example of this is that gold, copper, and silver each *look* different from one another, see Fig. 1.1. This is due to the fact that the dielectric properties of metals vary drastically over the optical spectrum, see Fig. 3.1.[26] Fields do penetrate into metals at optical frequencies, decaying exponentially with a characteristic "skin depth", δ.[24]

The skin depth at various frequencies can be calculated using

$$\delta(\omega) = \frac{c}{\omega\kappa(\omega)}, \tag{3.1}$$

where

$$\kappa(\omega) = \sqrt{\frac{1}{2}\sqrt{\Im\left[\epsilon_m(\omega)\right]^{2} + \Re\left[\epsilon_m(\omega)\right]^{2}} - \frac{1}{2}\Re\left[\epsilon_m(\omega)\right]}, \qquad (3.2)$$

is the imaginary part of the index of refraction of the metal,[27] and where the value of the complex (dispersive) dielectric permittivity, $\epsilon_m = \epsilon'_m + i\epsilon''_m$, of the metal can be found experimentally or through an explicit theoretical expression, such as a Drude model,

$$\epsilon_m(\omega) = 1 - \frac{\omega_p^2}{\omega(\omega - i\omega_\tau)}, \qquad (3.3)$$

where ω_p is the plasma frequency and ω_τ is the collision frequency.[26]

One recent approach toward developing a boundary condition for the metal walls treats the cavity-metal structure at optical frequencies as a dielectric core-cladding fiber optic (FO) analogue and uses established techniques to numerically solve for the resulting modal dispersion curves.[28–30] The calculated modes are then analogous to propagating fiber optic modes, with TE, TM, or hybrid TE/TM-type waveguide modes.

The FO approach has the benefit of appealing to the vast body of work involving fiber optics, but it has a few notable limitations. First, if looking for real propagation modes, it numerically requires using a lossless Drude model for the metal dielectric, which does not adequately match the actual physical properties of most metals at optical frequencies. Introducing loss

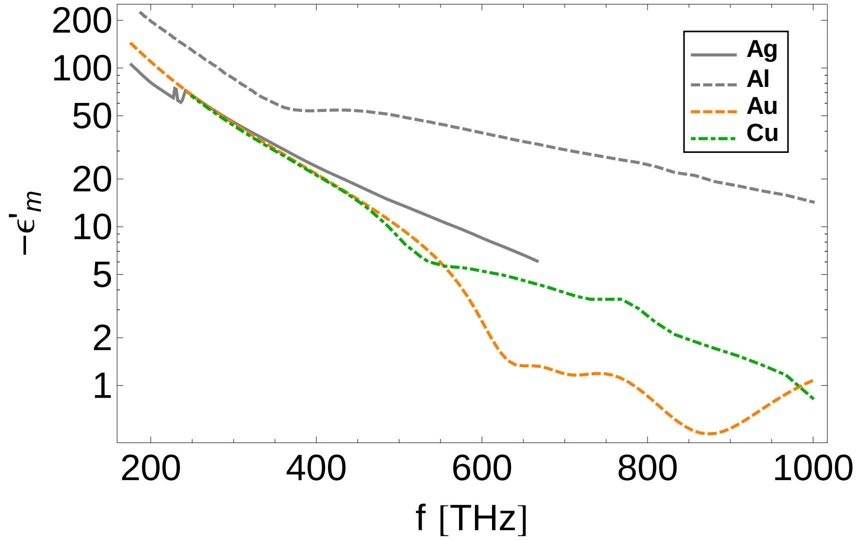

(a) Real component of metal dielectrics.

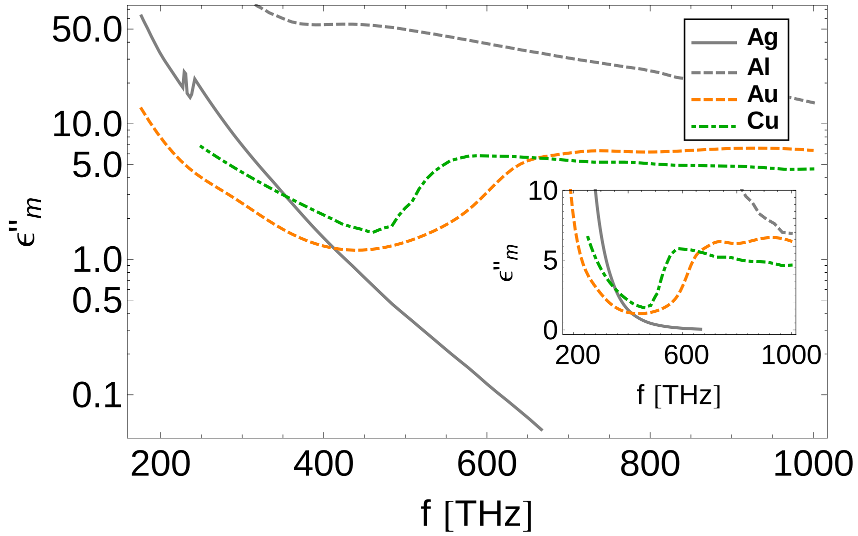

(b) Imaginary component of metal dielectrics.

Figure 3.1: The real (a) and imaginary (b) parts of metal dielectrics at optical frequencies.[26]

requires finding all complex roots to the equation, which in general is not a trivial task. Furthermore, while this approach can be used for cylindrical apertures, it is difficult to generalize for other geometries.[31, 32] Finally, the dispersion curves must always be calculated numerically using this method, and any effects due to changing geometries must be extracted empirically.

Nevertheless, modal dispersion analysis is a useful approach for determining some properties of the waveguide modes that can be excited within a particular aperture. In this chapter we present a surface approximation used for calculating the modal dispersion relationship of cylindrical and rectangular apertures in real metals. The goal is to find an equivalent waveguide geometry which accurately captures the properties of the aperture as well as the effect of the real metal walls. It has already been shown with stacked photonic crystal nanocavities that resonance properties of a complicated structure can be accurately described by determining an effective resonant cavity with PEC walls.[33] Here, too, we find an effective PEC cavity using the metallic skin depth as the limiting length scale at the cavity walls, hence "skin depth boundary condition" (SDBC).

This analysis carries all the benefits of dispersion analysis as discussed in reference [30] for example, with the added benefit of determining the evanescent modes and including real metal parameters. This approach describes the fundamental behavior of waveguide modes at optical frequencies using approximate boundary conditions. Unlike many other approaches, this theoretical model directly predicts the dispersion curve, and its dependence on aperture dimensions and metal parameters, without needing to rely on interpretation of numerical solutions.

3.2 Boundary conditions

Although the metallic skin depths at optical frequencies can be large, beyond that depth we expect metals to behave like perfect conductors, i.e. the fields drop rapidly to zero. When the skin depth, δ, is significantly smaller than the characteristic aperture dimension, a, this allows significant simplification of the resulting equations. To compare these sizes, we note that a is typically on the order of the wavelength, λ. Fig. 3.2 shows the variation of the ratio δ/λ for a few metals over a range of frequencies. Note that this ratio is small enough that we can consider the contribution of the fields in the metal as a correction to the dominant waveguide fields, yet not so small that this effect would be negligible.

To determine the dimensions of the effective cavity cross-section, we note that the fields inside the metal walls of a cylindrical cavity can be written in terms of Hankel functions of the first kind,[28] and as sine or cosine func-

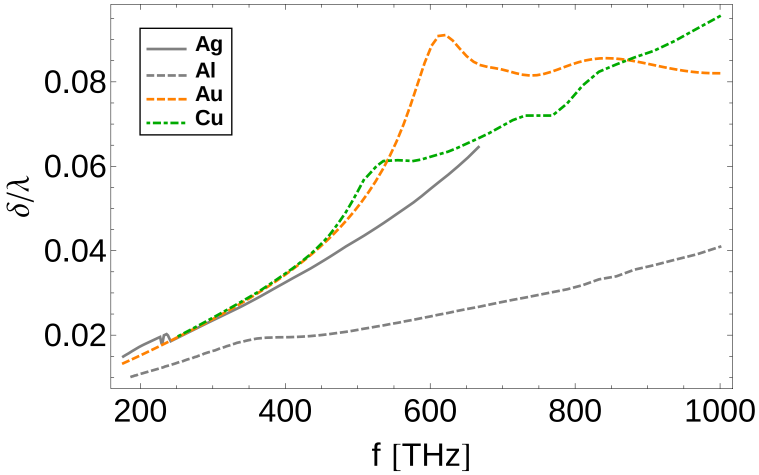

Figure 3.2: The ratio of δ/λ for a few metals over a range of frequencies.

tions weighted by a decaying exponential in a rectangular cavity.[24] In both of these cases, the fields decay extremely rapidly upon entering the metal. Thus, the majority of the fields in the metal are constrained within a very small region close to the surface of the aperture. We make the reasonable assumption that upon reaching one skin depth into the metal we have accounted for the contribution of the fields within the metal, and beyond that point it is effectively a PEC.

Then, for an arbitrary aperture, we can apply the perfect electric conductor boundary conditions:

$$\hat{\mathbf{n}} \times \mathbf{E} = 0, \tag{3.4a}$$

$$\hat{\mathbf{n}} \cdot \mathbf{H} = 0, \tag{3.4b}$$

where $\hat{\mathbf{n}}$ is a unit normal to the cavity wall, at a depth of δ into the metal, rather than at the cavity walls themselves, see Fig. 3.3(a). We will derive results in this chapter for cylindrical and rectangular apertures.

It is important to highlight that this analysis does not describe the complete details of the fields' behavior within the metal. This is different than other approaches discussed in the introduction that do, in fact, describe the fields in the metal explicitly. Instead we consider only the overall effect that the imperfect conductor has on the behavior of the fields within the cavity itself. This simplification allows us to avoid relying on numerical techniques while still determining the consequences of these effects.

3.3 Dispersion analysis

Using conservation of energy, or by substituting Eqs. 2.10 into Eq. 2.9, we get the dispersion relations,

$$\epsilon\frac{\omega^2}{c^2} = k_z^2 + \beta^2, \tag{3.5a}$$

for cylindrical apertures, and

$$\epsilon\frac{\omega^2}{c^2} = k_z^2 + \left[\beta_m^{(x)}\right]^2 + \left[\beta_n^{(y)}\right]^2 \tag{3.5b}$$

for rectangular apertures. For what follows we will consider apertures filled with a dielectric material of permittivity ϵ, embedded in a metal film with

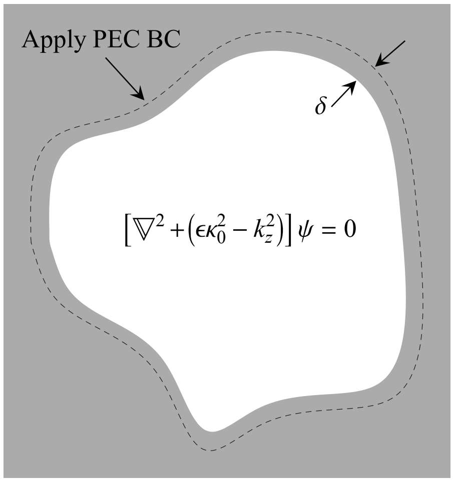

(a) General waveguide geometry.

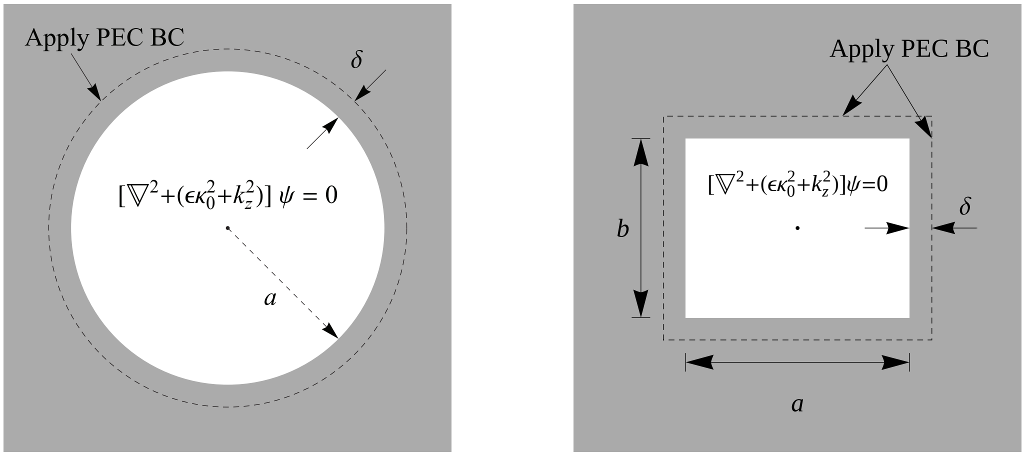

(b) Cylindrical waveguide geometry. (c) Rectangular waveguide geometry.

Figure 3.3: Schematic of general (a), cylindrical (b), and rectangular (c) waveguide geometries and solution strategy. The gray region represents the metal, the white region is the dielectric-filled aperture, and the dashed curve represents a skin depth inside the metal.

complex dielectric permittivity ϵ_m.

Equations 3.5 have the benefit of solving for all possible modes, both propagating (real k_z) and evanescent (imaginary k_z). It is well known that near-field evanescent fields can contribute significantly to the ability of structures to couple to incident light as well as transmitted waves.[34,35] Furthermore, as discussed earlier, the decay length can be many multiples of film thickness in thin films, whereby evanescent modes within an aperture may directly contribute to EOT. Hence, solving for all modes, both propagating and evanescent, produces a more complete picture of the resonance behavior of these apertures. We now use the SDBC to evaluate these dispersion relations.

3.3.1 Cylindrical apertures

Here we discuss a cylindrical aperture of radius a, see Fig. 3.3(b). Waveguide modes are given in Eq. 2.10a. We find β by evaluating $J_m\left[\beta(a+\delta)\right]=0$ for TM modes and $J'_m\left[\beta(a+\delta)\right]=0$ for TE modes. Applying these conditions gives

$$\beta = \left(\frac{1}{1+\xi}\right)\beta_0 \tag{3.6}$$

where

$$\beta_0^{\mathrm{TM}} \equiv \frac{\chi_{mn}}{a} \tag{3.7a}$$

$$\beta_0^{\mathrm{TE}} \equiv \frac{\chi'_{mn}}{a} \tag{3.7b}$$

with χ_{mn} being the nth root of the mth Bessel function, χ'_{mn} being the nth root of the derivative of the mth Bessel function, and

$$\xi \equiv \delta/a. \tag{3.8}$$

This is a general analytical result for any radius and any metal; for a particular radius and metal combination one need only numerically calculate the ratio ξ to determine the particular shift in modal dispersion.

Note, that for a perfect conductor $\delta \to 0$ so $\xi \to 0$, and we recover the well-known PEC waveguide modes β_0.[24] As the relative length of the skin depth increases (i.e. the metal becomes increasingly less PEC-like), ξ increases, and the magnitude of the transverse wavevector decreases. This, in turn, shifts the dispersion curve toward lower frequencies (see Fig. 3.4(a), inset).

3.3.2 Rectangular apertures

Here we discuss a rectangular aperture with sides of length a and b, see Fig. 3.3(c). Waveguide modes are given in Eq. 2.10b, shifting the origin to the center of the aperture. That is,

$$\psi = \psi_{mn}(x + a/2 + \delta, y + b/2 + \delta). \tag{3.9}$$

We find $\beta^{(x)}$ and $\beta^{(y)}$ by evaluating $\psi(-a/2 - \delta, y) = 0$, $\psi(a/2 + \delta, y) = 0$, $\psi(x, -b/2 - \delta) = 0$, and $\psi(x, b/2 + \delta) = 0$ for TM modes, and $\frac{\partial}{\partial(-x)}\psi(-a/2 - \delta, y) = 0$, $\frac{\partial}{\partial x}\psi(a/2 + \delta, y) = 0$, $\frac{\partial}{\partial(-y)}\psi(x, -b/2 - \delta) = 0$, and $\frac{\partial}{\partial y}\psi(x, b/2 + \delta) = 0$ for TE modes. Applying these conditions gives $B = D = 0$ for TM modes and $A = C = 0$ for TE modes, and

$$\beta = \left(\frac{1}{1 + 2\xi}\right)\beta_0, \tag{3.10}$$

for both the x or y wave vectors, where

$$\beta_0^{(x)} \equiv \frac{m\pi}{a} \tag{3.11a}$$

$$\beta_0^{(y)} \equiv \frac{n\pi}{b} \tag{3.11b}$$

with

$$\xi^{(x)} \equiv \delta/a \tag{3.12}$$

$$\xi^{(y)} \equiv \delta/b. \tag{3.13}$$

This is a general analytical result for any lengths and any metal; for a particular size and metal combination one need only numerically calculate the ratios ξ to determine the particular shift in modal dispersion. The extra factor of ξ in Eq. 3.10 as compared to the cylindrical result (Eq. 3.6) highlights the fact the fields penetrate an extra distance at two surfaces, rather than at the single surface of a cylinder.

Note, that for a perfect conductor $\delta \rightarrow 0$ so $\xi \rightarrow 0$, and we recover the well-known PEC waveguide modes β_0.[24] As the relative length of the skin depth increases (i.e. the metal becomes increasingly less PEC-like), ξ increases, and the magnitude of the transverse wavevector decreases. This, in turn, shifts the dispersion curve toward lower frequencies (see Fig. 3.4(b), inset).

3.3.3 Sample comparison with simulation

Figure 3.4 shows a number of dispersion curves for apertures filled with a dielectric $\epsilon = 3$, in silver, using a Drude model (Eq. 3.3) for the metal dielectric with $\omega_p = 1.37 \times 10^{16}\,\mathrm{s}^{-1}$ and $\omega_\tau = 7.29 \times 10^{13}\,\mathrm{s}^{-1}$. The cylindrical hole (Fig. 3.4(a)) has a radius $a = 190$ nm, and the square hole (Fig. 3.4(a)) has a side length $a = b = 190$ nm. The solid curves are calculated using this method, along with finite element full-wave eigenmode simulations of the same structure. As the figure shows, there is strong agreement between the theoretical prediction (solid curves) and the simulation results (points). The inset shows the curves predicted by this model (solid) as well as the curves using a PEC boundary condition (dotted). The shift to lower frequencies seen here is due to the effectively larger cavity.

There is one dispersion curve not accounted for by this model in the rectangular geometry (green in Fig. 3.4(b)). It seems that the degenerate TE/TM 11 mode is slightly perturbed under the TM polarization in a manner that is not accounted for by this model. Further analysis is required to fully determine the cause of this mode.

3.4 Cutoff dependence

Using the cutoff condition, $k_z = 0$, we can solve Eqs. 3.5 for the cutoff frequency, ω_{cutoff}, of a mode in terms of the dimensions of an aperture which supports it.

Practically, due to the frequency dependance of δ, for cylindrical apertures, it's easier to directly calculate the radius

$$a = \frac{c}{\omega_{\text{cutoff}}^{\text{TM}}} \frac{\chi_{mn}}{\sqrt{\epsilon}} - \delta\left(\omega_{\text{cutoff}}^{\text{TM}}\right) \tag{3.14a}$$

$$a = \frac{c}{\omega_{\text{cutoff}}^{\text{TE}}} \frac{\chi'_{mn}}{\sqrt{\epsilon}} - \delta\left(\omega_{\text{cutoff}}^{\text{TE}}\right) \tag{3.14b}$$

in terms of ω_{cutoff}. Note how apertures with smaller radii (by a subtractive factor of δ) permit higher frequency resonances as compared to the perfect

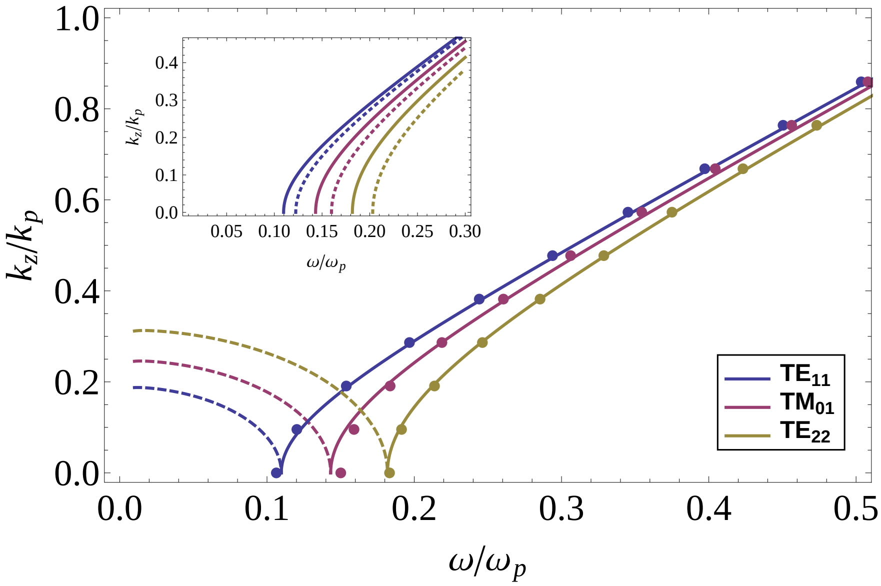

(a) Results for cylindrical apertures of radius $a = 190$ nm.

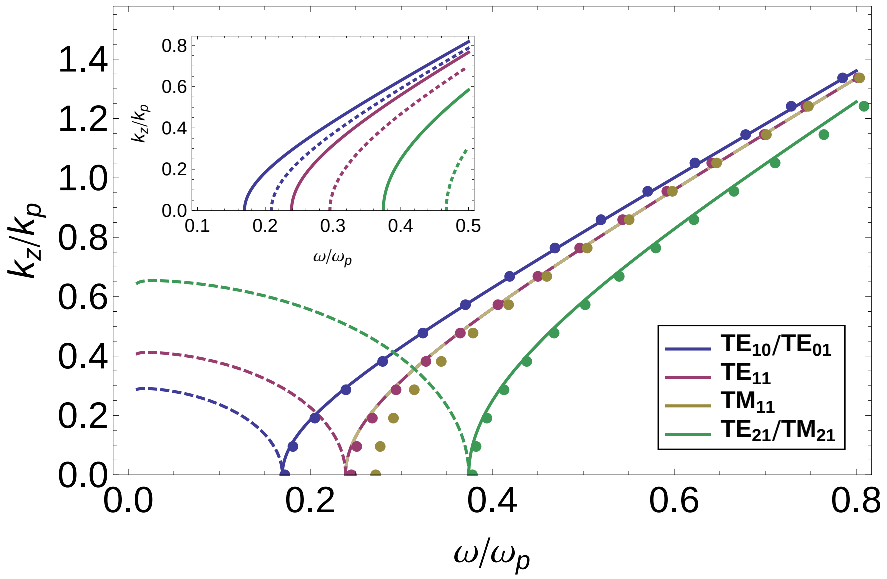

(b) Results for square apertures with side length $a = 190$ nm.

Figure 3.4: The real (solid) and imaginary (dashed) dispersion curves calculated and simulated (points) for cylindrical (a) [square (b)] apertures of radius [side length] $a = 190$ nm filled with a dielectric $\epsilon = 3$ embedded in Drude silver. Here $k_p \equiv \omega_p/c$. Inset shows results using this method (solid) compared to PEC modal dispersion (dashed).

electric conductor condition. Here, too, when $\delta \to 0$ as in a PEC we recover the well-known cutoff result. Fig. 3.5(a) shows a plot of f_{cutoff} for a few modes with cylindrical apertures, filled with a dielectric $\epsilon = 3$ embedded in Drude silver, as a function of the radius a. Note that for a given radius the cutoff frequency is lower using this model (solid) compared to the PEC values (dashed), again due to the effectively larger cavity size.

Similarly, for rectangular apertures, we calculate the cutoff frequency:

$$\omega_{\text{cutoff}} = \frac{c}{\sqrt{\epsilon}} \sqrt{\left(\beta_m^{(x)}\right)^2 + \left(\beta_n^{(y)}\right)^2}. \tag{3.15}$$

Note that the values of β, which depend explicitly on a and b, also implicitly depend on ω, and the roots can be found using various methods. Fig. 3.5(b) shows a plot of f_{cutoff} for a few modes with square apertures, filled with a dielectric $\epsilon = 3$ embedded in Drude silver, as a function of the side length a. Note that for a given length the cutoff frequency is lower using this model due to the effectively larger cavity size. Additionally, as the cavity size increases, the cutoff approaches the PEC value, as the contributions of the metal become increasingly negligible.

In both of these cases, however, if $\delta(\omega)$ does not vary greatly over the range of frequencies, this can be viewed as an approximation for the cutoff frequency, without further calculations. It is worthwhile to note that the

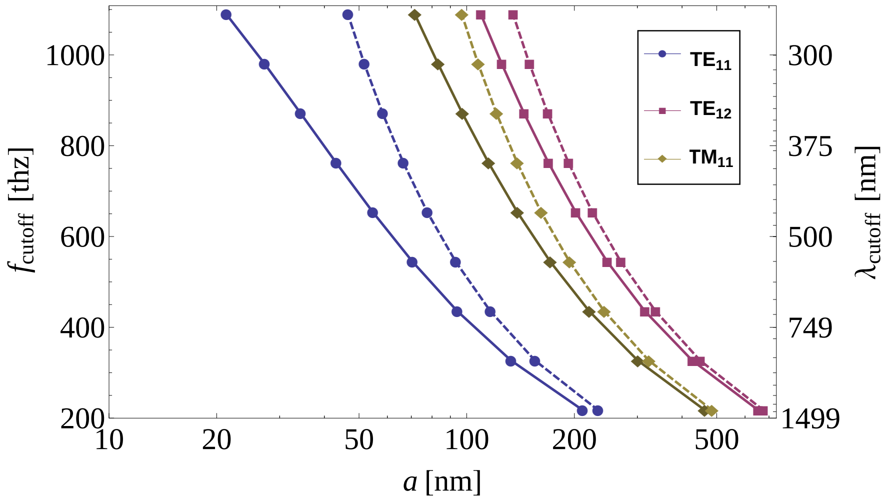

(a) Results for cylindrical apertures.

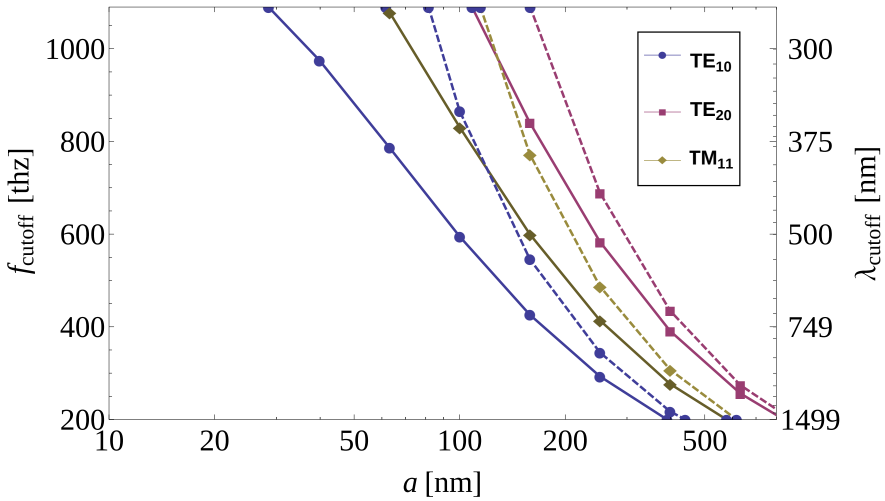

(b) Results for square apertures.

Figure 3.5: The cutoff frequency f_{cutoff} in cylinders (a) [squares (b)] filled with a dielectric $\epsilon = 3$ as a function of the radius [length] a for a few modes in silver. The solid lines are calculated using the method described in this chapter, the dashed lines are curves using for a perfect conductor.

general trend of these results (i.e. cutoff shifted toward lower frequencies) has been known empirically for some time, from experimental and numerical methods.[36] Here, though, we predict these properties in an intuitive analytical form, based on a new approximation for the interaction of the waveguide fields with realistic metals. Therefore, we view those established results as a confirmation of the theoretical approach developed here.

3.5 Effect on fields and induced charges and currents

Using Eqs. 2.10 with Eqs. 3.6 or 3.10 allows us to calculate the field profiles within the apertures. Fig. 3.6 shows some calculated cylindrical ψ fields for a few TM (a) and TE (b) modes for $\xi = 0.15$, and Fig. 3.7 shows some calculated rectangular ψ fields for a few TM (a) and TE (b) modes for $\xi^{(x)} = 0.15$ and $\xi^{(y)} = 0.21$. Note that these fields are only plotted within the cavity, and not into the cavity walls, as we have not analyzed the detailed behavior of the fields within the metal, only the net effect it has on the cavity response. Additionally, note that the fields do not drop to zero at the cavity walls as they do for a perfect conductor.

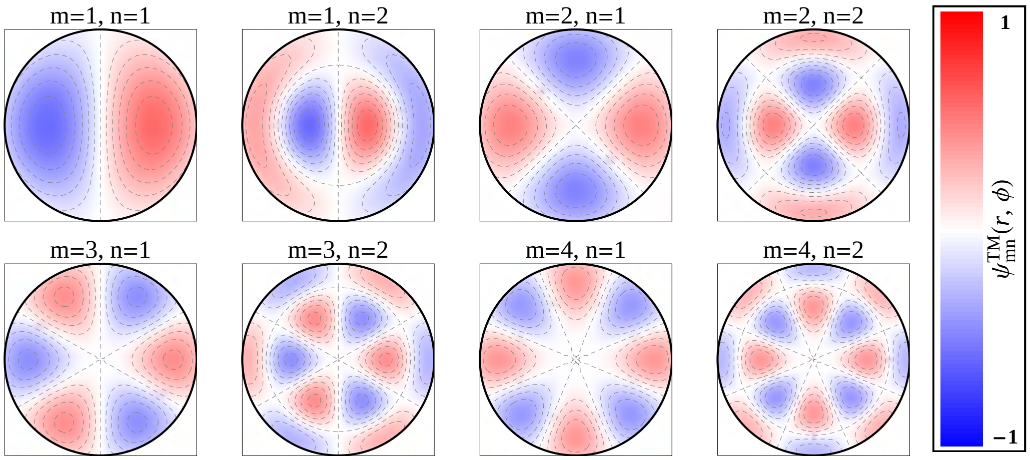

(a) TM mode fields.

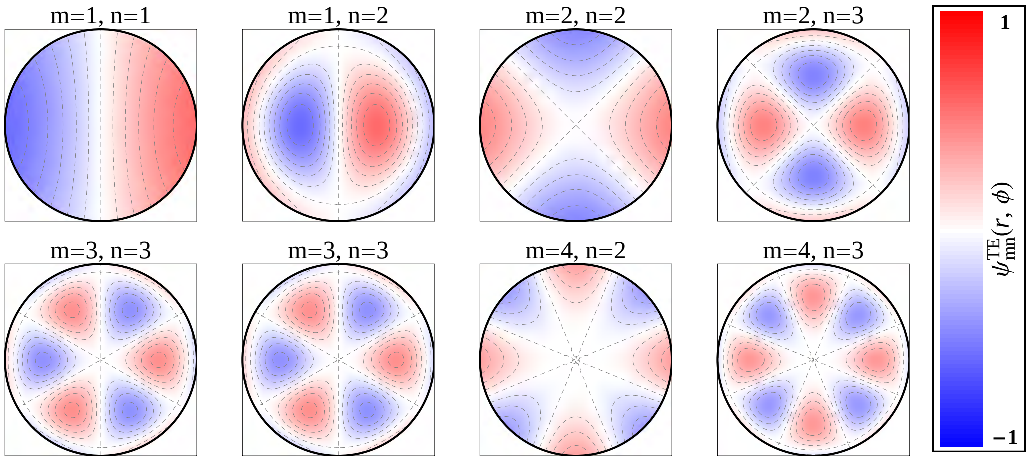

(b) TE mode fields.

Figure 3.6: Calculated TM (a) and TE (b) ψ fields in the cylindrical geometry, with $\xi = 0.15$.

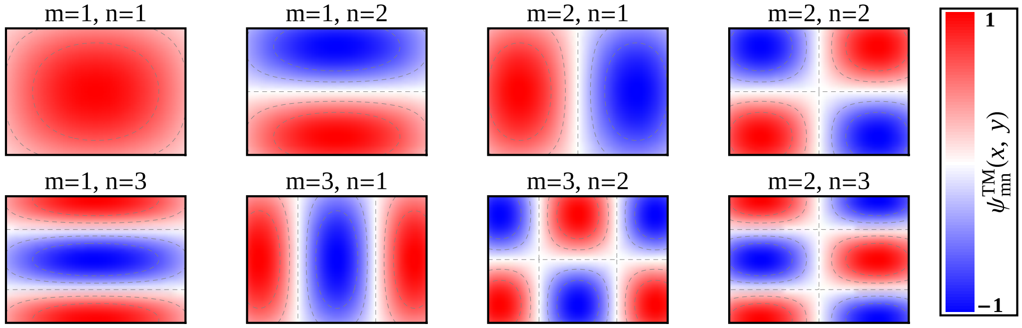

(a) TM mode fields.

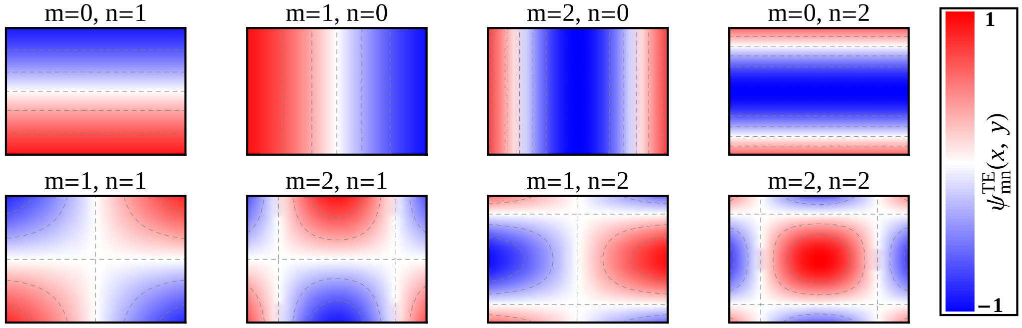

(b) TE mode fields.

Figure 3.7: Calculated TM (a) and TE (b) ψ fields in the rectangular geometry, with $\xi^{(x)} = 0.15$ and $\xi^{(y)} = 0.21$.

3.5.1 Cylindrical apertures

For $\xi \ll 1$, we can expand Eq. 2.10a in powers of ξ. Keeping through quadratic terms, we have

$$\begin{aligned}\psi(r,\phi) = \{J_m\left(\beta_0 r\right) &- \frac{1}{2}\xi(\xi-2)\beta_0 r J_{m+1}\left(\beta_0 r\right) \\ &+ \frac{1}{2}\xi\left[m(m\xi+\xi-2)-\xi\beta_0^2 r^2\right] J_m\left(\beta_0 r\right)\} e^{im\phi}. \qquad (3.16)\end{aligned}$$

This corresponds to the perfect electric conductor field $J_m\left(\beta_0 r\right)$ plus a correction due to the additional buildup of charges in the metal.

Fig. 3.8 shows a plot of ψ^{TM} for $m=1$, $n=2$ and $\xi=0.12$. If the dielectric of the metal is calculated using Eq. 3.3 with $a=190$ nm, this value of ξ corresponds to $f=611\,\mathrm{THz}$. The thin line is the PEC field component of Eq. 3.16, with the dashed line being the correction due to our method. The thick black line corresponds to the complete field behavior (i.e. the PEC contribution plus the correction). We have additionally plotted the decay of the fields into the metal walls. Note that the dominant contribution to total field strength is from the portion of the field concentrated within the cavity, with only small portions of the field penetrating into the metal.

Equation 3.16 shows that for good conductors (i.e. small ξ) there is no shift in the resonance of the cavity for the lowest order modes, while there is a change in the overall field behavior accounting for the buildup of additional

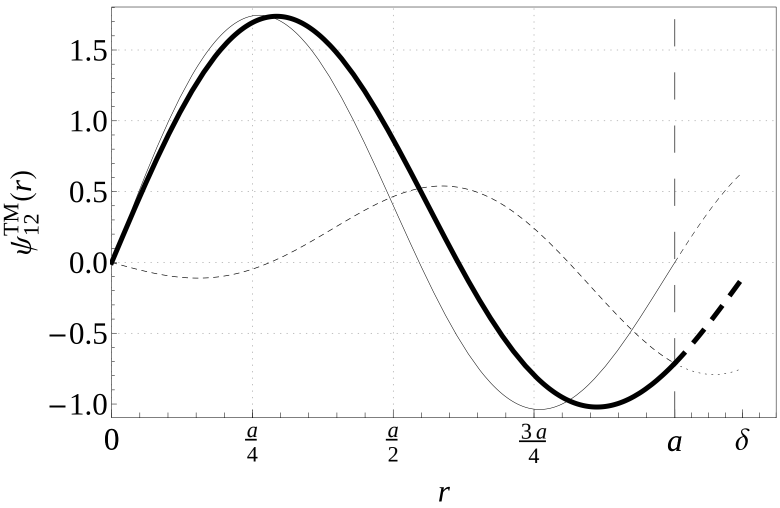

Figure 3.8: The radial field dependance of ψ^{TM} for a TM mode using Eq. 3.16 for $m = 1$, $n = 2$, and $\xi = 0.12$. The thin line is the perfect conductor waveguide mode, the dashed line is the contribution due to additional charges in the metal, and the thick line is the superposition of the two. The vertical dashed lines indicate the positions of the cavity walls. The rapid decay of the field inside the cavity walls is also plotted.

surface charges. For larger ξ or higher order modes, however, it is necessary to use the complete expressions Eqs. 2.10a and 3.6 to calculate the dispersion relation. Additionally, although ξ varies as a function of frequency, if there is minimal variation of this value over the frequency region of interest, it is straightforward to calculate the shift in resonance using Eq. 3.6.

Furthermore, note that at the metal surface, $r = a$, there is a nonzero E_z (H_z) for TM (TE) field equal to

$$\left.\begin{matrix} E_z \\ H_z \end{matrix}\right\} = -\frac{1}{2}\xi(\xi - 2)\chi_{mn}J_{m+1}[\chi_{mn}]e^{im\phi}. \tag{3.17}$$

This correction can be thought of as the contribution to the field from an effective distribution of surface charges, σ_{SDBC}, on the surface of the metal originating from the buildup of charge in the region of field penetration into the metal walls. This is in addition to the surface charges, σ_{PEC}, which arrange themselves on a perfect conductor to counterbalance the incident field. Then, the total surface charge on the metal is

$$\sigma = \sigma_{\mathrm{PEC}} + \sigma_{\mathrm{SDBC}}. \tag{3.18}$$

We find the value of σ using the continuity expressions

$$\hat{n} \cdot (\mathbf{D}_2 - \mathbf{D}_1) = 4\pi\sigma \tag{3.19}$$

resulting from Gauss's law,[24] where $\hat{n}$ is a unit normal from region 1 to region 2. Requiring the field inside the metal ($\mathbf{D}_2$) to drop to zero, we get

$$\sigma_{\mathrm{PEC}} = \frac{i\epsilon k_z}{4\pi}\frac{\beta_0}{\beta^2} J_{m+1}[\chi_{mn}] e^{im\phi}, \tag{3.20a}$$

$$\sigma_{\mathrm{SDBC}} = -\frac{1}{2}\xi^2 \left(\chi_{mn}^2 - m^2\right) \sigma_{\mathrm{PEC}}. \tag{3.20b}$$

where the value of k_z is determined by Eq. 3.5a and β by Eq. 3.6. These expressions result from first operating on Eq. 2.10a, and then expanding in powers of ξ. Note that $\chi_{mn}^2 > m^2$, so this additional effective surface charge distribution is always of opposite sign to the perfect conductor distribution.

We can likewise break the induced effective surface current,

$$\mathbf{J} = \mathbf{J}_{\mathrm{PEC}} + \mathbf{J}_{\mathrm{SDBC}}, \tag{3.21}$$

into the current, $\mathbf{J}_{\mathrm{PEC}}$, present in a perfect conductor and the surface plasmon current $\mathbf{J}_{\mathrm{SDBC}}$. Using the continuity expressions,

$$\hat{n} \times (\mathbf{B}_2 - \mathbf{B}_1) = \frac{4\pi}{c}\mathbf{J}, \tag{3.22}$$

requiring the field inside the metal ($\mathbf{B}_2$) to drop to zero, we get currents

$$\mathbf{J}_{\mathrm{PEC}} = \hat{z}\,\frac{ic\epsilon\kappa_0}{4\pi}\frac{\beta_0}{\beta^2} J_{m+1}[\chi_{mn}] e^{im\phi}, \tag{3.23a}$$

$$\mathbf{J}_{\mathrm{SDBC}} = -\frac{1}{2}\xi^2 \left(\chi_{mn}^2 - m^2\right) \mathbf{J}_{\mathrm{PEC}}, \tag{3.23b}$$

traveling upwards and downwards. Here the additional induced current travels in the opposite direction to the current induced in a perfect conductor.

This decrease in current is due to the resistive losses occurring in the region of field penetration into the metal.

3.5.2 Rectangular apertures

For $\xi \ll 1$, we can expand Eq. 2.10b in powers of ξ. Keeping through linear terms, we have

$$\begin{aligned}\psi^{\mathrm{TM}}(x,y) = \sin[\beta_0^{(x)}x']\sin[\beta_0^{(y)}y] \\ - \xi^{(x)}\frac{2\pi m x}{a}\cos[\beta_0^{(x)}x']\sin[\beta_0^{(y)}y'] \\ - \xi^{(y)}\frac{2\pi n y}{b}\sin[\beta_0^{(x)}x']\cos[\beta_0^{(y)}y'],\end{aligned} \tag{3.24a}$$

and

$$\begin{aligned}\psi^{\mathrm{TE}}(x,y) = \cos[\beta_0^{(x)}x']\cos[\beta_0^{(y)}y'] \\ + \xi^{(x)}\frac{2\pi m x}{a}\sin[\beta_0^{(x)}x']\cos[\beta_0^{(y)}y'] \\ + \xi^{(y)}\frac{2\pi n y}{b}\cos[\beta_0^{(x)}x']\sin[\beta_0^{(y)}y'],\end{aligned} \tag{3.24b}$$

where $x' \equiv x + a/2$ and $y' \equiv y + b/2$. This corresponds to the perfect electric conductor fields $\sin[\beta_0^{(x)}x']\sin[\beta_0^{(y)}y']$ or $\cos[\beta_0^{(x)}x']\cos[\beta_0^{(y)}y']$ plus a correction due to the additional buildup of charges in the metal.

Fig. 3.9 shows a plot of ψ^{TE} as a function of x when $y = 0$ for $m = 1$, $n = 0$ and $\xi^{(x)} = 0.12$. If the dielectric of the metal is calculated using

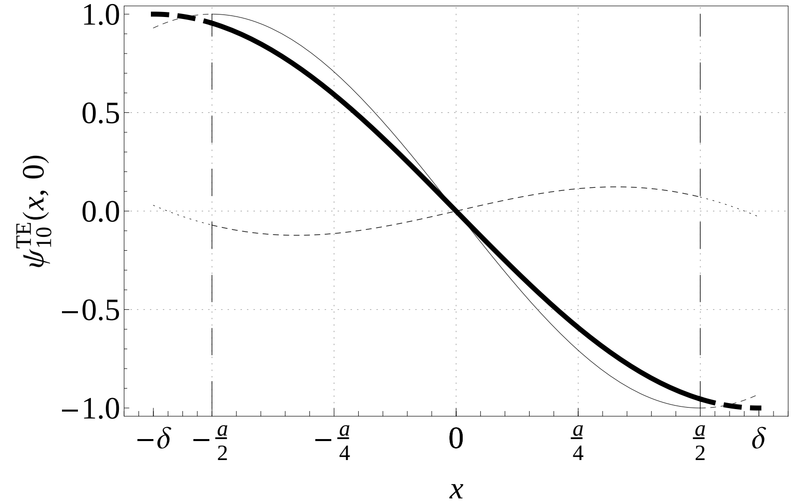

Figure 3.9: The x field dependance of ψ^{TE} along $y = 0$ for a TE mode using Eq. 3.24 for $m = 1$, $n = 0$, and $\xi^{(x)} = 0.12$. The thin line is the perfect conductor waveguide mode, the dashed line is the contribution due to additional charges in the metal, and the thick line is the superposition of the two. The vertical dashed line indicates the position of the cavity walls. The rapid decay of the field inside the cavity walls is also plotted.

Eq. 3.3 with $a = 190$ nm, this value of $\xi^{(x)}$ corresponds to $f = 611\,\mathrm{THz}$. The thin line is the PEC field component of Eq. 3.24, with the dashed line being the correction due to our method. The thick black line corresponds to the complete field behavior (i.e. the PEC contribution plus the correction). We have additionally plotted the decay of the fields into the metal wall. Note that the dominant contribution to total field strength is from the portion of the field concentrated within the cavity, with only small portions of the field penetrating into the metal.

Equation 3.24 shows that for good conductors (i.e. small ξ) there is no shift in the resonance of the cavity for the lowest order modes, while there is a change in the overall field behavior accounting for the buildup of additional surface charges. For larger ξ or higher order modes, however, it is necessary to use the complete expressions Eqs. 2.10b and 3.10 to calculate the dispersion relation. Additionally, although ξ varies as a function of frequency, if there is minimal variation of this value over the frequency region of interest, it is straightforward to calculate the shift in resonance using Eq. 3.10.

Furthermore, note that at the metal surface, there is a nonzero E_z (H_z) for TM (TE) field. For example, at the $x = a/2$ surface, this field is equal to

$$E_z = -\xi^{(x)} \frac{2\pi m x}{a} (-1)^m \sin[\beta_0^{(y)} y'] \tag{3.25a}$$

$$H_z = \xi^{(y)} \frac{2\pi n y}{b} (-1)^m \sin[\beta_0^{(y)} y']. \tag{3.25b}$$

This correction can also be thought of as the contribution to the field from an effective distribution of surface charges, σ_{SDBC}, on the surface of the metal originating from the buildup of charge in the region of field penetration into the metal walls. This is in addition to the surface charges, σ_{PEC}, which arrange themselves on a perfect conductor to counterbalance the incident field. We can find the value of the total surface charge, σ, on each wall using Eq. 3.19. We can likewise calculate the induced effective surface current $\mathbf{J}$ using Eq. 3.22. We do not carry out these calculations here, as the resulting expressions are quite messy (there are four of each quantities for each of the four walls) and do not yield any further fundamental insight beyond that of the cylindrical geometry.

3.6 Attenuation

We can also use these results to calculate the attenuation constant, α, i.e. the time-averaged fractional power lost per unit length of the cavity. The time-average power absorbed per unit length along the aperture is

$$P_{\text{abs}} = \frac{\omega\delta}{16\pi} \oint \left|H_{\parallel}\right|^2 \, ds, \tag{3.26}$$

where the integral is taken around the boundary of the aperture.[24] The time-averaged power transmitted per unit length, P_{trans}, is found by taking the $\hat{z}$ component of the time-averaged Poynting vector,

$$\mathbf{S} = \frac{1}{2}\frac{c}{8\pi}\text{Re}\left[\mathbf{E} \times \mathbf{H}^*\right], \tag{3.27}$$

integrated over the area of the aperture. The ratio

$$\alpha \equiv \frac{P_{\text{abs}}}{P_{\text{trans}}} \tag{3.28}$$

is the power lost per unit length in propagating modes, normalized with respect to the amount of power flowing down the cavity. Then, the power, P, decays along the aperture as a function of z by

$$P(z) = P_0 e^{-\alpha z}, \tag{3.29}$$

where P_0 is the incident power.

For cylindrical apertures, $\left|H_{\parallel}\right|^2 = |H_\phi|^2 + |H_z|^2$, whence

$$\alpha^{\mathrm{TM}} = \xi\epsilon\kappa_0^2 \left(a\beta B_{m-1} - mB_m\right)^2 \Big[k_z\big(a^2\beta^2 B_{m-1}^2 + B_m^2 \left(a^2\beta^2 - 2(-1)^m m\right) + 2a\beta\left((-1)^m - m\right) B_m B_{m-1}\big)\Big]^{-1}, \quad (3.30)$$

and

$$\alpha^{\mathrm{TE}} = \xi B_m^2 \left(a^2\beta^4 + m^2 k_z^2\right) \Big[k_z\big(2a\left((-1)^m + m\right)\beta B_{-1+m} B_m + \left(-2m\left((-1)^m + 2m\right) + a^2\beta^2\right) B_m^2 + a^2\beta^2 B_{1+m}^2\big)\Big]^{-1}, \quad (3.31)$$

where $B_m \equiv J_m(\beta a)$. These expressions can also be expanded in powers of ξ to yield an approximate expression for α. Furthermore, α is proportional to ξ, so for a PEC α is zero, and the structure is lossless. For rectangular aperture we must integrate the components of $\mathbf{H}$ parallel to the wall over all four edges of the aperture. The resulting expressions are quite messy, and do not yield any additional insight. Nevertheless, Fig. 3.10 shows the variation of α as a function of frequency for cylindrical, as well as square apertures. Note that for square apertures the degenerate TM_{11} and TE_{11} modes have different attenuation characteristics; this may be another manifestation of the effect that causes the mode splitting discussed earlier.

After the initial drop in loss above the cutoff, α increases with frequency due to larger portions of the field penetrating into the metal, as seen in

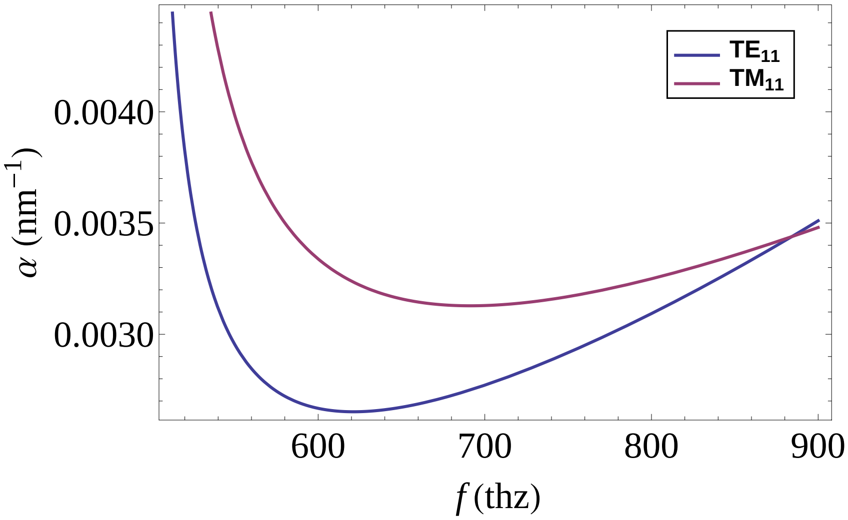

(a) Results for cylindrical apertures of radius $a = 190$ nm.

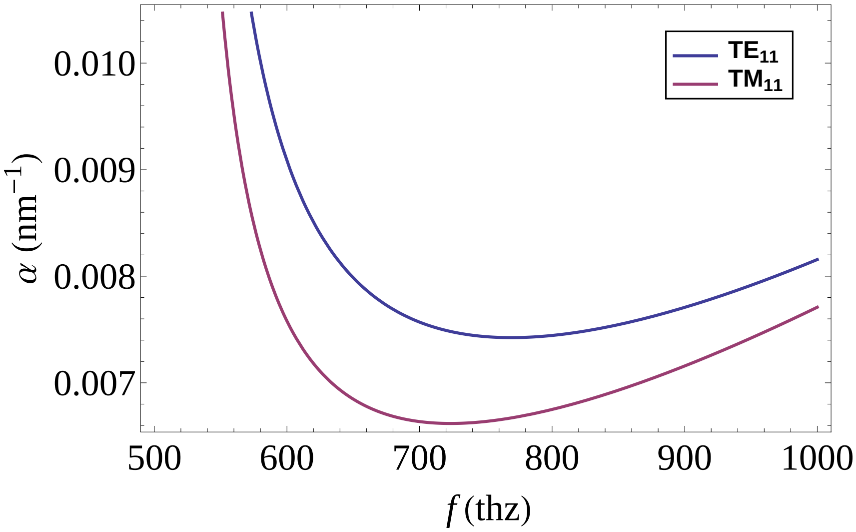

(b) Results for square apertures with side length $a = 190$ nm.

Figure 3.10: The fractional power loss α per unit length of a cylindrical (a) [square (b)] aperture of radius [side length] $a = 190\,\text{nm}$ filled with a dielectric $\epsilon = 3$ embedded in Drude silver. The loss is plotted for the TE_{11} and TM_{11} modes.

Fig. 3.10. Note that this expression only holds above the cutoff frequency. Furthermore, for an aperture of a particular size there is a frequency at which the loss is minimized. This frequency can, in principle be found by finding the root of

$$\frac{\partial \alpha}{\partial a} = 0 \tag{3.32}$$

in terms of ω. These solutions will depend on the explicit form of $\xi(\omega)$ for a given metal, as well as the particular radius of interest.

It is worthwhile to note that there is no minimum to α with respect to the aperture radius. For larger cavity size, α tends towards zero, as the propagating energy is proportional to a^2, while, for a particular frequency, the skin depth is fixed. Thus, the *relative* amount of loss decreases with increasing size.

3.7 Summary and conclusions

We have presented a new model for the interaction of electromagnetic fields in small holes in real metals at optical frequencies. Unlike other approaches, this simple model allows direct analytic predictions of various resonance properties, without needing to rely on numerical coupled-wave or finite element analyses or other numerical techniques. We have shown, through illustrative examples with silver, strong agreement between the theory and simulated results for both cylindrical and square apertures, and some predictions of this model are confirmed by long-known empirical results, as well.

Although the model was applied to apertures in silver, another major advantage of this approach is that the analytical form of the field response of all metals and cylindrical apertures is the same. The differences between various metals and frequencies are determined only by the value of ξ. This allows easy and accurate prediction of waveguide resonance properties, without relying on complicated or time-consuming numerical calculations and simulation. Furthermore, it is easy to measure values of metal dielectrics and calculate values for ξ to incorporate in this analysis, and not rely on a Drude model.

This approach can also be generalized to apertures of arbitrary shape. The general solutions to the wave equation (Eq. 2.9) determine the functional form of the cavity modes, while the dispersion relation of Eq. 3.5a is generalized to

$$\epsilon\frac{\omega^2}{c^2} = k_z^2 + \gamma^2, \tag{3.33}$$

where γ, the generalized transverse wavevector, replaces the radial wavevector β. The value of γ is found by evaluating the perfect conductor boundary conditions (Eqs. 3.4) at a distance δ into the cavity walls, see Fig. 3.3(a). For particular geometries, it is also possible to decouple TE and TM modes as we have here.

Furthermore, the results derived here can be used in various numerical techniques. First of all, these results can be directly implemented in a rigorous coupled wave analysis (Chap. 5). In those calculations the SDBC and the transverse wavevectors are used to account for the metal properties in the field expansion. On the other hand, the rationale behind this approach is useful for simplifying complicated finite element calculations (Chap. 6).

Finally, these results will be used as part of a larger theoretical framework which completely describes enhanced optical transmission, i.e. to find the resonance and transmission response of apertures embedded in metallic films of finite thickness. For example, additional restrictions can be placed on k_z transforming the waveguide into a resonant cavity. These restrictions arise from boundary conditions across the aperture openings. A detailed analysis of these is discussed next in Chapter 4.

Chapter 4

The effective cavity resonance

4.1 Introduction

In this chapter we present a novel theoretical approach for modeling the resonant properties of transmission through subwavelength apertures penetrating metal films. We show that cavity mode theory applies to an effective resonant cavity whose dimensions are determined by the aperture's geometry and the evanescent decay lengths of the diffracted waves above and below the aperture. This method suggests a concrete physical mechanism for the enhanced transmission observed in periodic aperture arrays; namely it is the evanescently scattered light, localized in the near field at metal surfaces, which couples into the apertures. Furthermore, it analytically predicts the frequencies of peaks in enhanced transmission, the quality factor of the peaks, and explains their dependence on variation in the hole radius, periodicity, and the film thickness over a wide range of geometries. This model demonstrates strong correlation to simulation and existing results with high degree of accuracy.

4.1.1 Enhanced optical transmission

Enhanced optical transmission (EOT) is a electromagnetic effect, first reported by Ebbesen and coworkers in 1998 for visible light,[17] and in 1973 by Ulrich and Tacke for microwave frequency radiation.[37] In this effect, the fraction of incident electromagnetic radiation that is transmitted through a grating or array of subwavelength grooves or holes perforating a metal film or plate is larger than to be expecting considering the fractional surface area of the openings, hence the term "enhanced." That is, even if the open portions of the structure only make up 50% of the surface area of the top surface, for example, greater than 50% of incident light will be transmitted through. For microwave structures, where metals are nearly-lossless, the total transmission through the arrays can approach 100%. Additionally, the transmission through an array of holes is enhanced compared to the transmission through a single aperture.

There are a few properties of EOT that are worth discussing. First of all, this effect is generally a resonant-type effect, where the transmission enhancement occurs in some well-defined, narrow bandwidth around a resonance peak. This should be contrasted to transmission through a waveguide where light is guided at any frequency above cutoff. Furthermore, the position and width of these peaks are dependent on the structure's materials and geometry: periodicity, cavity cross-sectional shape (i.e. rectangular, circular), hole depth (i.e. metal thickness), and the choice of metal and dielectrics in, above, and below the apertures. Varying each of these parameters changes the resonance properties differently. As an extreme example, the transmission effect is "enhanced" with periodic structures as compared to a single aperture or groove (i.e. infinite periodicity).

Many theories have been proposed for the underlying physical mechanism (or mechanisms) that cause EOT; different approaches are applicable with different configurations. For example, Bethe's calculations apply to a single, extremely small hole through an infinitely thin perfect electric conducting (PEC) film.[38] Others have generalized this approach to account for periodic arrays,[39] and finite thicknesses.[40] However, these approaches are limited to extremely small holes and perfect conducting metals, two situations which are not typically realized.

To avoid the geometric and material limitations of approaches based on Bethe's theory, one common argument supposes that it is the excitation of surface plasmons (SP) on the periodic surface, both for one-dimensional gratings or two-dimensional aperture arrays, which allows coupling of light from an incident wave through the holes.[41–46] This approach explains the role that structure periodicity plays in EOT. However, it does not account for the variation in EOT due to aperture shape.[47, 48] Furthermore, EOT has been demonstrated with PEC structures, as well as non-metallic materials where SP contributions are nonexistent.[34, 49, 50]

Another approach describes the contribution to EOT of propagating waveguide modes along the aperture.[21, 29, 51–53] These arguments suppose that incident light can only propagate through a film and contribute to EOT in a manner which satisfies a propagating waveguide condition along the length of the aperture. These approaches capture some limitations that the individual cavity structures place on allowed frequencies which demonstrate EOT, but do not directly explain the effect of periodicity on EOT or predict the locations of specific peaks in EOT and their dependence on cavity shapes.

In spite of the theoretical uncertainty regarding the mechanisms of EOT, the effect has been studied extensively through use of a semi-analytical coupled wave analysis,[46, 54, 55] by many different finite element or finite difference numerical simulation approaches,[56, 57] and experimentally.[41–44, 46, 47] These methods all empirically shed light on the dependence of EOT on structure periodicity and cavity shapes, but do not provide an intuitive, or fundamentally clarifying approach toward the mechanisms of EOT. Furthermore, these approaches are often computationally and experimentally expensive to carry out.

Thus, a complete first-principles approach to explain the effect of EOT through two-dimensional arrays subwavelength holds in metal films is desirable. In this chapter we develop a novel approach which analytically and intuitively explains the physical mechanism of EOT, and completely explains the aforementioned dependence on structure periodicity and cavity shape. The theory is accurate over an extremely broad range of geometrical configurations. In this approach, we extend the idea of waveguide dispersion analysis to account for finite film thicknesses.

For a finite film, an impedance mismatch between the superstrate and the metal at the top and bottom of the cavities introduces a restriction on the possible wavelengths that can exhibit resonant behavior along the z-direction. It is at these resonances where light is strongly coupled into and through the apertures, where peaks in EOT are manifest. There have been some successful studies of cavity-type resonances for one-dimensional gratings, under limited geometrical conditions;[11, 36, 58–62] we extend this approach to two-dimensional arrays.

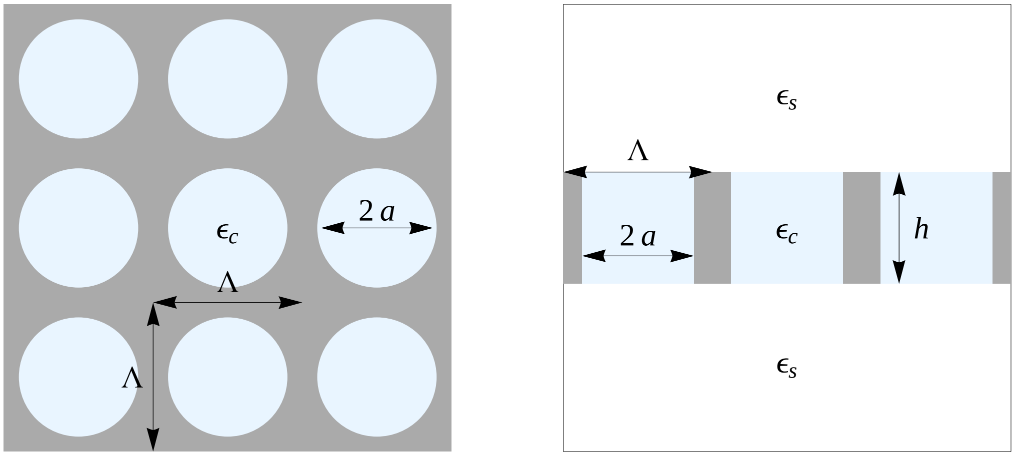

(a) A top-down view of the structure under consideration.

(b) A cross section view of the structure under consideration.

Figure 4.1: A schematic of periodic cylindrical channels in a thin film is shown from top down (a) and in cross section (b). The gray region represents the metal, the light blue regions are the dielectric-filled apertures, and the white is the superstrate and substrate.

Our goal is to describe an effective resonant cavity which has resonant properties that match that of the actual aperture array. It should be emphasized that this is not an *actual* cavity resonance, i.e. the fields do not demonstrate standing-wave behavior and there is a flow of energy along the aperture, but an effective cavity resonance (ECR) where the physical extents of the equivalent cavity are determined by the metamaterial's structural and material properties.

4.2 Effective cavity resonance solutions

Here we discuss cylindrical apertures of radius a, filled with dielectric ϵ_c embedded in a metal film of thickness h, arranged in an infinite square periodic lattice of period Λ, with a dielectric, ϵ_s, above and below the film, see Fig. 4.1. The approximation of infinite lattice is valid in practice as long as the size of an complete hole array is significantly larger than the wavelength of incident light, where we can neglect edge effects.[25] We additionally neglect any magnetic effects, taking $\mu = 1$ for all materials, and assume an implicit $\exp[-i\omega t]$ harmonic time dependence.

The dispersion relation of light within these structures is given by Eq. 3.5a. The transverse wavevector β is found by evaluating boundary conditions at the cavity's metal walls, as discussed in Chapter 3. The remainder of this chapter involves determining an appropriate restriction on k_z due to a finite film thickness. If the restriction forces k_z to take discrete values, it changes the allowed ω in Eq. 3.5a from a smoothly varying range of values to distinct resonance frequencies.

We emphasize again that this effective cavity resonance is not an actual *cavity* resonance. That is, there is no "standing-wave" behavior, as light is not stationary within the aperture, but instead propagates through it.

Nevertheless, there are still spatial restrictions to the fields which introduce a buildup in field strength within the cavity and can be modeled as an effective resonant cavity.

4.2.1 A simple, illustrative model

We first investigate a simple model for a restriction on k_z which sets up a resonance condition, which we will study in greater detail in Section. 4.2.2, and serves to illustrate our general approach. When incident light excites fields within the cavity, they induce surface currents (Eq. 3.21) oscillating upwards and downwards along the cavity walls. These currents have only a z-component, and, in the absence of charges ejected vertically from the surface, the net current in the z-direction must be zero at the top and bottom surfaces of the film. This changes the waveguide to an effective resonant (Fabry-Pérot) cavity of length h, introducing the restriction

$$k_z = p\,\pi/h, \tag{4.1}$$

where p is an integer.

Substituting this constrained value for the propagation constant into Eq. 3.5a gives a set of discrete resonance frequencies,

$$\omega_{mnp} = \frac{c}{\sqrt{\epsilon_c}}\left[\left(\frac{p\,\pi}{h}\right)^2 + \beta_{mn}^2\right]^{1/2}. \tag{4.2}$$

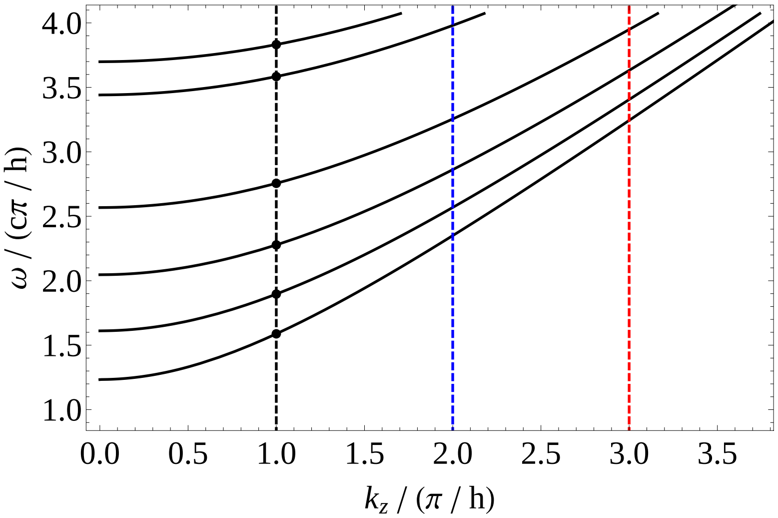

Figure 4.2: A graphical interpretation of the resonance condition described by Eq. 4.2. Vertical lines correspond to the k_z restricted by film thickness (Eq. 4.1), solid curves are the modal dispersion curves of the cylindrical cavities (Eq. 3.5a). The intersections of the two curves (points for $p = 1$ line) correspond to resonance conditions. Here $h/a = 2.1$.

Fig. 4.2 shows a graphical interpretation of this method. The dispersion curves are plotted, along with the restricted values for k_z from Eq. 4.1 which are vertical lines. The intersections between these curves correspond to resonance conditions for the effective cavity.

The frequency of light in the cavity, and the effective wavelength, $\lambda^{\text{eff}}_{mnp} \equiv 2\pi c/\omega_{mnp}$, are then functions of film thickness. Fig. 4.3 shows the effective wavelength in a cavity embedded in a PEC metal as a function of film thickness for the $p = 1$ resonance. For small thicknesses relative to the aperture radius, the permitted wavelength approaches zero, and the response of the

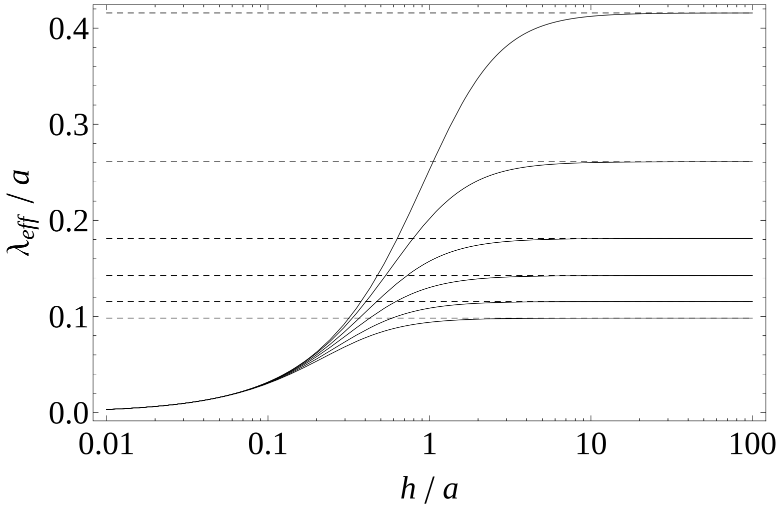

Figure 4.3: The effective wavelength (solid) in the cavity embedded in PEC is plotted (normalized with respect to cavity radius, a) as a function of film thickness (normalized with respect to cavity radius, a) for the $p = 1$ resonance. Dashed lines are the infinite-waveguide guided frequencies.

structure is dominated by the film thickness, with minor variation between the radial modes. On the other hand, as the cavity length increases relative to the aperture radius, the significance of the radial contribution grows, and the resonances approach the infinite-waveguide solutions (dashed lines). This behavior is qualitatively the same for non-PEC metals, with the exact functional form depending on the detailed dielectric properties of the metal.

4.2.2 A complete solution

The analysis in Section 4.2.1 ignores the contribution to the induced currents at the top surface due to the incident fields. Additionally, this solution does

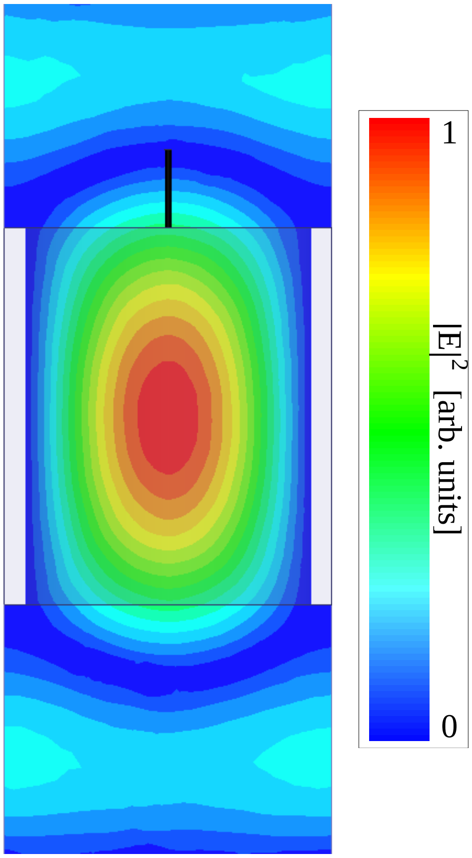

Figure 4.4: A cross-sectional slice of unit cell of a cylindrical cavity embedded in a PEC film is shown, with the magnitude of the electric field (in arbitrary units) plotted. Here $2a/\Lambda = 0.88$, $h/a = 2.63$ and the fields are evaluated at $\omega/(c\pi/h) = 1.72$. The solid black line, oriented along the z-direction above the film surface, is the predicted cavity field leakage depth.

not depend on periodicity, an effect which can not be neglected. Furthermore, a full field simulation (Fig. 4.4) shows that the fields of an ECR reach beyond the surface of the film, above and below, extending the effective height of the cavity. That is, if the concentrated fields extend a distance δ_e above and below the metal surface, the aperture has an effective height

$$h_{\text{eff}} = h + 2\delta_e, \tag{4.3}$$

which is the actual aperture height plus the total penetration depth into the superstrate and substrate, beyond which the cavity fields decay to zero.

Then, we substitute this effective cavity height in Eq. 4.1, giving the restriction

$$k_z = p\,\pi/h_{\text{eff}}, \tag{4.4}$$

where p is an integer. The distance the fields leak out of the cavity is determined by restrictions on the fields above and below the film, which depend explicitly on the periodicity of the apertures.

To find this distance, we must find the maximal spatial extent of localized fields in the superstrate. It has been pointed out that evanescent fields at the interface between the apertures and the superstrate and substrate play an important role in EOT, but the details of this mechanism is not completely understood.[34, 63] Here, we develop an approach which more completely describes the role of the evanescent fields, by describing the spatial extent of the cavity resonance in terms of the length added by the evanescent fields. These localized fields, unlike incident plane waves, are able to couple to waveguide modes in the cavity.

We note that, due to continuity boundary conditions between an aperture and the superstrate, single-walled aperture structures are unable to support the normally-incident TEM waves which strike them. Specifically, TEM waves have no z-component to their fields, while the fields in the apertures require a non-zero E_z (TM modes) or H_z (TE mode).[24] Likewise, light exiting an aperture can not directly excite a zero-order transmission plane wave. Nevertheless, as we discussed in Section 2.3, normally-incident light scatters from periodic arrays of subwavelength holes into Floquet modes.

Evanescent Floquet modes, where $(m^2 + n^2)K^2 > \epsilon_s \omega^2/c^2$, introduce strong localized fields above and below the metal film. These fields decay exponentially away from the surface with a decay length

$$\delta_{mn}\left(\omega, \Lambda\right) = 1/\mathrm{Im}[k^f_{zmn}(\omega, \Lambda)], \tag{4.5}$$

where k^f_z is given by Eq. 2.13c. In general, these scattered fields have non-zero z-components, which then interact with the fields inside the apertures. Thus, it is the strength of, and scattered, although localized, nature of the evanescent modes that drives the transmission through the film.

The maximal spatial extent of these localized fields then sets the penetration depth of the cavity fields into the superstrate and substrate. That is,

$$\delta_e(\omega, \Lambda) = \max\left[\delta_{mn}\left(\omega, \Lambda\right)\right]. \tag{4.6}$$

The inclusion of the max function picks the mode with the longest decay length which is, in general, the lowest-order non-propagating mode. Although the detailed behavior of the electromagnetic fields above and below the metal is due to a superposition of all evanescent and propagating Floquet modes, the *extent* of the localized fields is still limited by the lowest-order evanescent Floquet mode in the superstrate or substrate. This sets the maximal distance over which any evanescent Floquet modes can extend, and thereby the effective depth of the fields above and below the film.

Furthermore, this length depends explicitly on the periodicity, which directly explains both the enhancement seen for periodic structures, and the variation in EOT with changes of periodicity. We discuss this further in Section 4.3. This predicted length is shown in Fig. 4.4 as the solid black line, oriented along the vertical direction above the film surface, and is seen to match the field simulation. Additionally, note the field strength at that point matches the field strength at cavity walls, and thus describes the edge of the effective cavity.

There is one notable limitation of this approach, which we now discuss. At a frequency where the radicand in Eq. 2.13c is zero, i.e. a diffraction frequency,

$$\omega_{\text{diff}} = \frac{c\pi}{p\sqrt{\epsilon_s}}\sqrt{m^2 + n^2}, \tag{4.7}$$

the field leakage depth asymptotically approaches infinity, with a discontinuity at the diffraction frequency. This can be seen in Fig. 4.5, which shows the leakage depth as a function of frequency. The tendency towards infinite evanescent decay lengths captures the smooth transition from a localized mode to a propagating diffracted mode. However, approaching this transition makes the lowest order evanescent fields less local, while the second order (shorter decay length) evanescent fields are still localized. The actual effective cavity addition δ_e must then depend on the relative weights of the first- and second-order evanescent modes, which we do not analyze. Thus, we expect this model to break down at frequencies just below the diffraction frequencies. It is likely that this analysis can be improved by considering the scattering efficiencies into different Floquet modes. However, even without that addition, this model is still highly accurate for nearly all frequencies.

Using these results, we can rewrite Eq. 4.2 using the effective height of

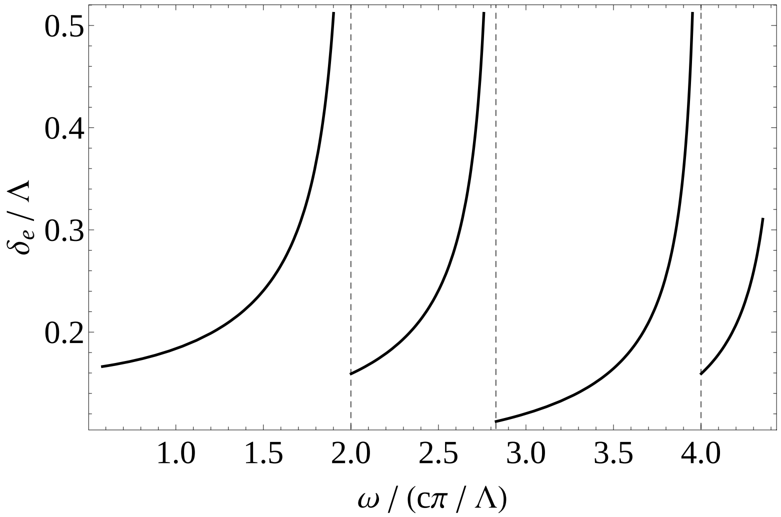

Figure 4.5: We plot the cavity field leakage length δ_e as a function of normalized frequency. Discontinuities at dashed vertical lines are the locations of the onset of propagating diffracted modes.

Eq. 4.3,

$$\omega_{mnp} = \frac{c}{\sqrt{\epsilon_c}} \left[\left(\frac{p\,\pi}{h + 2\delta_e(\omega_{mnp})} \right)^2 + \beta_{mn}^2 \right]^{1/2} . \tag{4.8}$$

Since the effective height is itself a function of frequency, it is difficult to find an exact solution for ω in all cases. Nevertheless, due to the analytic nature of this expression, we are still able to extract general trends in resonance changes due to cavity geometry. For ease of interpretation, we utilize the graphical approach discussed earlier. In Fig. 4.6 the dispersion curves are plotted, along with the restricted k_zs from Eq. 4.4 which are the dashed lines. The intersections between these curves correspond to resonance conditions for the effective cavity.

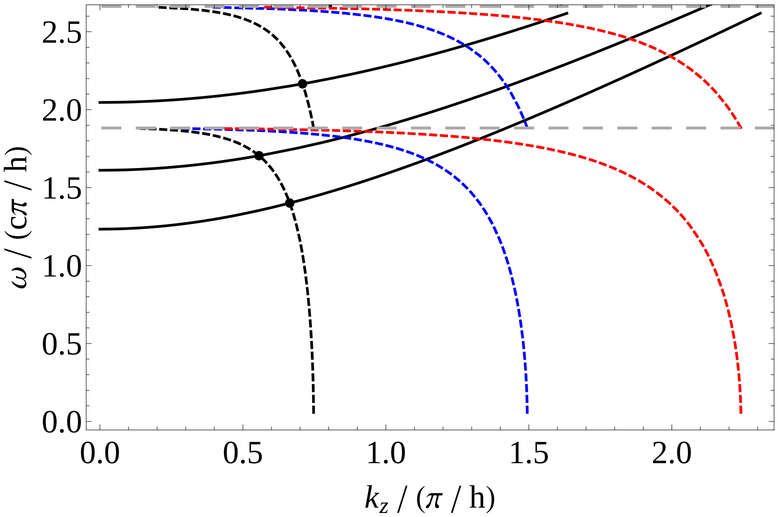

Figure 4.6: A graphical interpretation of the resonance condition described by Eq. 4.8. Dashed lines correspond to the k_z restricted by film thickness (Eq. 4.4), solid curves are the modal dispersion curves of the cylindrical cavities (Eq. 3.5a). The intersections of the two curves (points for $p = 1$ line) correspond to resonance conditions. Here $h/a = 2.1$.

Until this point we have been analyzing open apertures in metal films. We feel it is also worthwhile briefly noting that this approach can be applied to closed cavities, as well, with a different effective height,

$$h_{\text{eff}} = h + \delta_e + \delta_m, \tag{4.9}$$

where δ_m is the field penetration depth into the metal (i.e. the skin depth Eq. 3.1), and where we follow the key assumption in Chapter 3, neglecting fields beyond a skin depth into metal. Then, Eq. 4.2 becomes:

$$\omega_{mnp} = \frac{c}{\sqrt{\epsilon_c}} \left[\left(\frac{p\,\pi}{h + \delta_e(\omega_{mnp}) + \delta_m(\omega_{mnp})} \right)^2 + \beta_{mn}^2 \right]^{1/2}. \tag{4.10}$$

4.3 ECR dependence on structure geometry

Figure 4.7 shows the dispersion curves, Eq. 3.5a, overlaid with the restricted k_z condition, Eq. 4.4, for different geometries. Note the discontinuity in the k_z restriction at diffraction frequencies due to the limitations of the theory discussed earlier. The dependence of EOT peaks on cavity radius is found in Eq. 3.5a; the radius only affects the waveguide mode dispersion. Thus, keeping the film thickness and periodicity fixed, and changing the radius, shifts only the modal dispersion curve up or down, see Fig. 4.7(a). As the radius decreases, the allowed waveguide modes shift to higher frequencies, as expected. However, the rate of shifting is not uniform, in contrast to the illustrative model discussed in Section 4.2.1, and smaller shifts are found for the same change in radius as the resonance approaches a diffraction frequency. Also, note that the dielectric in the cavity enters these calculations by shifting the dispersion curve towards lower frequencies with higher dielectrics.

Changing the period or film thickness leaves the waveguide modal dispersion curve untouched, shifting only the restriction on k_z due to the effective cavity height. The relative size of h and δ_e determine the dominant contribution to the effective length. When h is large relative to δ_e, i.e. thick films, the resonance approaches the simpler model discussed earlier, where the dominant length is in the waveguide. When δ_e is large, i.e. extremely thin films or near diffraction, the effects of periodicity dominates the transmission spectrum.

Increasing the thickness of the film pushes the k_z restriction curve closer to the straight vertical lines of Fig. 4.2. However, the lines never do reach $p\pi/h$ as there is always some field coupling depth, see Fig. 4.7(c). The smooth transition from the enhanced transmission of a periodic structure, to propagation along regular, independent waveguides can be seen.

Increasing the period shifts the first diffraction towards lower frequencies, drastically changing the curvature of this restriction curve, see Fig. 4.7(b). This, in turn, shifts all resonances towards lower frequencies, with the most drastic changes occurring close to diffraction frequencies. As the period increases further, it pushes down the diffraction frequencies, and thereby increases the density of restricted k_z lines crossing the dispersion curves. It should also be noted that expected transmission through a film drops above a diffraction frequency. If the lowest order scattered Floquet mode is a propagating mode, it not only carries energy away from the structure, but it also leaves proportionally less electromagnetic energy to be scattered into the lowest order evanescent mode, thus decreasing the available localized light which can be coupled to the ECR. This effect introduces an important design restriction when designing compound cavity array structures. Namely, it is important that all desired effects occur below the onset of diffraction; we discuss this further in Part III. Also, note that the dielectric in the superstrate or substrate enters these calculations by increasing the effective height with higher dielectric values.

This result further explains the differences in EOT between periodic and single apertures. As the period approaches infinity (i.e. single apertures), the discrete transverse Floquet wavevectors $\sqrt{(m^2 + n^2)K^2}$ can be made arbitrarily close together and can be considered a continuous variable which varies smoothly between 0 and $\epsilon_s \omega^2/c^2$. This leads to an infinite continuum of propagating reflected modes (i.e. a spherical scattered wave) and the number of evanescently decaying modes approaches zero. However, it is precisely via these evanescent fields that light is coupled into, and ultimately out of the cavity. Thus, as the periodicity increases, the number of modes which permit EOT approaches zero, leading to the expected weaker overall coupling and lower transmission.

4.4 Comparison to simulation

It is straightforward to numerically find the roots to Eq. 4.8 and calculate the dependence of peaks in EOT on geometrical properties over a large range

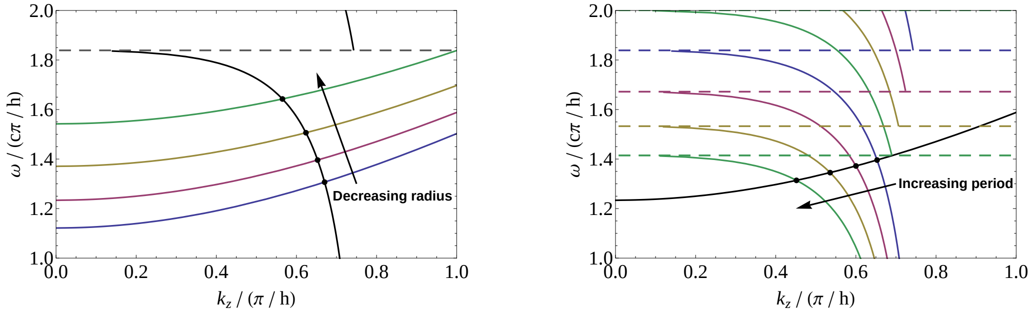

(a) Effect of varying the radius. Arrow points along direction of decreasing radius with $2a/\Lambda$ of 0.7, 0.79, 0.87, and 0.96 plotted. Here $h/\Lambda = 0.92$, the black line is the k_z restriction from film thickness, and the colored lines are the different waveguide modal dispersion curves.

(b) Effect of varying the periodicity. Arrow points along direction of increasing periodicity with p/h of 0.87, 0.96, 1.04, and 1.13 plotted. Horizontal dashed lines are the diffraction frequencies for each period. Here $h/a = 2.63$, the black line is the waveguide modal dispersion curve, and the colored lines are the k_z restrictions from film thickness.

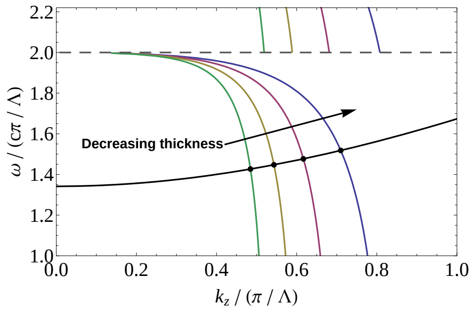

(c) Effect of varying the film thickness. Arrow points along direction of increasing thickness with h/a of 2.11, 2.63, 3.16, and 6.32 plotted. Here $2a/\Lambda = 0.87$, the black line is the waveguide modal dispersion curve, and the colored lines are the k_z restrictions from film thickness.

Figure 4.7: Graphical interpretation of the variation in the resonance condition due to changes in radius (a), periodicity (b), and film thickness (c).

of values. To verify the predictions, we simulated structures using HFSS, which is a commercially available full-wave finite element simulation tool. We simulate periodic cylindrical apertures embedded in idealized PEC metal film as well as cavities in a realistic gold film.

Figure 4.8 compares the simulated transmission through a PEC film with $\epsilon_c = \epsilon_s = 1$, overlayed with predicted peaks of EOT. There is extremely strong agreement between the predicted and simulated results, over a wide range of geometries. Any major differences between predicted and simulated values occur at frequencies very close to diffraction frequencies, which is a manifestation of the limitation of this theory discussed earlier. It is also worth noting that for extremely thin films, the resonance broadens significantly towards lower frequencies. This is due to the contribution of evanescent waveguide modes (i.e. below cutoff) where the decay length along the aperture is large compared to the film thickness, as discussed in Chapter 3.

Note, that the subwavelength condition $2a/\lambda < 1$ is given in the normalized coordinates of Fig. 4.8(a) by

$$\left(\frac{2a}{\Lambda}\right)\left(\frac{\omega}{c\pi/h}\right) < 2\left(\frac{h}{\Lambda}\right). \tag{4.11}$$

Similarly, in the normalized coordinates of Fig. 4.8(b) by

$$\left(\frac{\omega}{c\pi/h}\right) < \left(\frac{h}{a}\right), \tag{4.12}$$

and in the normalized coordinates of Fig. 4.8(c) by

$$\left(\frac{\omega}{c\pi/\Lambda}\right) < 2\left(\frac{2a}{\Lambda}\right)^{-1}, \tag{4.13}$$

Then, the plotted range of values in Fig. 4.8 are entirely within the subwavelength regime. The existence of EOT through subwavelength PEC structures, where SP resonance is not a contributing factor, further highlights the minimal role of SPs in aperture array EOT. The ECR can be viewed as the dominant mechanism which enhances transmission for this class of structures. While there are some structures which are well-described by a SP model, this analysis demonstrates that a wide variety of structures do not require SP resonances to create enhanced transmission.

As further verification of the validity of this approach, we compare the predictions of this model as it applies to cavities in metal, as per Eq. 4.10. Figure 4.9 compares the simulated specular reflection from a gold film with $\epsilon_s = 2.1$ and $\epsilon_c = 2.1 + i\,0.9$, overlayed with predicted peaks of EOT. We introduced loss in the cavity dielectric to better identify the resonances; when there are strong fields built up in the cavity there is increased loss in the dielectric. There is reasonably close agreement between the predicted and simulated results. The weakest agreement is found upon varying the radius. Due to the fairly large skin depths of gold at optical frequencies, there is a

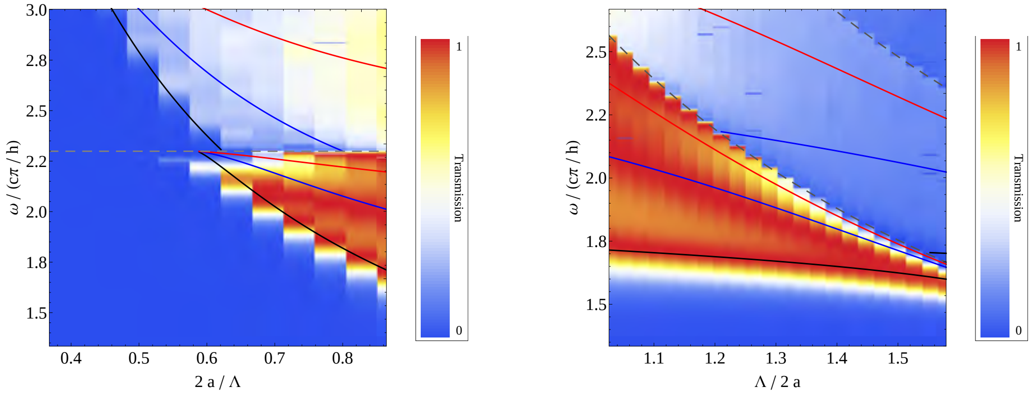

(a) Effect of varying the radius. Here $h/\Lambda = 0.92$.

(b) Effect of varying the periodicity. Here $h/a = 2.63$.

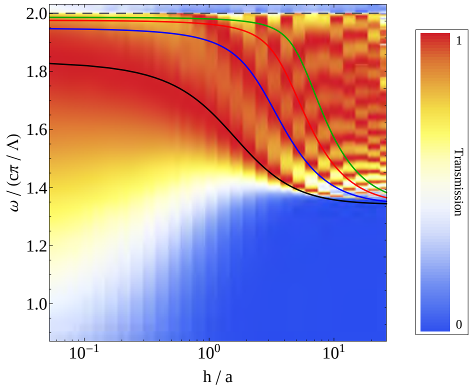

(c) Effect of varying the film thickness. Here $2a/\Lambda = 0.87$.

Figure 4.8: Simulated zero-order transmission through cylindrical apertures embedded in PEC, overlayed with predicted ECR peaks. The gray dashed lines are diffraction frequencies, and the black, blue and red (and green) colored lines are the lowest order TE_{11p} curves for p=1,2,3 (and 4) respectively as a function of radius (a), periodicity (b) and film thickness (c).

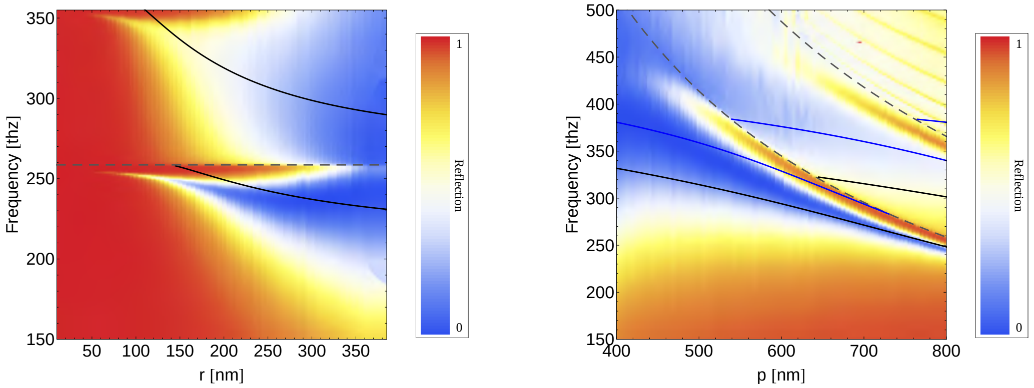

(a) Effect of varying the radius. Here $h = 250$ nm and $\Lambda = 800$ nm.

(b) Effect of varying the periodicity. Here $h = 250$ nm and $a = 190$ nm.

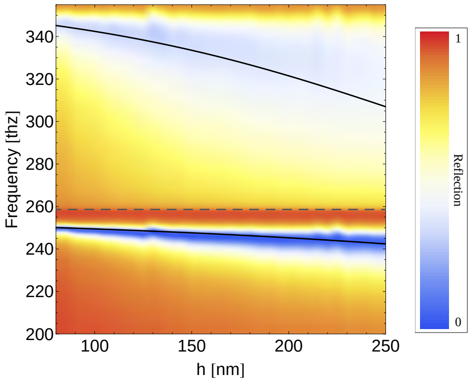

(c) Effect of varying the film thickness. Here $a = 190$ nm and $\Lambda = 800$ nm.

Figure 4.9: Simulated specular reflection from an array of cylindrical holes embedded in gold, overlayed with predicted ECR peaks. The gray dashed lines are diffraction frequencies, the black and blue lines are the lowest order TE_{111} and TM_{011} curves, respectively as a function of radius (a), periodicity (b) and film thickness (c).

small range of values where a/δ_m is large, while $2a/\Lambda$ remains small. When these conditions are not satisfied, a large fraction of the fields are contained within the metal, and the ECR model and SDBC would not apply. Any other differences between predicted and simulated values occur at frequencies very close to diffraction frequencies, which is a manifestation of the limitations of this theory discussed earlier in Section 4.2.2.

4.5 Calculating the quality factor of the ECR

Now that we are able to calculate the resonance frequencies of the effective cavities, it is possible to calculate the quality factor, Q, of the effective resonance. Here we use the expression,

$$Q = \omega_{mnp} \frac{U}{P_{\text{loss}}}, \tag{4.14}$$

where ω_{mnp} is a particular resonance frequency found using Eq. 4.8, U is the time-averaged energy stored within the aperture and P_{loss} is the time-average power lost.[24] Putting together Eqs. 2.8, 2.10a, and 4.4, we have

$$\psi_{mnp} = e^{-i(p\pi/h_{\text{eff}})z} e^{im\varphi} J_m \left(\beta_{mn} r\right), \tag{4.15}$$

and we can calculate both the energy stored and power lost.

The energy stored in the aperture is

$$U_{mnp}^{\text{low}} = \frac{C}{4\pi} \left[\epsilon \frac{\omega_{mnp}^2}{c^2} \frac{1}{\beta_{mn}^2}\right] \frac{h}{4} \iint \left|\psi_{mnp}\right|^2 r dr\, d\varphi, \tag{4.16a}$$

where the integral is taken over the aperture face, and where $C = 1$ for TE modes and $C = \epsilon$ for TM modes.[24] Note, that this only the energy stored within the metallic bounds of the aperture (i.e. we use h for the cavity height), and is thus is really a lower bound for the energy stored. However, as there is some energy stored in the evanescent fields above and below the aperture, an upper bound for the stored energy includes these fields (i.e. we use h_{eff} for the cavity height):

$$U_{mnp}^{\text{high}} = \frac{C}{4\pi}\left[\epsilon\frac{\omega_{mnp}^2}{c^2}\frac{1}{\beta_{mn}^2}\right]\frac{h_{\text{eff}}}{4}\iint|\psi_{mnp}|^2\,rdr\,d\varphi. \tag{4.16b}$$

Using these two values yields an upper and lower bound for the quality factor.

The power lost from the aperture is due to two sources: transmission out of the bottom face of the aperture and losses at the metal walls, the latter of which only exists with non-PEC metals. We do not consider the loss from the upper face of the aperture. The reason for this is apparent from the PEC case where we find 100% transmission through the film at resonance. This means that an equal amount of power flows through the top face of the apertures as through the bottom, with the same directionality. Since the unit normal vectors pointing out of the cavity are equal in magnitude but opposite in direction at the top an bottom faces, the total power flow *out* of the cavity is zero. This would correspond to an infinite Q, which must be rejected outright. Thus, we assume that, at resonance, whatever power enters the aperture at the top face must exit from the bottom or be absorbed in the walls. It is worthwhile noting, however, that this argument does not assume that for all circumstances 100% of incident light couples into the cavity, just that any light that is coupled is either transmitted or absorbed.

This result allows us to greatly simplify the calculation for P_{loss}, as we need not directly solve for the flow of power into the metal walls. Given that all energy which enters the apertures from the top surface must either be absorbed in the metal or transmitted out of the aperture, the power lost must be equal to the power incident, P, and it is sufficient to set $P_{\text{loss}} = P$. The incident power is,

$$P_{mnp} = \frac{C}{4\pi}\frac{c}{2\sqrt{\epsilon}}\left[\epsilon\frac{\omega_{mnp}^2}{c^2}\frac{1}{\beta_{mn}^2}\right] \times \sqrt{1-\left[\epsilon\frac{\omega_{mnp}^2}{c^2}\frac{1}{\beta_{mn}^2}\right]^{-1}} \iint \left|\psi_{mnp}\right|^2 r dr\, d\varphi \quad (4.17)$$

which is also the power lost.[24]

Substituting Eqs. 4.16 and 4.17 into Eq. 4.14 gives an expression for the bounds of Q for a particular resonance,

$$Q_{mnp}^{\text{low}} = \frac{hh_{\text{eff}}}{2}\frac{\epsilon}{p\pi}\frac{\omega_{mnp}^2}{c^2} \quad (4.18)$$

and

$$Q_{mnp}^{\text{high}} = \frac{h_{\text{eff}}^2}{2}\frac{\epsilon}{p\pi}\frac{\omega_{mnp}^2}{c^2}. \tag{4.19}$$

Note that Q is proportional to the resonance frequency squared. Thus, for an otherwise identical structure, transitioning from a PEC to a real metal decreases the resonance frequency, and thus decreases the Q which implicitly captures the metallic losses. This, furthermore, captures the dependence of the quality factor on the various geometrical parameters.

We can use this result to predict the bandwidth and resonance line shape for each resonance. We assume that the transmission line shape matches the line shape of energy in a cavity,[24]

$$|E(\omega)|^2 \propto \frac{1}{(\omega - \omega_{mnp})^2 + (\omega_{mnp}/2Q_{mnp})^2}. \tag{4.20}$$

Figure 4.10 shows simulated transmission through a particular geometrical configuration with the calculated Q, normalized and superimposed over the transmission curve. There is very strong agreement between the predicted response and the simulated transmission; the slightly wider simulated transmission peaks are due to the fact that the complete transmission spectrum is given by a superposition of the two resonances.

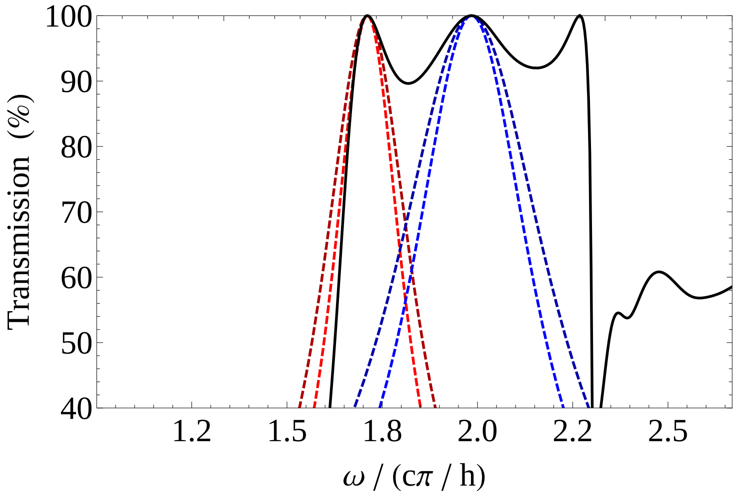

Figure 4.10: The transmission curve (solid black) for an aperture in PEC, with $2a/\Lambda = 0.87$, and $h/\Lambda = 1.15$. The red and blue dashed curves are the normalized resonant line shape for the TE_{111} and TE_{112} resonances for both the upper (lighter) and lower (darker) bounds of Q.

4.6 Summary and conclusion

We have presented a new analytical theory for the mechanism of enhanced optical transmission through arrays of subwavelength apertures. This theory demonstrates that an effective cavity is described by the cavity dimensions in conjunction with the decay length of strong, localized evanescent Floquet modes in the regions above and below the metal film. These localized fields are the primary cause for coupling light between the apertures and the other regions. Thus, this model is a fundamental theory for a mechanism of non-surface plasmon EOT.

Furthermore, we have shown how to predict the frequencies where peaks in enhanced transmission occur and how these frequencies depend on the cavity dimensions, metal choice, as well as periodicity of the structure. This model is valid over an extremely broad range of geometries, limited only at frequencies close to diffraction. We have shown strong agreement between our theory and simulations for both apertures through PEC and cavities embedded in real gold.

Although the model was applied to cylindrical apertures, this approach can be generalized to apertures of arbitrary shape. Other apertures change the value of the transverse wavevector β in dispersion relation of Eq. 3.5a, leaving everything else unchanged. Similarly, this can be generalized to rectangular (Eq. 3.5b), and perhaps arbitrary, periods, changing only the reciprocal lattice vectors in Eqs. 2.13. Likewise, the dependence of EOT on incident angle can be deduced from the changes this makes to the propagation vectors in the superstrate.

Part II

Numerical Techniques

Chapter 5

Rigorous coupled wave analysis

5.1 Introduction

The rigorous coupled wave analysis has been known in one form or another for quite some time.[64] Variations on this semi-analytic approach have been developed and used extensively for modeling grating and aperture array metamaterials.[46, 54, 55, 65] In this approach, the incident and unknown fields are written in different regions as linear combinations of orthogonal basis functions. Application of appropriate electromagnetic boundary conditions over all of the shared interfaces relates the fields in various regions.

Many approaches expand the fields in all regions only in terms of the Floquet mode solutions.[64, 66–69] In our approach, we will expand the electric and magnetic fields in terms of different sets of basis functions in the different regions.[46, 70] This approach requires fewer terms in the expansion to converge to a physical result than the former approach. However, it requires calculating the overlap integrals between different sets of basis functions, which often must be computed numerically.

Our approach to the RCWA is not fundamentally different than existing approaches. One significant difference, however, is in the choice of metal boundary conditions. We make use a surface impedance boundary condition (SIBC),[24, 71–73] as well as the SDBC, see Chapter 3. This approach allows a simpler expansion of the fields inside the cavity than some other approaches.

5.2 Solution strategy

Our approach to the RCWA relies on our knowledge of the field's behavior in various regions; we will therefore expand both the electric and magnetic fields in terms of sets of basis functions appropriate for each region. Namely, in the superstrate, where we expect the overall far-field to behave largely like plane waves, we expand the fields – both incident and scattered – in terms of basis sets of Floquet modes (Eq. 2.15). In the cavities, however, it is more natural to expand the fields in terms of waveguide modes (Eq. 2.8).

Here, we will apply the SDBC at the metal surfaces inside the aperture or cavity. At the top and bottom metal surfaces, facing the superstrate, we apply the SIBC

$$\mathbf{E}_t = \mathcal{Z}\hat{\mathbf{n}} \times \mathbf{H}_t, \tag{5.1}$$

where $\mathcal{Z} = 1/n$ is the impedance of the metal, where n is the, in general complex, index of refraction of the metal, $\mathbf{E}_t$ and $\mathbf{H}_t$ are the electric and magnetic fields tangent to the interface and $\hat{\mathbf{n}}$ is the unit normal out of the metal ($\hat{\mathbf{z}}$ on the top interface, $-\hat{\mathbf{z}}$ on the bottom).

Additionally, we require continuity of the transverse electric fields and magnetic fields – subject to the continuity condition Eq. 3.22 where $\mathbf{J} = 0$ – across any cavity-superstrate or aperture-substrate interface. Then multiplying the resulting relationships by orthogonal basis functions and integrating over the interfaces will eventually yield a set of equations for the unknown field expansion coefficients in terms of the incident conditions.

5.2.1 Polarization schemes

It useful to decompose an arbitrary electromagnetic field into two orthogonal polarizations. Waveguide fields are usually broken down into TM ($H_z = 0$) and TE ($E_z = 0$) polarizations. In general, TEM ($H_z = 0$ and $E_z = 0$) cavity polarizations can also exist, but for cavities of a single surface these modes are non-existent. For coaxial and grating-type structures, on the other hand, TEM modes must be included. These cavity polarizations are linearly independent; transverse fields for each polarization are uniquely specified by the z-components of the field, see Eq. 2.7. Therefore, any arbitrary field within the cavities with both E_z and H_z components can be split into TM and TE parts, and once E_z and H_z are known, the remaining field components for each polarization can be calculated separately and independently of the other.

We will likewise separate the fields in the superstrate into these two polarizations. Then, an incident plane wave with TM polarization in the superstrate, for example, has a E_z component while $H_z = 0$. Continuity of the E and H fields across the cavity interface ensures that the only cavity modes that can *directly* couple with this incident TM plane wave are ones with $H_z = 0$, namely cavity TM modes. Then, the TE cavity modes, likewise, will only directly interact with an incident plane wave with TE polarizations where $E_z = 0$.

However, scattered fields produced by this TM incident wave can, in general, have H_z components. But, in order to satisfy the condition that the net $H_z = 0$, for a given scattered field with $H_z \neq 0$, there must be other fields with equal and opposite H_z components. This leaves us, though, with the existence of scattered or diffracted fields of both polarizations for an incident beam having a single polarization, and thus an incident TM wave can, *indirectly*, couple to TE cavity modes through scattered fields.

As an illustrative example, we'll consider a normally-incident plane wave. This beam has a TEM polarization; both E and H must be perpendicular to the incident $\mathbf{k}_0^f = k\hat{z}$ vector, thus there is neither an H_z nor an E_z component to the fields. This implies is that the incident beam can not *directly* couple to *any* cavity modes. However, scattered fields can have both H_z and E_z, and even a TEM beam can couple to both TM and TE polarizations. Thus, it is through scattering that coupling between TE and TM modes arises, even for non-normal incident waves. In practice, as discussed in Chapter 4, it is the evanescent scattered fields that are the dominant contributors to cavity excitations.

5.2.2 Floquet modes in Cartesian coordinates

For the purposes of this chapter, in the interest of readability, we will drop the explicit superscript f notation on Floquet mode wave vectors, unless there is a particular need. We also assume a rectangular lattice, such that Eqs. 2.13 become:

$$k_{xm} = k_0 \sin\varphi_i \cos\theta_i + \frac{2m\pi}{\Lambda_x}, \tag{5.2a}$$

$$k_{yn} = k_0 \sin\varphi_i \sin\theta_i + \frac{2n\pi}{\Lambda_y}, \tag{5.2b}$$

and

$$k_{zmn} = \sqrt{\epsilon \kappa_0^2 - k_{xm}^2 - k_{yn}^2}, \tag{5.2c}$$

where φ_i is the inclination and θ_i is the azimuthal angle of the incoming wavevector. Additionally, we can write inclination and azimuthal angles of scattered waves (when $\varphi \neq 0$, $m \neq 0$, and $n \neq 0$) as

$$\sin\theta_{mn} = \frac{k_{yn}}{\sqrt{k_{xm}^2 + k_{yn}^2}}, \tag{5.3a}$$

$$\cos\theta_{mn} = \frac{k_{xm}}{\sqrt{k_{xm}^2 + k_{yn}^2}}, \tag{5.3b}$$

$$\sin\varphi_{mn} = \frac{\sqrt{k_{xm}^2 + k_{yn}^2}}{\sqrt{\epsilon}\kappa_0} = \sqrt{1 - \xi_{mn}^2}, \tag{5.3c}$$

$$\cos\varphi_{mn} = \frac{k_{zmn}}{\sqrt{\epsilon}\kappa_0} = \xi_{mn}, \tag{5.3d}$$

see Fig. 5.1(a).

Now, for the TM polarization, we write all the fields in terms of the magnitude of the magnetic field, H_{mn}^{TM}, see Fig. 5.1(b). Here we relate the magnitude of the electric field E_{mn}^{TM} to the magnetic field using Eq. 2.3d.

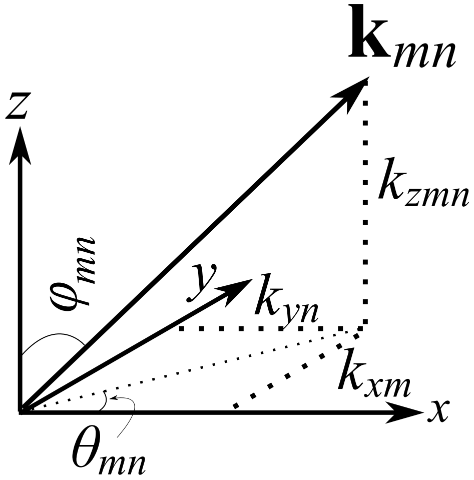

(a) An arbitrary wave vector.

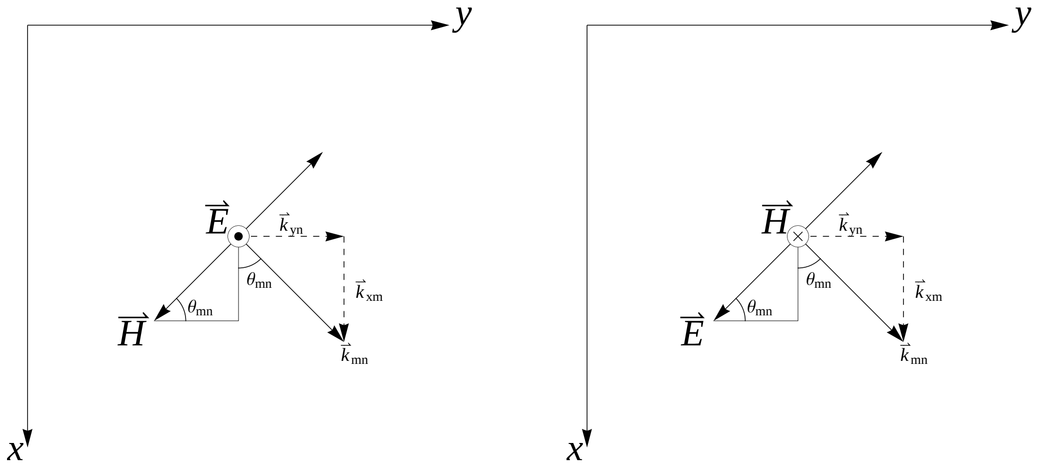

(b) The wave vectors in TM polarization. (c) The wave vectors in TE polarization.

Figure 5.1: Geometry of the Floquet mode wave vectors.

Hence,

$$E_{zmn}^{TM} = \pm H_{mn}^{TM} \frac{1}{\sqrt{\epsilon}} \sin\varphi_{mn}, \tag{5.4a}$$

$$E_{xmn}^{TM} = \mp H_{mn}^{TM} \frac{1}{\sqrt{\epsilon}} \cos\theta_{mn} \cos\varphi_{mn}, \tag{5.4b}$$

$$E_{ymn}^{TM} = \mp H_{mn}^{TM} \frac{1}{\sqrt{\epsilon}} \sin\theta_{mn} \cos\varphi_{mn}, \tag{5.4c}$$

$$H_{zmn}^{TM} = 0, \tag{5.4d}$$

$$H_{xmn}^{TM} = +H_{mn}^{TM} \sin\theta_{mn}, \tag{5.4e}$$

$$H_{ymn}^{TM} = -H_{mn}^{TM} \cos\theta_{mn}. \tag{5.4f}$$

$$\tag{5.4g}$$

Regarding the choice of sign in the latter three equations, the upper symbol refers to upward propagating and the lower symbol to downward propagating waves. We continue this notation for the remainder of this chapter. Similarly, for the TE polarization, we write all the fields in terms of the magnitude of the electric field, E_{mn}^{TM}, see Fig. 5.1(c). Here we relate the magnitude of the electric field E_{mn}^{TM} to the magnetic field using Eq. 2.3c. Hence,

$$E_{zmn}^{TE} = 0, \tag{5.5a}$$

$$E_{xmn}^{TE} = E_{mn}^{TE} \sin\theta_{mn}, \tag{5.5b}$$

$$E_{ymn}^{TE} = -E_{mn}^{TE} \cos\theta_{mn}, \tag{5.5c}$$

$$H_{xmn}^{TE} = \pm E_{mn}^{TE} \sqrt{\epsilon} \cos\theta_{mn} \cos\varphi_{mn}, \tag{5.5d}$$

$$H_{ymn}^{TE} = \pm E_{mn}^{TE} \sqrt{\epsilon} \sin\theta_{mn} \cos\varphi_{mn}, \tag{5.5e}$$

$$H_{zmn}^{TE} = \mp E_{mn}^{TE} \sqrt{\epsilon} \sin\varphi_{mn}. \tag{5.5f}$$

For normally incident or reflected, TEM waves, we retain two independent polarizations, expanded in terms of H_{mn}^{TM} or E_{mn}^{TE}, which we still refer to as TM and TE, even though the z-components of both fields are zero.

5.3 Field expansions

With all this, we are now able to expand the fields in the superstrate, substrate, and cavity in terms of appropriate basis sets. Here we assume the cavities or apertures are of height h, centered around $z = 0$, see Fig. 5.2

5.3.1 Fields in the superstrate and substrate

We can now expand both the electric and magnetic fields in the superstrate, and in substrate for open channels, as the sum of the TM and TE Floquet

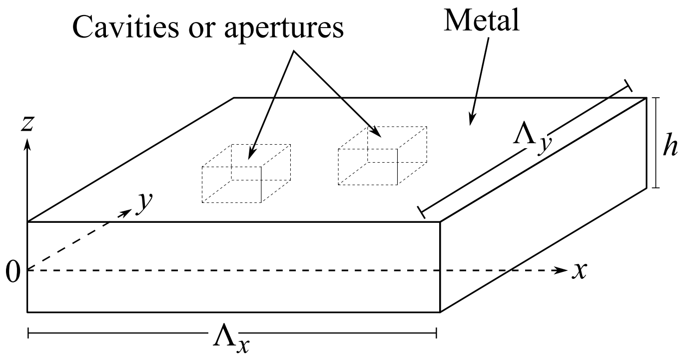

Figure 5.2: A schematic of a geometry that is described in this analysis.

modes. As a notation convention, in the expressions for incident waves, which in our geometry are downward propagating, we will replace the H_{mn}^{TM} expansion coefficients with I_{mn}^{TM} and the E_{mn}^{TE} expansion coefficients with I_{mn}^{TE}. We assume that the superstrate, defined by the region $z > h/2$ above the metal film, is filled with a dielectric ϵ_a, so here,

$$\begin{aligned} k_{zmn} &= \sqrt{\epsilon_a \kappa_0^2 - k_{xm}^2 - k_{yn}^2} \\ &= \xi_{mn} \sqrt{\epsilon_a} \kappa_0, \end{aligned} \tag{5.6}$$

where

$$\xi_{mn} \equiv \sqrt{1 - \frac{k_{xm}^2 + k_{yn}^2}{\epsilon_a \kappa_0^2}}. \tag{5.7}$$

Then the six electric and magnetic field components can be written,

$$\begin{aligned} E_z^{\text{super}} = &\sum_{m,n} \left(-\frac{1}{\sqrt{\epsilon_a}} \sqrt{1 - \xi_{mn}^2} I_{mn}^{TM} \right) e^{i[k_{xm}x + k_{yn}y - k_{zmn}(z-h/2)]} \\ &+ \sum_{m,n} \left(\frac{1}{\sqrt{\epsilon_a}} \sqrt{1 - \xi_{mn}^2} H_{mn}^{TM} \right) e^{i[k_{xm}x + k_{yn}y + k_{zmn}(z-h/2)]}, \end{aligned} \tag{5.8a}$$

$$\begin{aligned} E_x^{\text{super}} &= \sum_{m,n} \left(-\frac{1}{\sqrt{\epsilon}_a} \xi_{mn} \cos\theta_{mn} I_{mn}^{TM} + \sin\theta_{mn} I_{mn}^{TE} \right) e^{i[k_{xm}x + k_{yn}y - k_{zmn}(z-h/2)]} \\ &+ \sum_{m,n} \left(\frac{1}{\sqrt{\epsilon}_a} \xi_{mn} \cos\theta_{mn} H_{mn}^{TM} + \sin\theta_{mn} E_{mn}^{TE} \right) e^{i[k_{xm}x + k_{yn}y + k_{zmn}(z-h/2)]}, \end{aligned} \tag{5.8b}$$

$$\begin{aligned} E_y^{\text{super}} &= \sum_{m,n} \left(-\frac{1}{\sqrt{\epsilon}_a} \xi_{mn} \sin\theta_{mn} I_{mn}^{TM} - \cos\theta_{mn} I_{mn}^{TE} \right) e^{i[k_{xm}x + k_{yn}y - k_{zmn}(z-h/2)]} \\ &+ \sum_{m,n} \left(\frac{1}{\sqrt{\epsilon}_a} \xi_{mn} \sin\theta_{mn} H_{mn}^{TM} - \cos\theta_{mn} E_{mn}^{TE} \right) e^{i[k_{xm}x + k_{yn}y + k_{zmn}(z-h/2)]}, \end{aligned} \tag{5.8c}$$

$$\begin{aligned} H_z^{\text{super}} &= \sum_{m,n} \left(\sqrt{\epsilon}_a \sqrt{1-\xi_{mn}^2} I_{mn}^{TE} \right) e^{i[k_{xm}x + k_{yn}y - k_{zmn}(z-h/2)]} \\ &+ \sum_{m,n} \left(-\sqrt{\epsilon}_a \sqrt{1-\xi_{mn}^2} E_{mn}^{TE} \right) e^{i[k_{xm}x + k_{yn}y + k_{zmn}(z-h/2)]}, \end{aligned} \tag{5.8d}$$

$$\begin{aligned} H_x^{\text{super}} &= \sum_{m,n} \left(\sin\theta_{mn} I_{mn}^{TM} - \sqrt{\epsilon_a}\, \xi_{mn} \cos\theta_{mn} I_{mn}^{TE} \right) e^{i[k_{xm}x + k_{yn}y - k_{zmn}(z-h/2)]} \\ &+ \sum_{m,n} \left(\sin\theta_{mn} H_{mn}^{TM} + \sqrt{\epsilon_a}\, \xi_{mn} \cos\theta_{mn} E_{mn}^{TE} \right) e^{i[k_{xm}x + k_{yn}y + k_{zmn}(z-h/2)]}, \end{aligned} \tag{5.8e}$$

$$\begin{aligned} H_y^{\text{super}} &= \sum_{m,n} \left(-\cos\theta_{mn} I_{mn}^{TM} - \sqrt{\epsilon}_a\, \xi_{mn} \sin\theta_{mn} I_{mn}^{TE} \right) e^{i[k_{xm}x + k_{yn}y - k_{zmn}(z-h/2)]} \\ &+ \sum_{m,n} \left(-\cos\theta_{mn} H_{mn}^{TM} + \sqrt{\epsilon}_a\, \xi_{mn} \sin\theta_{mn} E_{mn}^{TE} \right) e^{i[k_{xm}x + k_{yn}y + k_{zmn}(z-h/2)]}. \end{aligned} \tag{5.8f}$$

Similarly, we assume that the substrate (if non-metallic), defined by the region $z < h/2$ below the metal film, is filled with a dielectric ϵ_b. Thus,

$$\tilde{k}_{zmn} = \sqrt{\epsilon_b \kappa_0^2 - k_{xm}^2 - k_{yn}^2} \tag{5.9}$$

$$= \tilde{\xi}_{mn} \sqrt{\epsilon_b} \kappa_0, \tag{5.10}$$

where

$$\tilde{\xi}_{mn} \equiv \sqrt{1 - \frac{k_{xm}^2 + k_{yn}^2}{\epsilon_b \kappa_0^2}}. \tag{5.11}$$

Then the six electric and magnetic field components can be written,

$$\tilde{E}_z^{\text{sub}} = \sum_{m,n} \left(-\frac{1}{\sqrt{\epsilon_b}} \sqrt{1 - \tilde{\xi}_{mn}^2} \tilde{H}_{mn}^{TM} \right) e^{i[k_{xm}x + k_{yn}y - \tilde{k}_{zmn}(z+h/2)]}, \tag{5.12a}$$

$$\tilde{E}_x^{\text{sub}} = \sum_{m,n} \left(-\frac{1}{\sqrt{\epsilon_b}} \tilde{\xi}_{mn} \cos\theta_{mn} \tilde{H}_{mn}^{TM} + \sin\theta_{mn} \tilde{E}_{mn}^{TE} \right) e^{i[k_{xm}x + k_{yn}y - \tilde{k}_{zmn}(z+h/2)]}, \tag{5.12b}$$

$$\tilde{E}_y^{\text{sub}} = \sum_{m,n} \left(-\frac{1}{\sqrt{\epsilon_b}} \tilde{\xi}_{mn} \sin\theta_{mn} \tilde{H}_{mn}^{TM} - \cos\theta_{mn} \tilde{E}_{mn}^{TE} \right) e^{i[k_{xm}x + k_{yn}y - \tilde{k}_{zmn}(z+h/2)]}, \tag{5.12c}$$

$$\tilde{H}_z^{\text{sub}} = \sum_{m,n} \left(\sqrt{\epsilon_b} \sqrt{1 - \tilde{\xi}_{mn}^2} \tilde{E}_{mn}^{TE} \right) e^{i[k_{xm}x + k_{yn}y - \tilde{k}_{zmn}(z+h/2)]}, \tag{5.12d}$$

$$\tilde{H}_x^{\text{sub}} = \sum_{m,n} \left(\sin\theta_{mn} \tilde{H}_{mn}^{TM} - \sqrt{\epsilon_b}\, \tilde{\xi}_{mn} \cos\theta_{mn} \tilde{E}_{mn}^{TE} \right) e^{i[k_{xm}x + k_{yn}y - \tilde{k}_{zmn}(z+h/2)]}, \tag{5.12e}$$

$$\tilde{H}_y^{\text{sub}} = \sum_{m,n} \left(-\cos\theta_{mn} \tilde{H}_{mn}^{TM} - \sqrt{\epsilon_b}\, \tilde{\xi}_{mn} \sin\theta_{mn} \tilde{E}_{mn}^{TE} \right) e^{i[k_{xm}x + k_{yn}y - \tilde{k}_{zmn}(z+h/2)]}. \tag{5.12f}$$

Note that the substrate fields, expansion coefficients, and wave vectors are all noted by a tilde. Additionally, the substrate fields lack any incident (upward traveling) waves, as we assume light is only incident from the top surface.

5.3.2 Fields in the cavities or apertures

For the fields in the cavities or apertures, we expand as the sum of the TM and TE solutions to Eq. 2.8. For a single-surface cavity, there are no TEM modes. To distinguish between the propagation constants k_{zmn} and $\tilde{k}_{zmn}$ in the superstrate and substrate, we use γ as the propagation constant in the waveguide, and use indices s and l rather than m and n. Additionally, we will expand the fields generally in terms of the ψ_{sl}, without specifying if the cavity is rectangular or cylindrical; these results apply equally well to either case. We also assume the cavity is filled with a dielectric ϵ_c. Using the results of Section 2.2, and some vector calculus identities, the six electric and magnetic field components inside the cavity can we written,

$$E_z^{\text{cavity}} = \sum_{s,l} \psi_{sl}^{\text{TM}} \left[e^{i\gamma_{sl}(z+h/2)} \mathcal{A}_{sl} + e^{-i\gamma_{sl}(z+h/2)} \mathcal{B}_{sl} \right], \tag{5.13a}$$

$$\begin{aligned} E_x^{\text{cavity}} &= \sum_{s,l} \frac{i\gamma_{sl}}{\epsilon_c \kappa_0^2 - \gamma_{sl}^2} \hat{\mathbf{x}} \cdot \nabla_t \psi_{sl}^{\text{TM}} \left[e^{i\gamma_{sl}(z+h/2)} \mathcal{A}_{sl} - e^{-i\gamma_{sl}(z+h/2)} \mathcal{B}_{sl} \right] \\ &+ \sum_{s,l} \frac{i\kappa_0}{\epsilon_c \kappa_0^2 - \gamma_{sl}^2} \hat{\mathbf{y}} \cdot \nabla_t \psi_{sl}^{\text{TE}} \left[e^{i\gamma_{sl}(z+h/2)} \mathcal{D}_{sl} + e^{-i\gamma_{sl}(z+h/2)} \mathcal{F}_{sl} \right], \end{aligned} \tag{5.13b}$$

$$\begin{aligned} E_y^{\text{cavity}} &= \sum_{s,l} \frac{i\gamma_{sl}}{\epsilon_c \kappa_0^2 - \gamma_{sl}^2} \hat{\mathbf{y}} \cdot \nabla_t \psi_{sl}^{\text{TM}} \left[e^{i\gamma_{sl}(z+h/2)} \mathcal{A}_{sl} - e^{-i\gamma_{sl}(z+h/2)} \mathcal{B}_{sl} \right] \\ &+ \sum_{s,l} -\frac{i\kappa_0}{\epsilon_c \kappa_0^2 - \gamma_{sl}^2} \hat{\mathbf{x}} \cdot \nabla_t \psi_{sl}^{\text{TE}} \left[e^{i\gamma_{sl}(z+h/2)} \mathcal{D}_{sl} + e^{-i\gamma_{sl}(z+h/2)} \mathcal{F}_{sl} \right], \end{aligned} \tag{5.13c}$$

$$H_z^{\text{cavity}} = \sum_{s,l} \psi_{sl}^{\text{TE}} \left[e^{i\gamma_{sl}(z+h/2)} \mathcal{D}_{sl} + e^{-i\gamma_{sl}(z+h/2)} \mathcal{F}_{sl} \right], \tag{5.13d}$$

$$\begin{aligned} H_x^{\text{cavity}} &= \sum_{s,l} -\frac{i\epsilon_c\kappa_0}{\epsilon_c \kappa_0^2 - \gamma_{sl}^2} \hat{\mathbf{y}} \cdot \nabla_t \psi_{sl}^{\text{TM}} \left[e^{i\gamma_{sl}(z+h/2)} \mathcal{A}_{sl} + e^{-i\gamma_{sl}(z+h/2)} \mathcal{B}_{sl} \right] \\ &+ \sum_{s,l} \frac{i\gamma_{sl}}{\epsilon_c \kappa_0^2 - \gamma_{sl}^2} \hat{\mathbf{x}} \cdot \nabla_t \psi_{sl}^{\text{TE}} \left[e^{i\gamma_{sl}(z+h/2)} \mathcal{D}_{sl} - e^{-i\gamma_{sl}(z+h/2)} \mathcal{F}_{sl} \right], \end{aligned} \tag{5.13e}$$

$$H_y^{\mathrm{cavity}} = \sum_{s,l} \frac{i\epsilon_c\kappa_0}{\epsilon_c\kappa_0^2 - \gamma_{sl}^2}\,\hat{\mathbf{x}}\cdot\nabla_t\psi_{sl}^{\mathrm{TM}}\left[e^{i\gamma_{sl}(z+h/2)}\mathcal{A}_{sl} + e^{-i\gamma_{sl}(z+h/2)}\mathcal{B}_{sl}\right]$$
$$+\sum_{s,l} \frac{i\gamma_{sl}}{\epsilon_c\kappa_0^2 - \gamma_{sl}^2}\,\hat{\mathbf{y}}\cdot\nabla_t\psi_{sl}^{\mathrm{TE}}\left[e^{i\gamma_{sl}(z+h/2)}\mathcal{D}_{sl} - e^{-i\gamma_{sl}(z+h/2)}\mathcal{F}_{sl}\right], \quad (5.13\mathrm{f})$$

where we have expanded in terms of the upward and downward propagating TM mode expansion constants $\mathcal{A}_{sl}$ and $\mathcal{B}_{sl}$ and the upward and downward propagating TE mode expansion constants $\mathcal{D}_{sl}$ and $\mathcal{F}_{sl}$. For rectangular waveguide modes Eq. 2.10b, these expressions are simple; for cylindrical modes Eq. 2.10a these expressions are more complicated. In all cases, we assume solutions to these equations satisfying the SDBC at the cavity walls for determination of γ_{sl} and related constants.

5.4 Application of boundary conditions

We are now able to relate the fields in the superstrate, cavity or aperture, and substrate. We define the region $\mathbf{r}_t \in C$ as the cross-sectional face of the cavity or aperture and $\mathbf{r}_t \in P$ as the face of the entire period. Note that we have six sets of unknowns (H_{mn}^{TM}, E_{mn}^{TE}, $\mathcal{A}_{sl}$, $\mathcal{B}_{sl}$, $\mathcal{D}_{sl}$, and $\mathcal{F}_{sl}$) for cavities, and another two ($\tilde{H}_{mn}^{TM}$ and $\tilde{E}_{mn}^{TE}$) for an open aperture. We must therefore have six sets of equations relating these components (eight for apertures). The continuity of both of the transverse components of the electric and magnetic fields at the top interface gives us four sets. The remaining two (four) are found by application of the SDBC (continuity of both of transverse field components) at the bottom of the cavity (aperture).

5.4.1 The top boundary

Ensuring the continuity of the transverse electric field at the top interface, we equate Eqs. 5.8b and 5.13b evaluated at $z = h/2$, multiply by $\left(\psi_{qr}^{\mathrm{TM}}\right)^*$, integrate over the cavity face, and rearrange to give the unknowns in terms of the known quantities. This gives

$$\begin{aligned}
&\sum_{m,n} \mathcal{K}^{(1)}_{\left(\begin{smallmatrix} q & m \\ r & n \end{smallmatrix}\right)} \left(-\frac{1}{\sqrt{\epsilon_a}}\, \xi_{mn} \cos\theta_{mn} H^{TM}_{mn} - \sin\theta_{mn} E^{TE}_{mn} \right) \\
&\qquad + \sum_{s,l} \mathcal{G}^{(1)}_{\left(\begin{smallmatrix} q & s \\ r & l \end{smallmatrix}\right)} \frac{i\gamma_{sl}}{\epsilon_c \mathcal{K}_0^2 - \gamma_{sl}^2} \left[e^{i\gamma_{sl} h} \mathcal{A}_{sl} - e^{-i\gamma_{sl} h} \mathcal{B}_{sl} \right] \\
&\qquad + \sum_{s,l} \mathcal{G}^{(2)}_{\left(\begin{smallmatrix} q & s \\ r & l \end{smallmatrix}\right)} \frac{i\mathcal{K}_0}{\epsilon_c \mathcal{K}_0^2 - \gamma_{sl}^2} \left[e^{i\gamma_{sl} h} \mathcal{D}_{sl} + e^{-i\gamma_{sl} h} \mathcal{F}_{sl} \right] \\
&\qquad = \sum_{m,n} \mathcal{K}^{(1)}_{\left(\begin{smallmatrix} q & m \\ r & n \end{smallmatrix}\right)} \left(-\frac{1}{\sqrt{\epsilon_a}}\, \xi_{mn} \cos\theta_{mn} I^{TM}_{mn} + \sin\theta_{mn} I^{TE}_{mn} \right), \qquad (5.14)
\end{aligned}$$

where $\mathcal{K}$ and $\mathcal{G}$ represent the integrals,

$$\mathcal{K}^{(1)}_{\left(\begin{smallmatrix} q & m \\ r & n \end{smallmatrix}\right)} \equiv \iint_{\mathbf{r}_t \in C} e^{i[k_{xm}x + k_{yn}y]} \left(\psi_{qr}^{\mathrm{TM}}\right)^*, \qquad (5.15a)$$

$$\mathcal{K}^{(2)}_{\left(\begin{smallmatrix} q & m \\ r & n \end{smallmatrix}\right)} \equiv \iint_{\mathbf{r}_t \in C} e^{i[k_{xm}x + k_{yn}y]} \left(\psi_{qr}^{\mathrm{TE}}\right)^*, \qquad (5.15b)$$

$$(5.15c)$$

and

$$\mathcal{G}^{(1)}_{\left(\begin{smallmatrix} q & s \\ r & l \end{smallmatrix}\right)} \equiv \iint_{\mathbf{r}_t \in C} \left(\hat{\mathbf{x}} \cdot \nabla_t \psi^{\mathrm{TM}}_{sl}\right) \left(\psi^{\mathrm{TM}}_{qr}\right)^*, \tag{5.16a}$$

$$\mathcal{G}^{(2)}_{\left(\begin{smallmatrix} q & s \\ r & l \end{smallmatrix}\right)} \equiv \iint_{\mathbf{r}_t \in C} \left(\hat{\mathbf{y}} \cdot \nabla_t \psi^{\mathrm{TE}}_{sl}\right) \left(\psi^{\mathrm{TM}}_{qr}\right)^*, \tag{5.16b}$$

$$\mathcal{G}^{(3)}_{\left(\begin{smallmatrix} q & s \\ r & l \end{smallmatrix}\right)} \equiv \iint_{\mathbf{r}_t \in C} \left(\hat{\mathbf{y}} \cdot \nabla_t \psi^{\mathrm{TM}}_{sl}\right) \left(\psi^{\mathrm{TE}}_{qr}\right)^*, \tag{5.16c}$$

$$\mathcal{G}^{(4)}_{\left(\begin{smallmatrix} q & s \\ r & l \end{smallmatrix}\right)} \equiv \iint_{\mathbf{r}_t \in C} \left(\hat{\mathbf{x}} \cdot \nabla_t \psi^{\mathrm{TE}}_{sl}\right) \left(\psi^{\mathrm{TE}}_{qr}\right)^*. \tag{5.16d}$$

For rectangular geometries, these integrals have analytic solutions; for cylindrical geometries they must be computed numerically. For multiple cavities in a single unit cell, we repeat this analysis for each of cavities and its expansion coefficients.

We repeat this procedure for Eqs. 5.8c and 5.13c, now multiplying by $\left(\psi^{\mathrm{TE}}_{qr}\right)^*$. This gives,

$$\begin{aligned} \sum_{m,n} -\mathcal{K}^{(2)}_{\left(\begin{smallmatrix} q & m \\ r & n \end{smallmatrix}\right)} \left(\frac{1}{\sqrt{\epsilon_a}}\, \xi_{mn} \sin\theta_{mn} H^{TM}_{mn} - \cos\theta_{mn} E^{TE}_{mn}\right) & \\ + \sum_{s,l} \mathcal{G}^{(3)}_{\left(\begin{smallmatrix} q & s \\ r & l \end{smallmatrix}\right)} \frac{i\gamma_{sl}}{\epsilon_c \kappa_0^2 - \gamma_{sl}^2} \left[e^{i\gamma_{sl}h} \mathcal{A}_{sl} - e^{-i\gamma_{sl}h} \mathcal{B}_{sl}\right] & \\ + \sum_{s,l} -\mathcal{G}^{(4)}_{\left(\begin{smallmatrix} q & s \\ r & l \end{smallmatrix}\right)} \frac{i\kappa_0}{\epsilon_c \kappa_0^2 - \gamma_{sl}^2} \left[e^{i\gamma_{sl}h} \mathcal{D}_{sl} + e^{-i\gamma_{sl}h} \mathcal{F}_{sl}\right] & \\ = \sum_{m,n} \mathcal{K}^{(2)}_{\left(\begin{smallmatrix} q & m \\ r & n \end{smallmatrix}\right)} \left(-\frac{1}{\sqrt{\epsilon_a}}\, \xi_{mn} \sin\theta_{mn} I^{TM}_{mn} - \cos\theta_{mn} I^{TE}_{mn}\right). & \end{aligned} \tag{5.17}$$

We now equate the transverse magnetic field components. We do this in a piecewise fashion, equating Eqs. 5.8e and 5.13e over the cavity, and use the SIBC to relate $H_x = 1/\mathcal{Z}E_y$ over the metal, where E_y is given by Eq. 5.8c. These functions are evaluated at $z = h/2$, and we then multiply by $\exp\left[-i(k_{xg}x + k_{yf}y)\right]$, integrate over the entire period, and rearrange to give the unknowns in terms of the known quantities. This gives

$$\begin{aligned}
&\sum_{m,n} - \left(\delta^{(1)}_{\left(\begin{smallmatrix} g & m \\ f & n \end{smallmatrix}\right)} - \delta^{(2)}_{\left(\begin{smallmatrix} g & m \\ f & n \end{smallmatrix}\right)} \frac{1}{\mathcal{Z}} \frac{1}{\sqrt{\epsilon_a}}\, \xi_{mn}\right) \sin\theta_{mn} H^{TM}_{mn} \\
&\qquad \sum_{m,n} - \left(\delta^{(1)}_{\left(\begin{smallmatrix} g & m \\ f & n \end{smallmatrix}\right)} \sqrt{\epsilon_a}\, \xi_{mn} + \delta^{(2)}_{\left(\begin{smallmatrix} g & m \\ f & n \end{smallmatrix}\right)} \frac{1}{\mathcal{Z}}\right) \cos\theta_{mn} E^{TE}_{mn} \\
&\qquad + \sum_{s,l} -\mathcal{L}^{(1)}_{\left(\begin{smallmatrix} q & m \\ r & n \end{smallmatrix}\right)} \frac{i\epsilon_c \kappa_0}{\epsilon_c \kappa_0^2 - \gamma_{sl}^2} \left[e^{i\gamma_{sl}h} \mathcal{A}_{sl} + e^{-i\gamma_{sl}h} \mathcal{B}_{sl}\right] \\
&\qquad + \sum_{s,l} \mathcal{L}^{(2)}_{\left(\begin{smallmatrix} q & m \\ r & n \end{smallmatrix}\right)} \frac{i\gamma_{sl}}{\epsilon_c \kappa_0^2 - \gamma_{sl}^2} \left[e^{i\gamma_{sl}h} \mathcal{D}_{sl} - e^{-i\gamma_{sl}h} \mathcal{F}_{sl}\right] \\
&\qquad = \sum_{m,n} \left(\delta^{(1)}_{\left(\begin{smallmatrix} g & m \\ f & n \end{smallmatrix}\right)} + \delta^{(2)}_{\left(\begin{smallmatrix} g & m \\ f & n \end{smallmatrix}\right)} \frac{1}{\mathcal{Z}} \frac{1}{\sqrt{\epsilon_a}}\, \xi_{mn}\right) \sin\theta_{mn} I^{TM}_{mn} \\
&\qquad\qquad \sum_{m,n} - \left(\delta^{(1)}_{\left(\begin{smallmatrix} g & m \\ f & n \end{smallmatrix}\right)} \sqrt{\epsilon_a}\, \xi_{mn} - \delta^{(2)}_{\left(\begin{smallmatrix} g & m \\ f & n \end{smallmatrix}\right)} \frac{1}{\mathcal{Z}}\right) \cos\theta_{mn} I^{TE}_{mn},
\end{aligned} \tag{5.18}$$

where $\mathcal{L}$ and δ represent the integrals,

$$\mathcal{L}^{(1)}_{\left(\begin{smallmatrix} q & m \\ r & n \end{smallmatrix}\right)} \equiv \iint_{\mathbf{r}_t \in C} \left(\hat{\mathbf{y}} \cdot \nabla_t \psi^{\mathrm{TM}}_{sl}\right) e^{-i[k_{xg}x + k_{yf}y]}, \tag{5.19a}$$

$$\mathcal{L}^{(2)}_{\left(\begin{smallmatrix} q & m \\ r & n \end{smallmatrix}\right)} \equiv \iint_{\mathbf{r}_t \in C} \left(\hat{\mathbf{x}} \cdot \nabla_t \psi^{\mathrm{TE}}_{sl}\right) e^{-i[k_{xg}x + k_{yf}y]}, \tag{5.19b}$$

$$\mathcal{L}^{(3)}_{\left(\begin{smallmatrix} q & m \\ r & n \end{smallmatrix}\right)} \equiv \iint_{\mathbf{r}_t \in C} \left(\hat{\mathbf{x}} \cdot \nabla_t \psi^{\mathrm{TM}}_{sl}\right) e^{-i[k_{xg}x + k_{yf}y]}, \tag{5.19c}$$

$$\mathcal{L}^{(4)}_{\left(\begin{smallmatrix} q & m \\ r & n \end{smallmatrix}\right)} \equiv \iint_{\mathbf{r}_t \in C} \left(\hat{\mathbf{y}} \cdot \nabla_t \psi^{\mathrm{TE}}_{sl}\right) e^{-i[k_{xg}x + k_{yf}y]}, \tag{5.19d}$$

and

$$\delta^{(1)}_{\left(\begin{smallmatrix} g & m \\ f & n \end{smallmatrix}\right)} \equiv \Lambda_x \Lambda_y \delta_{mg} \delta_{nf}, \tag{5.20a}$$

$$\delta^{(2)}_{\left(\begin{smallmatrix} g & m \\ f & n \end{smallmatrix}\right)} \equiv \iint_{\mathbf{r}_t \notin C} e^{i[k_{xm}x + k_{yn}y]} e^{-i[k_{xg}x + k_{yf}y]}, \tag{5.20b}$$

$$\tag{5.20c}$$

where δ_{mn} is the Kronecker delta function. Here as well, for rectangular geometries these integrals have analytic solutions; for cylindrical geometries they must be computed numerically. For multiple cavities in a single unit cell, the integral $\delta^{(2)}$ over the region $\mathbf{r}_t \notin C$ is transformed to the region not containing any cavity, and the integrals $\mathcal{L}$ over the cavity must be computed over each cavity face.

Finally, we repeat this procedure for the y-component of the magnetic field, equating Eqs. 5.8f and 5.13f over the cavity, and using $H_y = -1/\mathcal{Z} E_x$

over the metal, where E_x is given by Eq. 5.8c. This gives,

$$\begin{aligned}
\sum_{m,n} \left(\delta^{(1)}_{\left(\begin{smallmatrix} g & m \\ f & n \end{smallmatrix}\right)} - \delta^{(2)}_{\left(\begin{smallmatrix} g & m \\ f & n \end{smallmatrix}\right)} \frac{1}{\mathcal{Z}} \frac{1}{\sqrt{\epsilon_a}}\, \xi_{mn} \right) \cos\theta_{mn} H^{TM}_{mn} & \\
+ \sum_{m,n} - \left(\delta^{(1)}_{\left(\begin{smallmatrix} g & m \\ f & n \end{smallmatrix}\right)} \sqrt{\epsilon_a}\, \xi_{mn} + \delta^{(2)}_{\left(\begin{smallmatrix} g & m \\ f & n \end{smallmatrix}\right)} \frac{1}{\mathcal{Z}} \right) \sin\theta_{mn} E^{TE}_{mn} & \\
+ \sum_{s,l} \mathcal{L}^{(3)}_{\left(\begin{smallmatrix} q & m \\ r & n \end{smallmatrix}\right)} \frac{i\epsilon_c \varkappa_0}{\epsilon_c \varkappa_0^2 - \gamma_{sl}^2} \left[e^{i\gamma_{sl}h} \mathcal{A}_{sl} + e^{-i\gamma_{sl}h} \mathcal{B}_{sl} \right] & \\
+ \sum_{s,l} \mathcal{L}^{(4)}_{\left(\begin{smallmatrix} q & m \\ r & n \end{smallmatrix}\right)} \frac{i\gamma_{sl}}{\epsilon_c \varkappa_0^2 - \gamma_{sl}^2} \left[e^{i\gamma_{sl}h} \mathcal{D}_{sl} - e^{-i\gamma_{sl}h} \mathcal{F}_{sl} \right] & \\
= \sum_{m,n} - \left(\delta^{(1)}_{\left(\begin{smallmatrix} g & m \\ f & n \end{smallmatrix}\right)} + \delta^{(2)}_{\left(\begin{smallmatrix} g & m \\ f & n \end{smallmatrix}\right)} \frac{1}{\mathcal{Z}} \frac{1}{\sqrt{\epsilon_a}}\, \xi_{mn} \right) \cos\theta_{mn} I^{TM}_{mn} & \\
\sum_{m,n} - \left(\delta^{(1)}_{\left(\begin{smallmatrix} g & m \\ f & n \end{smallmatrix}\right)} \sqrt{\epsilon_a}\, \xi_{mn} - \delta^{(2)}_{\left(\begin{smallmatrix} g & m \\ f & n \end{smallmatrix}\right)} \frac{1}{\mathcal{Z}} \right) \sin\theta_{mn} I^{TE}_{mn}. & \quad (5.21)
\end{aligned}$$

5.4.2 The bottom boundary

At the bottom boundary we have two choices of boundary conditions, depending on the situation. If the cavities are closed, i.e. there is metal at the bottom, we apply the SDBC. When the apertures are open to the substrate, we repeat the procedure of field continuity from the top surface.

Cavities

As discussed at length in Chapter 3, the SDBC assumes that once the fields have reached a skin depth into the metal, they resemble PEC fields. Due to the relationships between the transverse fields and the normal fields within a cavity (Eqs. 2.7), it is sufficient to ensure that the normal fields drop to zero upon reaching a skin depth. Applying this condition to Eq. 5.13a evaluated at $z = -h/2$, multiplying by $\left(\psi_{qr}^{\mathrm{TM}}\right)^*$, integrating over the area of the cavity gives:

$$\mathcal{A}_{sl} + \mathcal{B}_{sl} = 0, \tag{5.22}$$

due to the orthogonality of the waveguide modes. Similarly, applying this condition to Eq. 5.13d evaluated at $z = -h/2$, multiplying by $\left(\psi_{qr}^{\mathrm{TE}}\right)^*$, integrating over the area of the cavity gives:

$$\mathcal{D}_{sl} + \mathcal{F}_{sl} = 0, \tag{5.23}$$

These are the remaining two sets of equations required to solve the system.

Apertures

For open apertures, we again match all four transverse electric and magnetic field components. Ensuring the continuity of the transverse electric field at the bottom interface, we equate Eqs. 5.12b and 5.13b evaluated at $z = -h/2$, multiply by $\left(\psi_{qr}^{\mathrm{TM}}\right)^*$, integrate over the cavity face, and rearrange to give the unknowns in terms of the known quantities. This gives,

$$\sum_{s,l} \mathcal{G}^{(1)}_{\left(\begin{smallmatrix} q & s \\ r & l \end{smallmatrix}\right)} \frac{i\gamma_{sl}}{\epsilon_c \kappa_0^2 - \gamma_{sl}^2} \left[\mathcal{A}_{sl} - \mathcal{B}_{sl}\right] + \sum_{s,l} \mathcal{G}^{(2)}_{\left(\begin{smallmatrix} q & s \\ r & l \end{smallmatrix}\right)} \frac{i\kappa_0}{\epsilon_c \kappa_0^2 - \gamma_{sl}^2} \left[\mathcal{D}_{sl} + \mathcal{F}_{sl}\right] \\ + \sum_{m,n} \mathcal{K}^{(1)}_{\left(\begin{smallmatrix} q & m \\ r & n \end{smallmatrix}\right)} \left(\frac{1}{\sqrt{\epsilon_b}} \tilde{\xi}_{mn} \cos\theta_{mn} \tilde{H}^{TM}_{mn} - \sin\theta_{mn} \tilde{E}^{TE}_{mn} \right) = 0. \tag{5.24}$$

We repeat this procedure for Eqs. 5.12c and 5.13c, now multiplying by $\left(\psi_{qr}^{\mathrm{TE}}\right)^*$. This gives,

$$\sum_{s,l} \mathcal{G}^{(3)}_{\left(\begin{smallmatrix} q & s \\ r & l \end{smallmatrix}\right)} \frac{i\gamma_{sl}}{\epsilon_c \kappa_0^2 - \gamma_{sl}^2} \left[\mathcal{A}_{sl} - \mathcal{B}_{sl}\right] + \sum_{s,l} -\mathcal{G}^{(4)}_{\left(\begin{smallmatrix} q & s \\ r & l \end{smallmatrix}\right)} \frac{i\kappa_0}{\epsilon_c \kappa_0^2 - \gamma_{sl}^2} \left[\mathcal{D}_{sl} + \mathcal{F}_{sl}\right]$$
$$+ \sum_{m,n} \mathcal{K}^{(2)}_{\left(\begin{smallmatrix} q & m \\ r & n \end{smallmatrix}\right)} \left(\frac{1}{\sqrt{\epsilon_b}} \tilde{\xi}_{mn} \sin\theta_{mn} \tilde{H}_{mn}^{TM} + \cos\theta_{mn} \tilde{E}_{mn}^{TE} \right) = 0. \quad (5.25)$$

Here, again, for multiple cavities in a single unit cell, we repeat this analysis for each of cavities and its expansion coefficients.

We now equate the transverse magnetic field components. Here again we use the piecewise approach, equating Eqs. 5.12e and 5.13e over the aperture, and $H_x = -1/\mathcal{Z} E_y$ over the metal, where E_y is given by Eq. 5.12f. Note that here, $\hat{\mathbf{n}} = -\hat{\mathbf{z}}$ in the SIBC. These functions are evaluated at $z = -h/2$, and we then multiply by $\exp\left[-i(k_{xg}x + k_{yf}y)\right]$, integrate over the entire period, and rearrange to give the unknowns in terms of the known quantities. This gives

$$\sum_{s,l} -\mathcal{L}^{(1)}_{\left(\begin{smallmatrix} q & m \\ r & n \end{smallmatrix}\right)} \frac{i\epsilon_c \kappa_0}{\epsilon_c \kappa_0^2 - \gamma_{sl}^2} \left[\mathcal{A}_{sl} + \mathcal{B}_{sl}\right] + \sum_{s,l} \mathcal{L}^{(2)}_{\left(\begin{smallmatrix} q & m \\ r & n \end{smallmatrix}\right)} \frac{i\gamma_{sl}}{\epsilon_c \kappa_0^2 - \gamma_{sl}^2} \left[\mathcal{D}_{sl} - \mathcal{F}_{sl}\right]$$
$$+ \sum_{m,n} - \left(\delta^{(1)}_{\left(\begin{smallmatrix} g & m \\ f & n \end{smallmatrix}\right)} - \delta^{(2)}_{\left(\begin{smallmatrix} g & m \\ f & n \end{smallmatrix}\right)} \frac{1}{\mathcal{Z}} \frac{1}{\sqrt{\epsilon_b}} \tilde{\xi}_{mn} \right) \sin\theta_{mn} \tilde{H}_{mn}^{TM}$$
$$+ \sum_{m,n} \left(\delta^{(1)}_{\left(\begin{smallmatrix} g & m \\ f & n \end{smallmatrix}\right)} \sqrt{\epsilon_b}\, \tilde{\xi}_{mn} + \delta^{(2)}_{\left(\begin{smallmatrix} g & m \\ f & n \end{smallmatrix}\right)} \frac{1}{\mathcal{Z}} \right) \cos\theta_{mn} \tilde{E}_{mn}^{TE} = 0. \quad (5.26)$$

Finally, we repeat this procedure for the y-component of the magnetic field, equating Eqs. 5.12f and 5.13f over the aperture, and using $H_y = 1/\mathcal{Z} E_x$ over the metal, where E_y is given by Eq. 5.12c. This gives,

$$\begin{aligned}\sum_{s,l}\mathcal{L}^{(3)}_{\left(\begin{smallmatrix} q & m \\ r & n\end{smallmatrix}\right)}\frac{i\epsilon_c\kappa_0}{\epsilon_c\kappa_0^2-\gamma_{sl}^2}\left[\mathcal{A}_{sl}+\mathcal{B}_{sl}\right]+\sum_{s,l}\mathcal{L}^{(4)}_{\left(\begin{smallmatrix} q & m \\ r & n\end{smallmatrix}\right)}\frac{i\gamma_{sl}}{\epsilon_c\kappa_0^2-\gamma_{sl}^2}\left[\mathcal{D}_{sl}-\mathcal{F}_{sl}\right]\\ +\sum_{m,n}\left(\delta^{(1)}_{\left(\begin{smallmatrix} g & m \\ f & n\end{smallmatrix}\right)}-\delta^{(2)}_{\left(\begin{smallmatrix} g & m \\ f & n\end{smallmatrix}\right)}\frac{1}{\mathcal{Z}}\frac{1}{\sqrt{\epsilon_b}}\,\tilde{\xi}_{mn}\right)\cos\theta_{mn}\tilde{H}^{TM}_{mn}\\ +\sum_{m,n}\left(\delta^{(1)}_{\left(\begin{smallmatrix} g & m \\ f & n\end{smallmatrix}\right)}\sqrt{\epsilon_b}\,\tilde{\xi}_{mn}+\delta^{(2)}_{\left(\begin{smallmatrix} g & m \\ f & n\end{smallmatrix}\right)}\frac{1}{\mathcal{Z}}\right)\sin\theta_{mn}\tilde{E}^{TE}_{mn}=0.\end{aligned}\tag{5.27}$$

These are the remaining sets of equations required to solve the system.

5.5 Constructing a coupling matrix

At this point, we would like to construct a coupling matrix to relate the unknown quantities with the known. We are looking for a matrix-vector equation of the form:

$$\mathcal{M}\mathbf{\Psi}=\mathbf{\Theta}\tag{5.28}$$

However, looking at all the coupling equations, we see that our known (and unknown) quantities are rank 2 tensors (matrices). In order to get an equation like Eq. 5.28, we change indices.

For the Floquet mode, both m and n run from $-N$ to N, for a total of $(2N+1)^2$ modes. Note, that N can be different values for the superstrate (N_a) and substrate (N_b). We choose a new index $\tilde{m}$ which runs from 1 to $(2N+1)^2$, cycling over each n for every m, see Table 5.1(a). Thus, $\tilde{m}$ goes

$\tilde{m}$	m	n
1	$-N$	$-N$
2	$-N$	$-N+1$
$\vdots$	$\vdots$	$\vdots$
$2N+1$	$-N$	N
$(2N+1)+1$	$-N+1$	$-N$
$\vdots$	$\vdots$	$\vdots$
$(2N+1)^2$	N	N

(a) Change of index re-mapping for m and n.

$\tilde{s}$	s	l
1	1	1
2	1	2
$\vdots$	$\vdots$	$\vdots$
S	1	S
$S+1$	2	1
$\vdots$	$\vdots$	$\vdots$
S^2	S	S

(b) Change of index re-mapping for s and l.

Table 5.1: Change of summation index re-mapping to convert double sums to a matrix-vector equation.

from 1 to $(2N+1)^2$. We similarly define $\tilde{g}$ for the indices g and h which run from $-G$ to G.

For the cavity modes, both s and l run from 1 to S, for a total of S^2 modes. We choose a new index $\tilde{s}$ which runs from 1 to S^2, cycling over ever l for each s, see Table 5.1(b). We similarly define $\tilde{q}$ for the indices q and r which run from 1 to Q^2.

Then, unknown quantities like $\mathcal{A}_{sl}$ become vectors and other single-index quantities, like ξ_{mn}, become diagonal matrices. Similarly, expressions like $\mathcal{F}_{\left(\begin{smallmatrix} q & m \\ r & n \end{smallmatrix}\right)}$ become matrices $\mathcal{F}_{(\tilde{q}\tilde{m})} = \mathcal{F}_{\tilde{q}\tilde{m}}$. Now, we can drop all the explicit summation signs over $\tilde{m}$ and $\tilde{s}$ (Einstein notation), and re-write Eqs. 5.14, 5.17, 5.18, and 5.21 as,

$$\begin{aligned}
&-\mathcal{K}^{(1)}_{\tilde q\tilde m}\frac{1}{\sqrt{\epsilon_a}}\,\xi_{\tilde m}\cos\theta_{\tilde m}\mathbf{H}^{TM}_{\tilde m}-\mathcal{K}^{(1)}_{\tilde q\tilde m}\sin\theta_{\tilde m}\mathbf{E}^{TE}_{\tilde m}\\
&\qquad+\mathcal{G}^{(1)}_{\tilde q\tilde s}\frac{i\gamma_{\tilde s}}{\epsilon_c\kappa_0^2-\gamma_{\tilde s}^2}e^{i\gamma_{\tilde s}h}\mathbf{A}_{\tilde s}-\mathcal{G}^{(1)}_{\tilde q\tilde s}\frac{i\gamma_{\tilde s}}{\epsilon_c\kappa_0^2-\gamma_{\tilde s}^2}e^{-i\gamma_{\tilde s}h}\mathbf{B}_{\tilde s}\\
&\qquad+\mathcal{G}^{(2)}_{\tilde q\tilde s}\frac{i\kappa_0}{\epsilon_c\kappa_0^2-\gamma_{\tilde s}^2}e^{i\gamma_{\tilde s}h}\mathbf{D}_{\tilde s}+\mathcal{G}^{(2)}_{\tilde q\tilde s}\frac{i\kappa_0}{\epsilon_c\kappa_0^2-\gamma_{\tilde s}^2}e^{-i\gamma_{\tilde s}h}\mathbf{F}_{\tilde s}\\
&\qquad\qquad=-\mathcal{K}^{(1)}_{\tilde q\tilde m}\frac{1}{\sqrt{\epsilon_a}}\,\xi_{\tilde m}\cos\theta_{\tilde m}\mathbf{I}^{TM}_{\tilde m}+\mathcal{K}^{(1)}_{\tilde q\tilde m}\sin\theta_{\tilde m}\mathbf{I}^{TE}_{\tilde m},
\end{aligned}\tag{5.29a}$$

$$\begin{aligned}
&-\mathcal{K}^{(2)}_{\tilde q\tilde m}\frac{1}{\sqrt{\epsilon_a}}\,\xi_{\tilde m}\sin\theta_{\tilde m}\mathbf{H}^{TM}_{\tilde m}+\mathcal{K}^{(2)}_{\tilde q\tilde m}\cos\theta_{\tilde m}\mathbf{E}^{TE}_{\tilde m}\\
&\qquad+\mathcal{G}^{(3)}_{\tilde q\tilde s}\frac{i\gamma_{\tilde s}}{\epsilon_c\kappa_0^2-\gamma_{\tilde s}^2}e^{i\gamma_{\tilde s}h}\mathbf{A}_{\tilde s}-\mathcal{G}^{(3)}_{\tilde q\tilde s}\frac{i\gamma_{\tilde s}}{\epsilon_c\kappa_0^2-\gamma_{\tilde s}^2}e^{-i\gamma_{\tilde s}h}\mathbf{B}_{\tilde s}\\
&\qquad-\mathcal{G}^{(4)}_{\tilde q\tilde s}\frac{i\kappa_0}{\epsilon_c\kappa_0^2-\gamma_{\tilde s}^2}e^{i\gamma_{\tilde s}h}\mathbf{D}_{\tilde s}-\mathcal{G}^{(4)}_{\tilde q\tilde s}\frac{i\kappa_0}{\epsilon_c\kappa_0^2-\gamma_{\tilde s}^2}e^{-i\gamma_{\tilde s}h}\mathbf{F}_{\tilde s}\\
&\qquad\qquad=-\mathcal{K}^{(2)}_{\tilde q\tilde m}\frac{1}{\sqrt{\epsilon_a}}\,\xi_{\tilde m}\sin\theta_{\tilde m}\mathbf{I}^{TM}_{\tilde m}-\mathcal{K}^{(2)}_{\tilde q\tilde m}\cos\theta_{\tilde m}\mathbf{I}^{TE}_{\tilde m},
\end{aligned}\tag{5.29b}$$

$$\begin{aligned}
&-\left(\delta^{(1)}_{\tilde g\tilde m}-\delta^{(2)}_{\tilde g\tilde m}\frac{1}{\mathcal{Z}}\frac{1}{\sqrt{\epsilon_a}}\,\xi_{\tilde m}\right)\sin\theta_{\tilde m}\mathbf{H}^{TM}_{\tilde m}-\left(\delta^{(2)}_{\tilde g\tilde m}\frac{1}{\mathcal{Z}}+\delta^{(1)}_{\tilde g\tilde m}\sqrt{\epsilon_a}\,\xi_{\tilde m}\right)\cos\theta_{\tilde m}\mathbf{E}^{TE}_{\tilde m}\\
&\qquad-\mathcal{L}^{(1)}_{\tilde q\tilde m}\frac{i\epsilon_c\kappa_0}{\epsilon_c\kappa_0^2-\gamma_{\tilde s}^2}e^{i\gamma_{\tilde s}h}\mathbf{A}_{\tilde s}-\mathcal{L}^{(1)}_{\tilde q\tilde m}\frac{i\epsilon_c\kappa_0}{\epsilon_c\kappa_0^2-\gamma_{\tilde s}^2}e^{-i\gamma_{\tilde s}h}\mathbf{B}_{\tilde s}\\
&\qquad+\mathcal{L}^{(2)}_{\tilde q\tilde m}\frac{i\gamma_{\tilde s}}{\epsilon_c\kappa_0^2-\gamma_{\tilde s}^2}e^{i\gamma_{\tilde s}h}\mathbf{D}_{\tilde s}-\mathcal{L}^{(2)}_{\tilde q\tilde m}\frac{i\gamma_{\tilde s}}{\epsilon_c\kappa_0^2-\gamma_{\tilde s}^2}e^{-i\gamma_{\tilde s}h}\mathbf{F}_{\tilde s}\\
&=\left(\delta^{(1)}_{\tilde g\tilde m}+\delta^{(2)}_{\tilde g\tilde m}\frac{1}{\mathcal{Z}}\frac{1}{\sqrt{\epsilon_a}}\,\xi_{\tilde m}\right)\sin\theta_{\tilde m}\mathbf{I}^{TM}_{\tilde m}-\left(\delta^{(1)}_{\tilde g\tilde m}\sqrt{\epsilon_a}\,\xi_{\tilde m}-\delta^{(2)}_{\tilde g\tilde m}\frac{1}{\mathcal{Z}}\right)\cos\theta_{\tilde m}\mathbf{I}^{TE}_{\tilde m},
\end{aligned}\tag{5.29c}$$

and

$$\begin{aligned}
&\left(\delta^{(1)}_{\tilde{g}\tilde{m}} - \delta^{(2)}_{\tilde{g}\tilde{m}}\frac{1}{\mathcal{Z}}\frac{1}{\sqrt{\epsilon_a}}\,\xi_{\tilde{m}}\right)\cos\theta_{\tilde{m}}\mathbf{H}^{TM}_{\tilde{m}} - \left(\delta^{(1)}_{\tilde{g}\tilde{m}}\sqrt{\epsilon_a}\,\xi_{\tilde{m}} + \delta^{(2)}_{\tilde{g}\tilde{m}}\frac{1}{\mathcal{Z}}\right)\sin\theta_{\tilde{m}}\mathbf{E}^{TE}_{\tilde{m}} \\
&\qquad + \mathcal{L}^{(3)}_{\tilde{q}\tilde{m}}\frac{i\epsilon_c\kappa_0}{\epsilon_c\kappa_0^2-\gamma_{\tilde{s}}^2}e^{i\gamma_{\tilde{s}}h}\mathbf{A}_{\tilde{s}} + \mathcal{L}^{(3)}_{\tilde{q}\tilde{m}}\frac{i\epsilon_c\kappa_0}{\epsilon_c\kappa_0^2-\gamma_{\tilde{s}}^2}e^{-i\gamma_{\tilde{s}}h}\mathbf{B}_{\tilde{s}} \\
&\qquad + \mathcal{L}^{(4)}_{\tilde{q}\tilde{m}}\frac{i\gamma_{\tilde{s}}}{\epsilon_c\kappa_0^2-\gamma_{\tilde{s}}^2}e^{i\gamma_{\tilde{s}}h}\mathbf{D}_{\tilde{s}} - \mathcal{L}^{(4)}_{\tilde{q}\tilde{m}}\frac{i\gamma_{\tilde{s}}}{\epsilon_c\kappa_0^2-\gamma_{\tilde{s}}^2}e^{-i\gamma_{\tilde{s}}h}\mathbf{F}_{\tilde{s}} \\
&= -\left(\delta^{(1)}_{\tilde{g}\tilde{m}} + \delta^{(2)}_{\tilde{g}\tilde{m}}\frac{1}{\mathcal{Z}}\frac{1}{\sqrt{\epsilon_a}}\,\xi_{\tilde{m}}\right)\cos\theta_{\tilde{m}}\mathbf{I}^{TM}_{\tilde{m}} - \left(\delta^{(1)}_{\tilde{g}\tilde{m}}\sqrt{\epsilon_a}\,\xi_{\tilde{m}} - \delta^{(2)}_{\tilde{g}\tilde{m}}\frac{1}{\mathcal{Z}}\right)\sin\theta_{\tilde{m}}\mathbf{I}^{TE}_{\tilde{m}}.
\end{aligned} \tag{5.29d}$$

Similarly, we rewrite Eqs. 5.22 and 5.23 as,

$$\mathbf{A}_{\tilde{s}} + \mathbf{B}_{\tilde{s}} = 0, \tag{5.30a}$$

and

$$\mathbf{D}_{\tilde{s}} + \mathbf{F}_{\tilde{s}} = 0, \tag{5.30b}$$

or Eqs. 5.24, 5.25, 5.26, and 5.27 as

$$\begin{aligned}
&\mathcal{G}^{(1)}_{\tilde{q}\tilde{s}}\frac{i\gamma_{\tilde{s}}}{\epsilon_c\kappa_0^2-\gamma_{\tilde{s}}^2}\mathbf{A}_{\tilde{s}} - \mathcal{G}^{(1)}_{\tilde{q}\tilde{s}}\frac{i\gamma_{\tilde{s}}}{\epsilon_c\kappa_0^2-\gamma_{\tilde{s}}^2}\mathbf{B}_{\tilde{s}} + \mathcal{G}^{(2)}_{\tilde{q}\tilde{s}}\frac{i\kappa_0}{\epsilon_c\kappa_0^2-\gamma_{\tilde{s}}^2}\mathbf{D}_{\tilde{s}} + \mathcal{G}^{(2)}_{\tilde{q}\tilde{s}}\frac{i\kappa_0}{\epsilon_c\kappa_0^2-\gamma_{\tilde{s}}^2}\mathbf{F}_{\tilde{s}} \\
&\qquad + \mathcal{K}^{(1)}_{\tilde{q}\tilde{m}}\frac{1}{\sqrt{\epsilon_b}}\,\tilde{\xi}_{\tilde{m}}\cos\theta_{\tilde{m}}\tilde{\mathbf{H}}^{TM}_{\tilde{m}} - \mathcal{K}^{(1)}_{\tilde{q}\tilde{m}}\sin\theta_{\tilde{m}}\tilde{\mathbf{E}}^{TE}_{\tilde{m}} \\
&= 0,
\end{aligned} \tag{5.31a}$$

$$\begin{aligned}
&\mathcal{G}^{(3)}_{\tilde{q}\tilde{s}}\frac{i\gamma_{\tilde{s}}}{\epsilon_c\kappa_0^2-\gamma_{\tilde{s}}^2}\mathbf{A}_{\tilde{s}} - \mathcal{G}^{(3)}_{\tilde{q}\tilde{s}}\frac{i\gamma_{\tilde{s}}}{\epsilon_c\kappa_0^2-\gamma_{\tilde{s}}^2}\mathbf{B}_{\tilde{s}} - \mathcal{G}^{(4)}_{\tilde{q}\tilde{s}}\frac{i\kappa_0}{\epsilon_c\kappa_0^2-\gamma_{\tilde{s}}^2}\mathbf{D}_{\tilde{s}} - \mathcal{G}^{(4)}_{\tilde{q}\tilde{s}}\frac{i\kappa_0}{\epsilon_c\kappa_0^2-\gamma_{\tilde{s}}^2}\mathbf{F}_{\tilde{s}} \\
&\qquad + \mathcal{K}^{(2)}_{\tilde{q}\tilde{m}}\frac{1}{\sqrt{\epsilon_b}}\,\tilde{\xi}_{\tilde{m}}\sin\theta_{\tilde{m}}\tilde{\mathbf{H}}^{TM}_{\tilde{m}} + \mathcal{K}^{(2)}_{\tilde{q}\tilde{m}}\cos\theta_{\tilde{m}}\tilde{\mathbf{E}}^{TE}_{\tilde{m}} \\
&= 0,
\end{aligned} \tag{5.31b}$$

$$-\mathcal{L}^{(1)}_{\tilde{q}\tilde{m}}\frac{i\epsilon_c\varkappa_0}{\epsilon_c\varkappa_0^2-\gamma_{\tilde{s}}^2}\mathbf{A}_{\tilde{s}}-\mathcal{L}^{(1)}_{\tilde{q}\tilde{m}}\frac{i\epsilon_c\varkappa_0}{\epsilon_c\varkappa_0^2-\gamma_{\tilde{s}}^2}\mathbf{B}_{\tilde{s}}+\mathcal{L}^{(2)}_{\tilde{q}\tilde{m}}\frac{i\gamma_{\tilde{s}}}{\epsilon_c\varkappa_0^2-\gamma_{\tilde{s}}^2}\mathbf{D}_{\tilde{s}}-\mathcal{L}^{(2)}_{\tilde{q}\tilde{m}}\frac{i\gamma_{\tilde{s}}}{\epsilon_c\varkappa_0^2-\gamma_{\tilde{s}}^2}\mathbf{F}_{\tilde{s}}$$
$$-\left(\delta^{(1)}_{\tilde{g}\tilde{m}}-\delta^{(2)}_{\tilde{g}\tilde{m}}\frac{1}{\mathcal{Z}}\frac{1}{\sqrt{\epsilon_b}}\,\tilde{\xi}_{\tilde{m}}\right)\sin\theta_{\tilde{m}}\tilde{\mathbf{H}}^{TM}_{\tilde{m}}+\left(\delta^{(1)}_{\tilde{g}\tilde{m}}\sqrt{\epsilon_b}\,\tilde{\xi}_{\tilde{m}}+\delta^{(2)}_{\tilde{g}\tilde{m}}\frac{1}{\mathcal{Z}}\right)\cos\theta_{\tilde{m}}\tilde{\mathbf{E}}^{TE}_{\tilde{m}}$$
$$=0, \quad (5.31c)$$

and

$$\mathcal{L}^{(3)}_{\tilde{q}\tilde{m}}\frac{i\epsilon_c\varkappa_0}{\epsilon_c\varkappa_0^2-\gamma_{\tilde{s}}^2}\mathbf{A}_{\tilde{s}}+\mathcal{L}^{(3)}_{\tilde{q}\tilde{m}}\frac{i\epsilon_c\varkappa_0}{\epsilon_c\varkappa_0^2-\gamma_{\tilde{s}}^2}\mathbf{B}_{\tilde{s}}+\mathcal{L}^{(4)}_{\tilde{q}\tilde{m}}\frac{i\gamma_{\tilde{s}}}{\epsilon_c\varkappa_0^2-\gamma_{\tilde{s}}^2}\mathbf{D}_{\tilde{s}}-\mathcal{L}^{(4)}_{\tilde{q}\tilde{m}}\frac{i\gamma_{\tilde{s}}}{\epsilon_c\varkappa_0^2-\gamma_{\tilde{s}}^2}\mathbf{F}_{\tilde{s}}$$
$$+\left(\delta^{(1)}_{\tilde{g}\tilde{m}}-\delta^{(2)}_{\tilde{g}\tilde{m}}\frac{1}{\mathcal{Z}}\frac{1}{\sqrt{\epsilon_b}}\,\tilde{\xi}_{\tilde{m}}\right)\cos\theta_{\tilde{m}}\tilde{\mathbf{H}}^{TM}_{\tilde{m}}+\left(\delta^{(1)}_{\tilde{g}\tilde{m}}\sqrt{\epsilon_b}\,\tilde{\xi}_{\tilde{m}}+\delta^{(2)}_{\tilde{g}\tilde{m}}\frac{1}{\mathcal{Z}}\right)\sin\theta_{\tilde{m}}\tilde{\mathbf{E}}^{TE}_{\tilde{m}}$$
$$=0. \quad (5.31d)$$

These equations make up a block matrix formulation, with

$$\mathbf{\Psi}=\begin{pmatrix}\mathbf{H}^{TM}_{\tilde{m}} & \mathbf{E}^{TE}_{\tilde{m}} & \mathbf{A}_{\tilde{s}} & \mathbf{B}_{\tilde{s}} & \mathbf{D}_{\tilde{s}} & \mathbf{F}_{\tilde{s}} & \tilde{\mathbf{H}}^{TM}_{\tilde{m}} & \tilde{\mathbf{E}}^{TE}_{\tilde{m}}\end{pmatrix}^T, \qquad (5.32)$$

and the corresponding entries in $\mathbf{\Theta}$ and $\mathcal{M}$ being filled by the matrices in these equations. Note, the last two entries in this vector are not included for closed cavities. Then, to find the unknown field components $\mathbf{\Psi}$ are found by solving the matrix equation. Note, that for multiple cavities, the central cavity expansion coefficient list is expanded to include the additional unknowns.

5.6 Conclusions and outlook

In this chapter we have detailed a powerful technique for modeling two-dimensional periodic metamaterials. This method has significant advantages over finite element or finite difference time domain *simulations*. This method makes use of accurate, fast, and versatile *calculations*, with the majority of the calculation overhead taken care of. Here, accuracy is limited by only by the precision of computer algorithms, and runs extremely fast, even on standard computer workstations. Similar simulations take significantly longer (on the order of hours) to solve, especially as the number of cavities per unit cell increases.

From a computational point of view, a parameter variation sweep (i.e. changing cavity dimensions, dielectrics) is an embarrassingly parallel problem, and we have written a simple distributed solve tool for this algorithm. Parameter sweeps that take upwards of a week in a finite element solver can be completed in a manner of hours using our tool. Various matrix equation algorithms (i.e. LU decomposition, block matrix algorithms etc.) can be used to further speed up these parametric sweeps.[74]

This approach can also be generalized to allow a combination of open and closed cavities in a single unit cell. This would require extra care to be taken with the various heights h appearing throughout the expressions in this chapter. Furthermore, although the structures discussed here are a fairly simple cavity structures, with known waveguide solutions, this approach may be generalizable to more complicated cavity shapes through appropriate coordinate transformations or choice of basis functions.[75]

It may also be possible, using block matrix analysis, to write an analytic expression for the matrix inverse $\mathcal{M}^{-1}$. This may be a path towards a complete analytic field analysis, without relying on numerical calculations or various other approximations.

Chapter 6

Simulation methods

6.1 Introduction

In this chapter we discuss our methods of finite element simulations, including approaches useful for increasing efficiency and optimizing structures. All of the methods developed thus far in this thesis can only be applied to somewhat simple systems, consisting of single-layer metal structures with cylindrical or rectangular holes. Furthermore, these approaches rely on approximations which break down with particular structures, or assumptions which do not apply in some regions. Additionally, they are somewhat limited in the results they provide. Thus, all of the theoretical and numerical methods are best complemented with a full-field simulation approach which numerically solves Maxwell's equations (Eqs. 2.2) in a complicated region.

6.2 The finite element method

In what follows here, we frame our discussion based on Ansoft HFSS$^{\mathrm{TM}}$ electromagnetic simulation software, although much of it applies equally well to other commercially available software. HFSS utilizes a finite element (FE) method for solving Maxwell's equations.[76] In this approach, the entire structure is divided up into smaller, tetrahedral finite regions, i.e. mesh cells, each with a local solution to Maxwell's equations. The application of boundary conditions between each cell yields a complete solution for the entire structure.

Generally speaking, the finer the mesh, the closer the numerical solution is to an actual, physically-measured system; an infinitesimally fine mesh should exactly match a physical system. However, this comes at the expense of computational efficiency. Typically, there is a balance to be struck between a finer mesh and less-accurate solutions, and intelligent meshing algorithms can greatly improve on simulation accuracy without sacrificing computational efficiency. It is most important to have a fine mesh in a region where the electromagnetic fields are expected to vary rapidly, while in regions where the field varies slowly it is sufficient to use a coarse mesh. HFSS's adaptive meshing algorithms are usually adept at generating appropriate meshes for the regions, although it is possible to override the default approaches when knowledge of the system can better guide the meshing method.

In this thesis we use two different types of solution methods: Eigenmode and driven modal. An eigenmode solution finds the frequencies at which a structure electromagnetically resonates, independent of any particular electromagnetic excitation or source. We use this method to generate the dispersion curves simulated in Chapter 3. Driven modal solutions, on the other hand, calculate the scattering parameters for materials that are excited by an electromagnetic source. We use this method for calculating reflection, transmission, and other related parameters of structures as functions of frequency, etc. This latter method is also the more common approach used in this thesis.

6.2.1 Boundary conditions and excitations

Finite element simulations require one to define a large physical region to be simulated, not just the metamaterial structure of interest. That is, one must extend the simulation region beyond the narrowly-defined region containing the structure to include air or other dielectrics around (i.e. above or below) the metamaterial, see Fig. 6.1. This is unlike some other methods, such integral equation or boundary element method solutions, where it is sufficient to

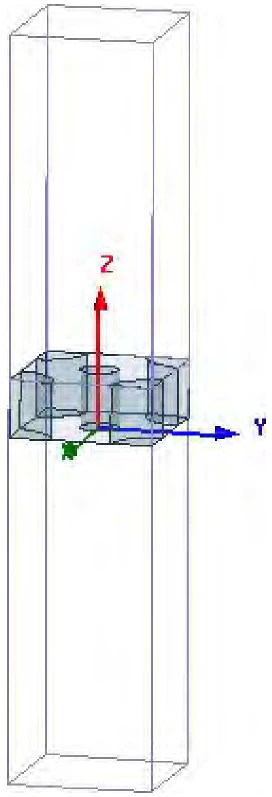

Figure 6.1: An example of a simulated region in HFSS. The metamaterial structure is in the middle, topped by regions of dielectric. In this case, periodic (master/slave) boundary conditions are applied at the sides of the structure.

describe just the "active" material.[76, 77] We will call the complete physical structure being simulated the "superstructure."

Furthermore, boundary conditions (BCs) must be set at the spatial extents of the superstructure and, for driven modal solutions, excitations must be defined. These conditions are determined by the type of structure being simulated. For example, to simulate a finite structure under plane wave excitation, radiation (incident or outward radiating, as appropriate) or perfectly-matched layer (PML) boundary conditions are used on the outer surfaces. For infinitely periodic arrays, on the other hand, master/slave (periodic) or perfect-E/perfect-H (mirror symmetry) boundary conditions are used on the periodic surfaces, typically in conjunction with a Floquet port (for master/slave BCs) or wave port (for perfect-E/H BCs).

Each different combination of boundary conditions and excitations often requires careful attention to simulation setup to ensure physical results. For example, periodic structures which lack mirror symmetry should not be simulated using perfect-E/H BCs with a waveport excitation; instead they require use of master/slave boundaries, with Floquet port excitations. In all cases, the total size of the simulated superstructure must be large-enough to capture any near-field effects, but not too large as to needlessly increase the simulation time.

Additionally, the inherently-finite size of the region introduces some artifacts to the simulation, some of which can be dealt with. Specifically, the distance between the top (and bottom) of the superstructure and the metamaterial – i.e. the distance between where radiation enters the system and the region of interest – should be large-enough such that any near-field effects have decayed away before they reach those surfaces. This is particularly important for port-type boundaries, or solutions using far-field probes, as the computer does not know that if the fields impinging on the port or probe are local or truly far-field. In those cases, if non-decayed, near fields impinge on the port or far-field surface, they will be included in the far-field reflection/transmission values, and will often yield values of total reflection plus transmission greater than one – i.e. lack of energy conservation within the simulation.

For finite structures, it is usually simple-enough to increase the complete structure size. However, for periodic structures, there is another complication. As we discussed in Chapter 4, the evanescent decay length of the near fields approaches infinity approaching diffraction frequencies (see Fig. 4.5). For any finite-height periodic structure, there will be some frequency below diffraction above which the decay length of the near fields is larger than the structure's total spatial extent. In these cases, the problem of energy conser-

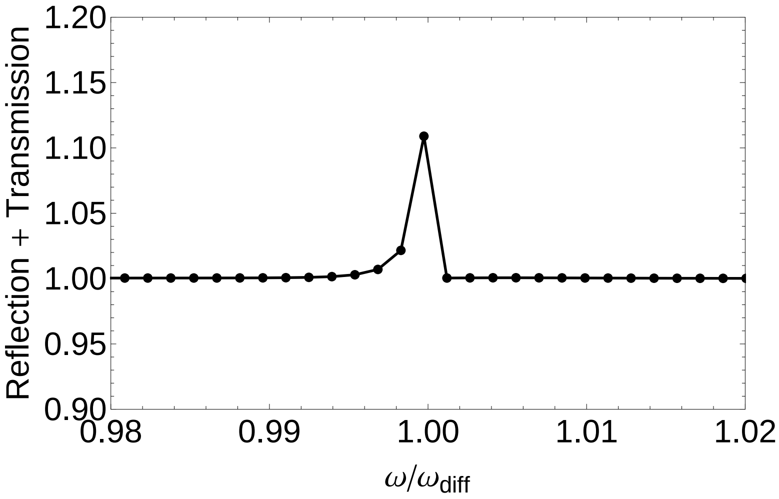

Figure 6.2: The total reflection plus transmission for a PEC aperture array structure near a diffraction frequency, ω_{diff}. Approaching the diffraction frequency from below leads to non-physical greater than one values when the near fields reach the extent of the superstructure.

vation is inescapable, and simulated results within this region are inherently nonphysical. Figure 6.2 shows a plot of total reflection plus transmission for a PEC cylindrical periodic aperture array near a diffraction frequency, ω_{diff}. The plot illustrates this problem, as approaching the diffraction frequency from below leads to non-physical values of this sum, as the near fields reach the extent of the superstructure. Note that the frequency range affected by this varies for different structures.

6.2.2 Typical methods of extracting relevant solution information

The resonant properties of the cavity modes can be analyzed using a few different methods. The easiest, and typically fastest way to extract reflection and transmission results is using waveports. For this approach, HFSS directly calculates the S-parameters for all modes, which are easily used to calculate the reflection and transmission coefficients. For finite structures with radiation boundary conditions one can either integrate the outward-facing Poynting vector (i.e. net energy flow) over the exterior surface, which is tedious to do and not-always entirely accurate in HFSS, or set up a far-field probe to measure it. With all of these approaches, the structure must be sufficiently large to ensure the exterior or far field probe surface is far enough away so near field effects can decay, as previously discussed.

Additionally, the cavity resonances can be determined indirectly from the extracted values of reflection and transmission. In order to excite a cavity mode resonance, there must be a non-zero component of the incident electric (TM) or magnetic (TE) fields perpendicular to the plane of the metal-superstrate interface in order to excite a TE or TM cavity mode, see Chapter 5. Thus, light striking the metamaterial normal to this interface, which has neither an electric nor a magnetic field component perpendicular to the interface (TEM), can not *directly* couple to a cavity mode. However, off-normal reflected waves, both propagating and evanescent, do have nonzero z-components to the fields and can thus couple to a cavity mode. Therefore, in order to couple light to a cavity mode, light must reflect in an off-normal direction. Thus, if light strikes the metamaterial normally at an off-resonance frequency, the light will be reflected back normally, as well. However, at a resonance, the light is coupled, via the excited cavity mode, into off-normal reflection. In a simulation, these scattered fields are captured by higher order Floquet ports, and there is a corresponding dip in the normal reflection.

While these straightforward metrics are useful for a simple comparison to standard experimental measurements, they are insufficient for calculating other properties, specifically field or absorption localization. For these quantities, one must make extensive use of the HFSS field calculator. This tool grants access to the raw, solved field data. For example, to measure the total electromagnetic energy absorbed in a particular piece of a structure, the volume loss density (i.e. the fraction of incident energy absorbed) derived from the solved electromagnetic fields can be directly integrated over the volume or surface of interest. Similarly, to measure field strength, the time-averaged electromagnetic energy density,

$$u = \epsilon \left|E\right]^2 + \left|B\right|^2, \tag{6.1}$$

of the solved electromagnetic fields can likewise be directly integrated over any volume or surface.[24] At cavity resonances, the ratio of the cavity energy to the total energy will exhibit a maximum. Although the magnitude of the maximum is dependant on the size of the simulated structure, i.e. the volume of the superstrate in the simulated structure, and is therefore somewhat arbitrary, we can still use the *position* of the maximum (with respect to wavelength or frequency) to locate cavity resonances. This metric is useful for determining where in a structure the fields or absorption are localized, however these results are generally difficult to measure, and thus verify experimentally.

While both the direct and indirect methods are each sufficient to characterize the cavity resonances, the choice of method is generally determined by the choice of boundary conditions or desired functionality. For example, for non-periodic structures, with radiation and/or PML boundary conditions, where there are no S-parameters, the method of choice is the direct integration of the reflected power or electromagnetic energy densities. This process, however, can be quite time and resource intensive, as the solved fields must

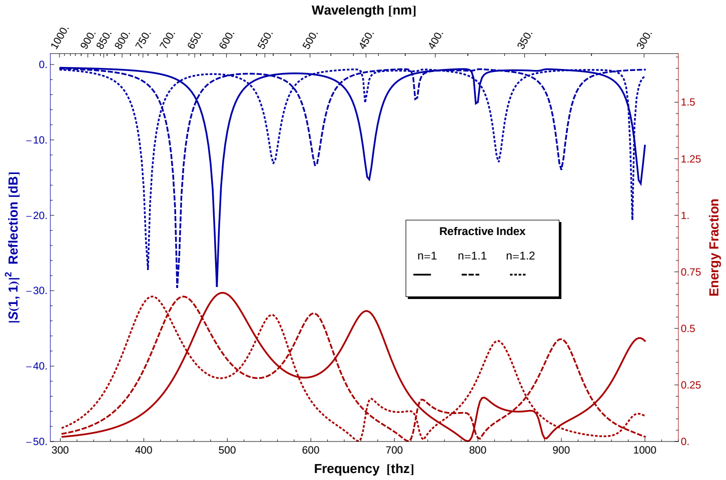

Figure 6.3: Resonance response of periodic arrays of rectangular cavities calculated via two different methods for three different indices of refraction (dielectric fills superstrate and cavity). The dips in reflected power correspond to the peaks in energy density. The apparent narrowness of the peaks in reflected power are due to the log (dB) scale. Here $h = 400$ nm, $\ell = 316.4$ nm and $w = 79.1$ nm with a period of 380 nm.

be saved and energies calculated at every solved frequency. For periodic and Floquet port structures, however, it is quicker to find the S-parameters than to integrate the energies. Results for both methods are compared in Fig. 6.3, and we make use of both approaches in this thesis.

6.3 Material parameters

HFSS, like many other electromagnetic simulation software, is primarily designed to model structures at microwave frequencies. As such, unless otherwise specified, it utilizes a surface impedance-type boundary condition on any metals with bulk conductivities greater than 10^5 Siemens/meter.[76] Even when forced to "solve inside" a high-conductivity structure, it still utilizes the bulk-conductivity values, often extrapolated from microwave frequencies to higher frequencies, to calculate the effective dielectric properties. However, as discussed in Chapter 3, metals at optical frequencies are not well-described by a simple, high value of bulk conductivity, see Fig. 3.1. Thus, although the mathematics of Maxwell's equations is scale invariant, and HFSS can, in principle solve at optical frequencies, extra care must be taken with metals.

Furthermore, HFSS also includes a rather large materials library, which includes metals, dielectrics, and semiconductors. However, these, too, are based on their values at microwave frequencies. For example, the model library claims that water has a constant dielectric permeability of $\epsilon = 81$ (Fig. 6.4(a)), while water's actual dielectric constant is closer to $\epsilon = 1.33^2$, and is dispersive, see Fig. 6.4(b).[78] Therefore, as with metals in HFSS, one can not use the default materials at optical frequencies.

Fortunately, HFSS allows users to create their own materials. Thus, when simulating materials at optical frequencies, one must import experimental values, or utilize theoretical expressions for the dielectric properties. However, the necessity of solving inside all metal structures adds significantly to the complexity of the simulation, and thus demands increased computational

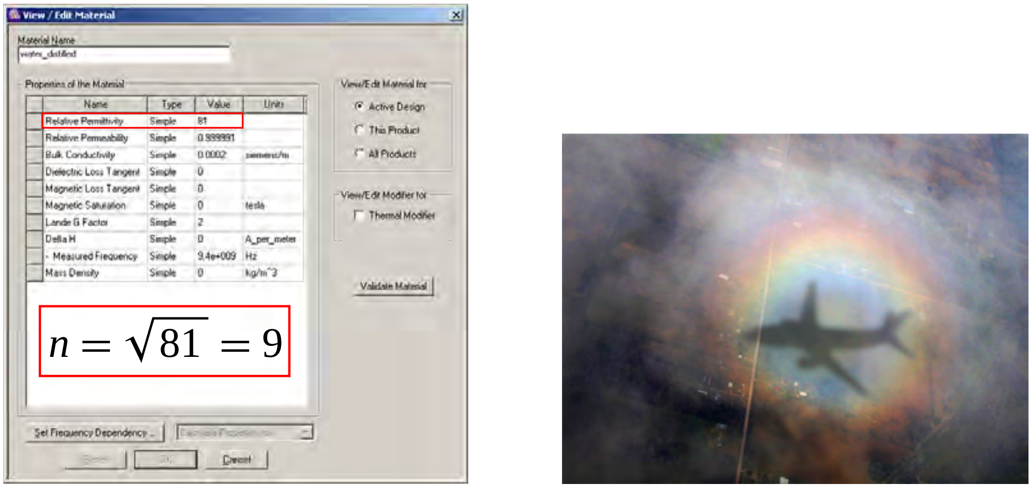

View / Edit Material

Material Name: water_distilled

Properties of the Material

Name	Type	Value	Units
Relative Permittivity	Simple	81	
Relative Permeability	Simple	0.999991	
Bulk Conductivity	Simple	0.0002	siemens/m
Dielectric Loss Tangent	Simple	0	
Magnetic Loss Tangent	Simple	0	
Magnetic Saturation	Simple	0	tesla
Lande G Factor	Simple	2	
Delta H	Simple	0	A_per_meter
- Measured Frequency	Simple	9.4e+009	Hz
Mass Density	Simple	0	kg/m^3

$$n = \sqrt{81} = 9$$

View/Edit Material for: ● Active Design ○ This Product ○ All Products

View/Edit Modifier for: ☐ Thermal Modifier

(a) The built-in material properties for water in HFSS's materials library.

(b) The true, dispersive optical response of water.[79]

Figure 6.4: An illustration of the problems with using the built-in material parameters for metals at optical frequencies.

resources. Generally speaking, the number of mesh cells required for equivalent volumes of metal and a simple dielectric differ by an order of magnitude. That is, while a particular volume of water may require 10^4 mesh cells in order to reasonably model it, the same volume of gold requires 10^5.

6.3.1 Efficient simulation of optical metals

The order of magnitude difference in computation cost per volume of metals versus dielectrics at optical frequencies necessitates an efficient method of simulating metamaterials with relatively-large volumes of metal. There are two basic approaches towards overcoming this issue. The first is to minimize

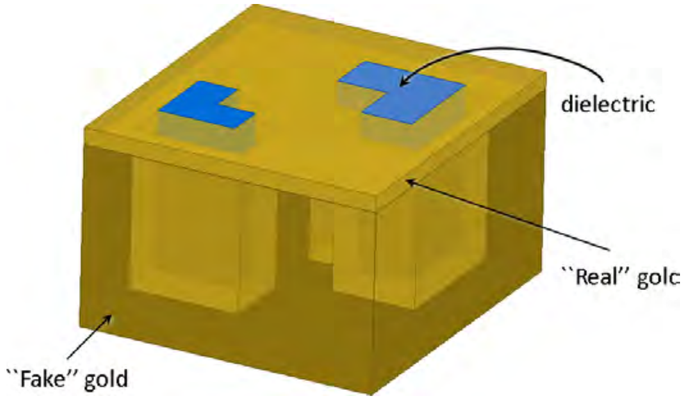

Figure 6.5: Using the arguments of the SDBC to simplify FE simulations for complicated structures. Here, we have minimized the amount of "real metal" in the simulation.

the amount of metal actually meshed, and the second is to utilize parallelization – "domain decomposition" in HFSS – and a high-performance computing cluster.

To develop an the first approach, where we try to minimize the amount of metal which HFSS must mesh, we will use the physical arguments behind the SDBC, discussed in Chapter 3. Specifically, we again make use of the argument that the majority of the fields that penetrate the metal are ultimately constrained within a skin depth into the metal, and beyond that point it is effectively a PEC. Thus, in defining material parameters for the metal portions of the structure, it is only necessary to include a thin film of "real" metal (i.e. the true material parameters) and to treat the rest of the metal either using a surface impedance boundary condition as in the microwave range, or even to set it as a PEC, see Fig. 6.5. Unlike for the analytical calculations done in that chapter, for numerical purposes it is necessary to extend the "real metal" portion of the structure up to two or three skin depths. Furthermore, although in Chapter 3 we analytically showed results for simple rectangular or cylindrical apertures, we can use this approach for complicated structures in simulation, where an analytical approach may not be feasible, see Fig. 6.5.

Although minimizing the amount of metal simulated in a structure can often allow a previously computationally-intractable structure to be simulated, there are situations where this is either inapplicable or insufficient. For example, if the structure is electrically large, or if the material has many apertures, especially if they are each only a skin depth or two away from each other. In these cases the number of mesh cells requires more RAM than a typical machine has. While this can be solved by throwing more RAM at the problem, it is often more efficient to utilize a parallelization method. In this approach, the superstructure is broken smaller pieces, each one solved on a different machine. Then, the boundaries are stitched together with appropriate boundary conditions, as if each section of superstructure was an individual mesh cell.[1] There are some limitations to implementing this

---

[1] It is worthwhile noting that is a conceptual description of the approach; the details

approach, most notably it is not available in HFSS (or most other solvers) with master/slave periodic boundary conditions, but this is another powerful approach for efficient simulation of structures with large amounts of optical metals.

6.4 Optimization approaches

Another advantage of using computer simulation in the metamaterial design process that is worthwhile briefly noting is the ability to optimize a structure. That is, given a set of constraints and a starting structure, HFSS can algorithmically change various structural or material parameters to find a new structure which better meets the design goals.[76] The method we use most often is the gradient-based, Quasi-Newton approach,[80] which is based on Newton's root-finding algorithm.[81]

We have found, in practice, that these optimization methods work best when the initial model is fairly close to the having the desired properties. For example, in the fabricated microwave structure discussed in Chapter 9, we initially designed the structure using ECR, followed by some additional simulations with more complicated dielectric materials. We found a decent device, see Table 6.1(a), which became an excellent device, see Table 6.1(b),

---

involve block-matrix algebra and various preconditioning tricks, see the HFSS Manual for complete details.[76]

	Absolute Absorption (%)	
Frequency (GHz)	E_1	E_2
8.1	83	3
9.6	18	73

(a) The performance of the initially-guessed structure.

	Absolute Absorption (%)	
Frequency (GHz)	E_1	E_2
8.1	96	1
9.6	5	93

(b) The performance of the optimized structure.

Table 6.1: The improvement in a device's performance after optimization.

after solving 120 variations in just over 3.5 hours.

Part III

A Novel Application: Light-splitting metamaterials

Chapter 7

Horizontally-oriented multi-junction solar cells

7.1 Introduction

The search for renewable, environmentally benign energy sources is one of the most significant technical challenges of the 21st century.[82] Novel light harvesting techniques, such as dye-sensitized Grätzel cells, are an important innovation which allows many different methods of charge separation that do not have the limitations of traditional semiconductor solar cells.[83, 84] For example, many different biomimetic charge separation methods exist, all of which require concentrated light in a specified bandwidth.[85, 86] However, these devices generally have the lowest overall cell efficiency of all research solar cells, see Fig. 7.1, on the order of 10%. This is primarily due to the fairly-narrow bandwidth of absorption in these materials.

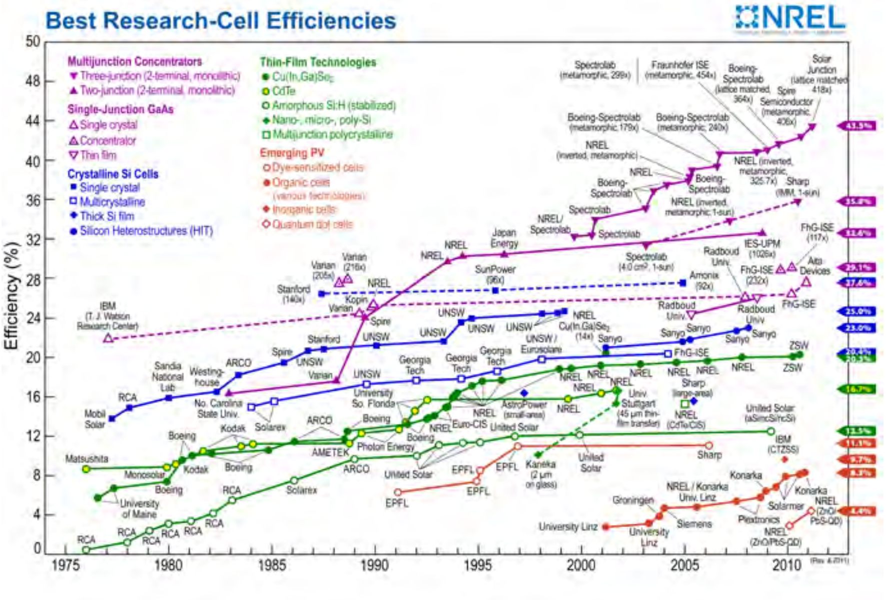

Figure 7.1: The best research solar cell efficiencies, plotted as a function of time.[87] Multi-junction solar cells (purple) show the highest efficiencies.

On the other side of the efficiency spectrum are multi-junction (MJ) solar cells, with efficiencies approaching 45%. A traditional silicon (or any semiconductor) solar cell is bandgap limited. That is, below the bandgap photons are not absorbed, and above the bandgap they only generate the bandgap energy per photon, even for higher-energy photons. A multi-junction solar cell (see Fig. 7.2(a)), on the other hand uses a few different semiconductors in a vertical stack to try and more efficiently utilize a broader portion of the solar spectrum, see Fig. 7.2(b). While these cells are significantly more efficient than their competition, they are also very expensive to manufacture, and thus are typically used in concentrator arrays which limits their broad usage.[88]

7.2 Metamaterials for solar energy

We can use a metamaterial to achieve the benefits of multi-junction devices while utilizing many of the new charge separation techniques. In fact, it has been shown that separating light into different physical regions based on wavelength can greatly increase the overall efficiency of solar cells based on these technologies.[91–93] However, those devices are large and expensive to manufacture, while a metamaterial-based device would consist of a single metamaterial layer, see Fig. 7.3. In a metamaterial device, the light is split and concentrated, sorting photons of different bandwidths into different regions of the structure. Each region can then be filled with the appropriate absorber for that bandwidth, creating a horizontally-oriented multi-junction solar cell. This enhanced optical concentration, along with the ability to separate different bandwidths of light in different physical regions of a horizontally-oriented metamaterial can yield significantly greater solar cell efficiencies when coupled with new charge separation methods.

It is important to note that there are some limitations to this approach. Firstly, there are significant fabrication challenges in making these devices.

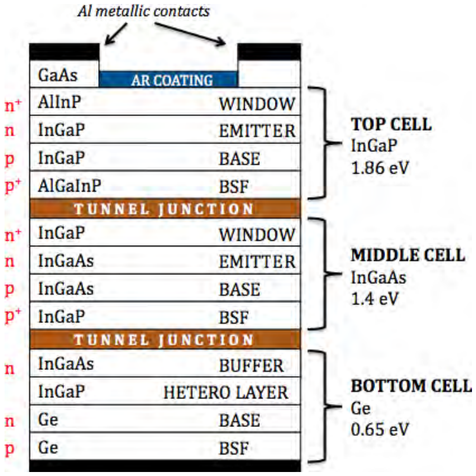

(a) A schematic of a traditional multi-junction solar cell.[89]

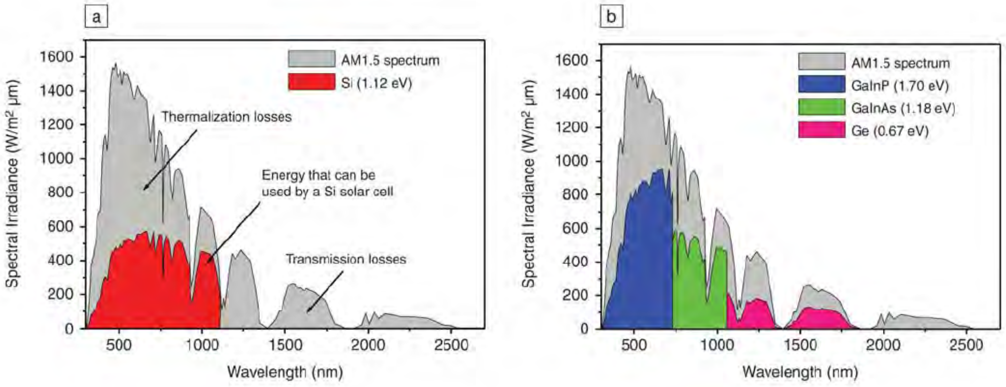

(b) The solar spectral irradiance overlayed with $\boxed{a}$ a single-cell silicon solar cell's absorption spectrum and, $\boxed{b}$ a multi-junction cell's absorption.[90] The multi-junction cell can more efficiently use a greater portion of the solar spectrum.

Figure 7.2: Some properties of a traditional multi-junction solar cell.

The small feature sizes means that any device based on this sort of metamaterial must be fabricated initially using electron beam lithography, followed by imprint lithography. Furthermore, as discussed many times in this thesis, metals at optical frequencies are far from perfect conductors, and can actually absorb a sizeable amount in incident light. Additionally, for a multi-junction device for electricity generation, the individual cavities must be electrically isolated from each other to ensure optimum charge extraction, which has additional design implications. Moreover, most of the biomimetic, or dye-based absorbers require immersion in water. Finally, all of these structures must be designed with a periodicity small-enough that any frequencies of interest are below diffraction, for reasons discussed in Section 4.3. Nevertheless, this is a novel approach, which is worth investigation.

7.2.1 Mechanism of photon sorting

The mechanism responsible for the light channeling towards, and into the cavities is explained if one considers the time-reversed situation of light exiting an aperture. For linear materials (see [94] for exceptions), Maxwell's equations and its solutions are invariant under complex conjugation.[24] In a lossless structure this simply amounts to time reversal symmetry (i.e. a $e^{i\omega t}$ time dependence transforms to $e^{-i\omega t}$), while a lossy dielectric transforms to

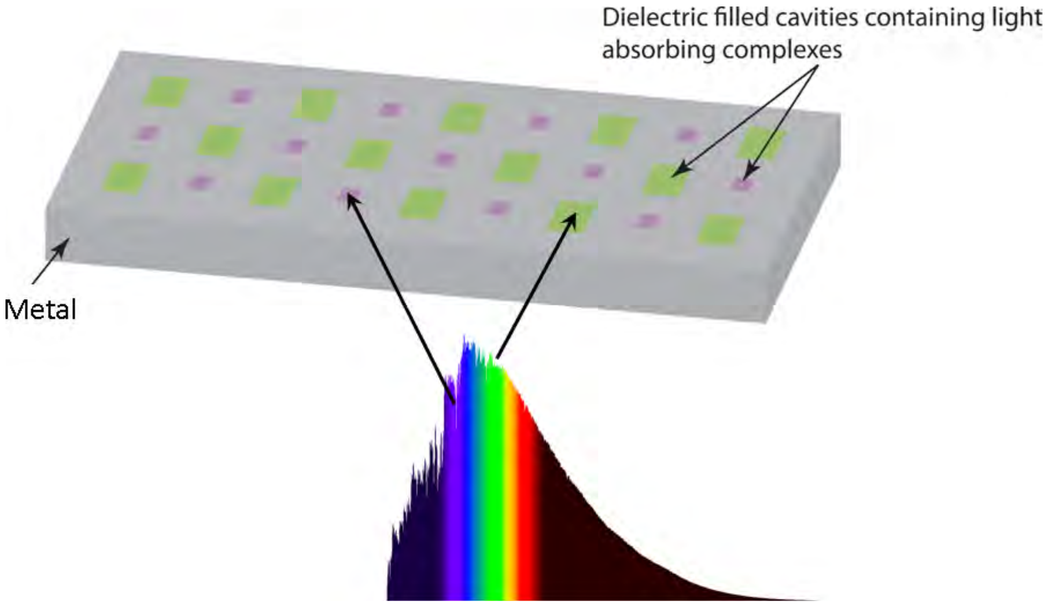

Figure 7.3: A metamaterial-based, horizontally-oriented multi-junction solar cell.

a gain material, in addition to time-reversal. Considering the time-reversed version of our structure, light generated at resonance by a gain material within an individual cavity, upon exiting, will spread out and form a diffuse beam.[95] Now, for an infinitely periodic array of apertures with gain media, in which radiation is generated with well-defined phase relationships, the light exiting each aperture diffracts in the same way as a single aperture, and will constructively interfere with the light exiting all the other apertures to create an outgoing plane wave. Note that each array of identical cavities will resonate (and radiate) light at their own resonant frequencies, independent from the (different) resonances of the other-sized cavities. The collective effect of light radiating from each aperture results in plane waves in the far field. Thus, transforming back to the forward-time with a lossy material, it is expected that light will converge towards (i.e. be channeled into) the cavities as it approaches the entrances to the apertures, and ultimately be absorbed.

7.3 Outlook

There has been some prior research on multi-band frequency selective surfaces to increase the capabilities of multi-frequency microwave antennas by adding subreflectors capable of operating at multi-frequency bands,[96–98] and in bimetallic nanoantennas,[99] or plasmonic gratings for the visible regime.[100] The devices demonstrated in these studies lack any multi-functional properties (i.e., photon sorting, localization and absorption), unlike the structures described in this work.

Some previous work on polarization-splitting,[60] and wavelength-selective compound grating structures,[11, 59, 60, 101–103] dealt primarily with transmission properties, and the devices were not optimized for absorption. It has been established that light can be localized in a single region of a nano-aperture structure,[104] however it has been demonstrated only at a single spatial location. While there is some work involving periodic grating structures for frequency selective absorption of electromagnetic radiation,[105–

107] these devices are highly polarization-dependent, a limitation that is not shared by the devices described in this work.

In this part of the thesis, we present two different classes of polarization-independent, photon-sorting metamaterials which operate at various portions of the electromagnetic spectrum. The first device is an early prototype, with interspersed L-shaped cavities. This device was simulated under PEC and optical metal conditions, fabricated, and nominally characterized. The second device contains interspersed cylindrical cavities, and has been simulated, fabricated and characterized for the microwave spectrum, and a path towards IR and visible wavelengths has been shown in simulation.

Chapter 8

Rectangular and L-shaped cavity arrays

8.1 Introduction

In this chapter we design a light-splitting and concentrating, polarization-independent metamaterial that operates at optical frequencies, although the initial design assumes PEC metals. The material is a compound subwavelength cavity array, consisting of two L-shaped cavities, arranged in a 700nm × 900nm periodic array. The cavities themselves are not deeply subwavelength in size; feature sizes are approximately $\lambda/(2\sqrt{\epsilon})$ where ϵ is the dielectric permittivity within the cavities. Thus from the perspective of incident radiation of wavelength λ, the material does not appear to be of homogenous composition with spatially-independent, effective values of ϵ.

This device concentrates electromagnetic energy within the cavities, with the electromagnetic energy density in the excited structure as much as two orders of magnitude greater than that in the unexcited structure in the microwave regime. These values correspond to very high light splitting and concentration efficiencies, with 97-99% of the concentrated light in the desired cavity and a light concentration factor as great as 292.

We also discuss the design, fabrication and characterization of a scaled-down structure, designed to operate in the visible regime. While light splitting was not experimentally verified due to technical and financial considerations, there is some indirect experimental evidence of enhanced field buildup within the cavities. Note, that all of the initial simulations use PEC conditions on the metal even though the dimensions are set for optical frequencies; changing to optical metals shifts the resonances down, as described in Chapter 3.

8.2 Metamaterial design

By adjusting the dimensions of the cavity one can tune the resonance response of the structure to build up a field resonance inside the cavities at particular target wavelengths λ, see Chapter 4. Here, however, we will ultimately be analyzing structures which are difficult to describe using the ECR model, and we suffice with the naive approach described in 4.2.1. That is, here we choose the initial dimensions of rectangular cavity structures based on Fabry-Pérot waveguide theory, where the cutoff frequencies ω_{mn} or wavelengths λ_{mn} are given by

$$\frac{\omega_{mn}}{c} = \frac{2\pi}{\lambda_{mn}} = \frac{\pi}{\sqrt{\epsilon}} \left(\frac{m^2}{\ell^2} + \frac{n^2}{w^2} \right)^{1/2}, \tag{8.1}$$

where ℓ is the length of the cavity and w is the width, ϵ is the dielectric constant of the material filling the cavity, and m and n are integers. The lowest order cutoff mode is determined by the larger of the two cavity dimensions ℓ, see Fig. 8.1(a). Inverting this equation to solve for ℓ in terms of the target cutoff wavelength $\lambda_{mn} = \lambda_{10} \equiv \lambda$ gives

$$\ell = \lambda/(2\sqrt{\epsilon}). \tag{8.2}$$

Structures with a 2:1 aspect ratio are easily fabricated using standard techniques. As such, we choose

$$w = \lambda/(4\sqrt{\epsilon}). \tag{8.3}$$

In practice, however, adjusting the width of the cavity introduces a small shift in the cavity resonance, and affects the Q of the cavity, see Fig. 8.1(b). Additionally, we choose the thickness, h, to be

$$h = \lambda/\sqrt{\epsilon} \tag{8.4}$$

to allow a complete node in the vertical direction; adjusting the thickness also introduces a shift in resonance and changes the Q of the cavity, see Fig. 8.1(c). Thus, all cavity dimensions are now given in terms of the target wavelength. Furthermore, scaling all dimensions of the complete structure by a factor α, while keeping ϵ constant, shifts the resonances by $\alpha\lambda_0$ or ω_0/α, see Fig. 8.1(d).

8.2.1 Demonstration of polarization independence

The optical response of arrays of rectangular structures, however, is polarization dependent, which greatly limits their use in solar applications. The cavity mode response of the rectangular structures is tied strongly to light polarized along the short side of the rectangle, see Fig. 8.2(a). Light polarized along the long side of the rectangle is reflected back with minimal cavity interaction. However, light polarized along the short side interacts strongly with the cavity, exciting a cavity mode resonance, which couples light into off-normal reflected modes. The maximum dip in normal reflection at 618 nm shown in Fig. 8.2(a) corresponds to strong excitation of the cavity, which can be seen in the field structure in the inset.

Recently, "L-shaped," open channel structures have been shown to posses polarization-independent responses.[108, 109] Here we extend this analysis to

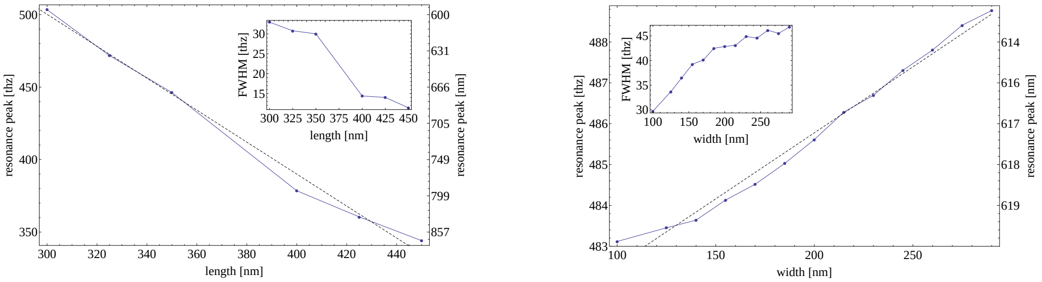

(a) Changing only the length of a rectangular cavity. Here $h = 632.8$ nm, $w = 100$ nm with an x and y period of 700 nm and 900 nm respectively. The line of best fit (dashed) corresponds to a resonance shift of 1.102 THz/nm for changing lengths.

(b) Changing only the width of a rectangular cavity. Here $h = 632.8$ nm, $\ell = 316.4$ nm with an x and y period of 700 nm and 900 nm respectively. The line of best fit (dashed) corresponds to a resonance shift of 0.032 THz/nm for changing widths.

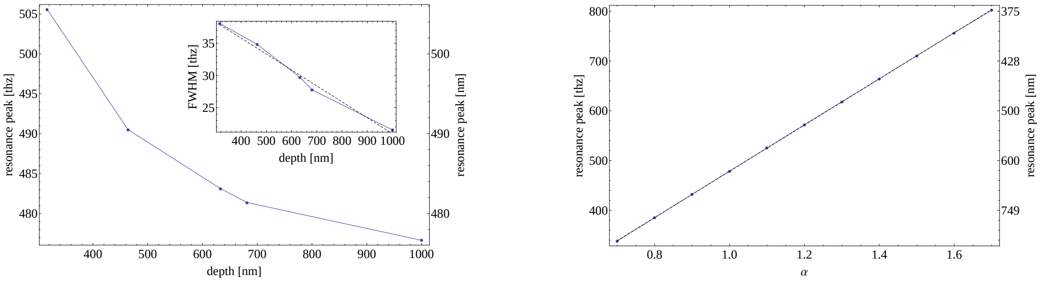

(c) Changing only the depth of a rectangular cavity. Here $w = 100$ nm, $\ell = 316.4$ nm with an x and y period of 700 nm and 900 nm respectively. The line of best fit (inset, dashed) corresponds to a FWHM shift of -0.025 THz/nm for changing depths.

(d) Scaling all cavity dimensions by the same factor, α, with nominal values of $h = 158.2$ nm, $\ell = 316.4$ nm and $w = 158.2$ nm with a period of 1.2656 μm.

Figure 8.1: The effect of cavity dimensions length (a), width (b) and depth (c), as well as uniform structure scaling (d) on resonance response of rectangular cavities embedded in a perfect electric conductor. The inset plots show the full-width-half-max Q of the resonance fit to a Gaussian.

include closed cavities. To create a polarization-independent cavity we join two, perpendicularly oriented rectangular cavities at a corner to create an L-shaped cavity. The L-shaped cavities, display nearly identical responses to both polarizations of light, see Fig. 8.2(b). Light polarized along either direction interacts with the long side of whichever rectangle is in line with its polarization, exciting cavity mode resonances in one leg of the structure. These resonances, in turn, couple light into off-normal reflected modes, causing the decrease in normal reflection at $\lambda = 609$ nm seen in Fig. 8.2(b). Here, again, the maximum dip in normal reflection at 609 nm corresponds to strong excitation of the cavity, which can be seen in the field structure in the inset.

It is worthwhile noting that although it is through one leg of the L that light couples to the cavity, the fields ultimately spread throughout the entire cavity, see Fig. 8.3. This means that all polarization can interact with absorbing molecules throughout the entire structure. Additionally, this mechanism has potential applications in polarization rotating metamaterials, or possibly for making a non-reciprocal structure.

After tuning the responses of two individual cavities to two different wavelength bands, we tile the two different cavities in a periodic array. Each cavity targets a separate wavelength band, and, as discussed earlier, can be filled with different light-absorbing complexes, see Fig. 8.4.

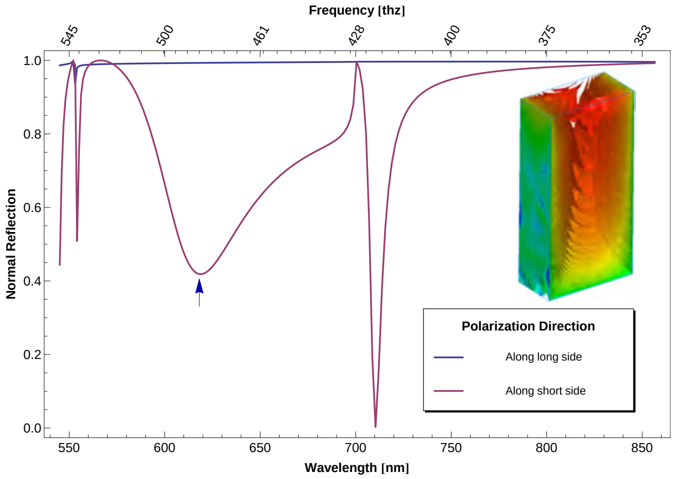

(a) Reflection from *rectangular* cavities, with cavity mode indicated by the arrow at $\lambda = 618$ nm. The large dip in normal reflection at ~ 710 nm corresponds to scattering due to diffraction. Inset shows magnitude of the electric field in the cavity at $\lambda = 618$ nm.

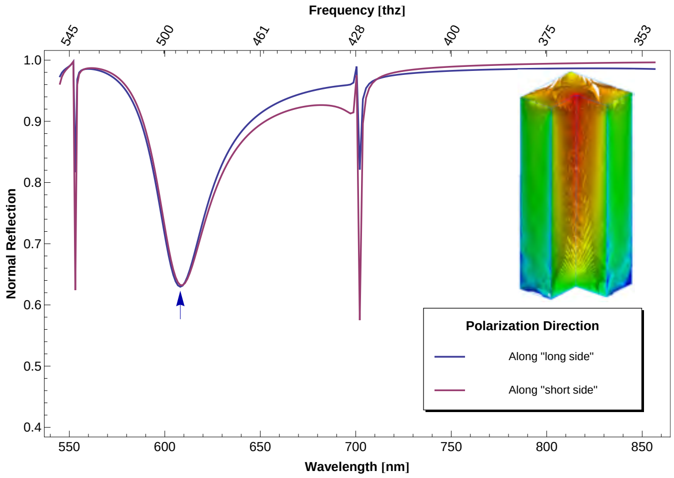

(b) Reflection from *L-shaped* cavities, with cavity mode indicated by the arrow at $\lambda = 609$ nm. The large dip in normal reflection at ~ 710 nm corresponds to scattering due to diffraction. Inset shows magnitude of the electric field in the cavity at $\lambda = 609$ nm.

Figure 8.2: The resonance response of the rectangular (a) and L-shaped (b) cavities. Plots show only the normal reflection from the metamaterial structures for each polarization while the field profiles are shown using the entire field results (i.e. both polarizations).

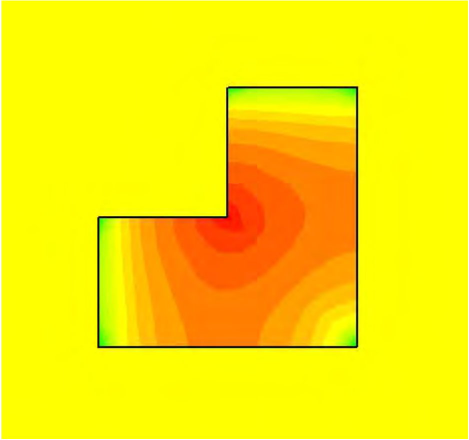

Figure 8.3: Magnitude of the electric field in an excited L cavity excited via light polarized along the y-direction. It can be seen that the whole cavity participates in the resonance regardless of the polarization of the incident light.

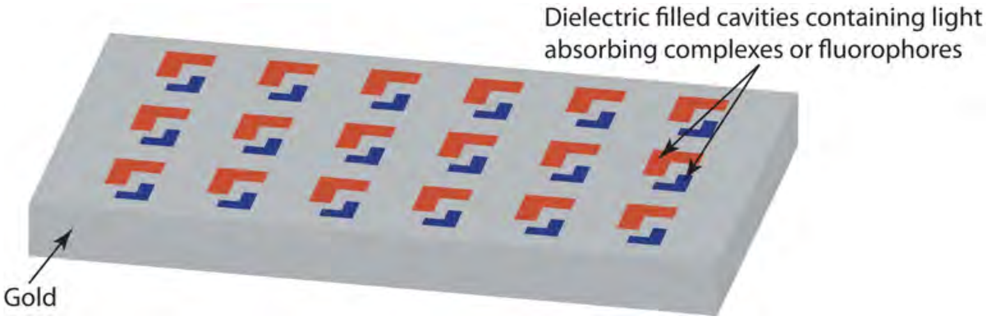

Figure 8.4: Schematic of interspersed L-shaped cavity metamaterial structure.

8.3 PEC simulation results

We initially chose to target wavelengths of 790 nm and 632 nm for the two cavities, corresponding to two standard fluorophores' absorbtion peaks for future experimental verification. The dimensions of the rectangular cavities used to make the legs of the L's are $\ell_1 = 254.8$ nm, $w_1 = 127.4$ nm, $\ell_2 = 328.3$ nm, $w_2 = 164.2$ nm with a uniform depth of 474.6 nm, and with a pitch of 700 nm and 900 nm in the x and y directions. The cavities are embedded in a perfect electric conducting film.

Simulations were conducted using vacuum as the dielectric in both the cavity and superstrate; for other dielectrics the resonance shifts, as discussed earlier. Fig. 8.5 shows the simulated intensity of light specularly reflected from the metamaterial surface. As discussed earlier, dips in the reflection intensity are correlated with optical resonances occurring within the cavity. We have labeled the two cavity resonances at 632nm and 790nm, which are excited by both polarizations.

Note, that although structures with only one L per unit cell are excited equally by both polarizations, see Fig. 8.2(b), in this tiled array the response is not identical for both polarizations. Here the two cavities are not oriented in the same direction and the fields interact with both structures simultaneously. This effect can be seen in Fig. 8.6(a) where one leg of the smaller L is excited asymmetrically and off its resonance wavelength. Nevertheless, the response is polarization-independent in the target cavities.

Additionally, this plot only shows the specularly reflected signal. Diffracted waves, which are picked up by other, higher-order ports (which may or may not be included in the simulation), also cause significant, sharp dips in the specular reflection. These points are indicated by arrows in the figure at 700 nm and 900 nm, the first-order diffraction points, and the dips in reflection are not indicative of a cavity mode.

Although useful for identifying the position of cavity mode resonances, the dips in specular reflection are relatively small, and are not the best metric for analyzing the capability of a structure to strongly concentrate light within the cavity. Furthermore, in the PEC model simulated here, there is no energy loss within the simulated structure, and all of the energy which enters the system must, ultimately, be reflected back out. For a solar energy application, however, the strong fields excited inside the cavity at resonance greatly enhance the inherent absorbtion capabilities of the charge separation complexes, and hence the dips in the reflection and corresponding energy absorbed would be greatly magnified. Nevertheless, we can quantify the capabilities of this structure to both split and concentrate light.

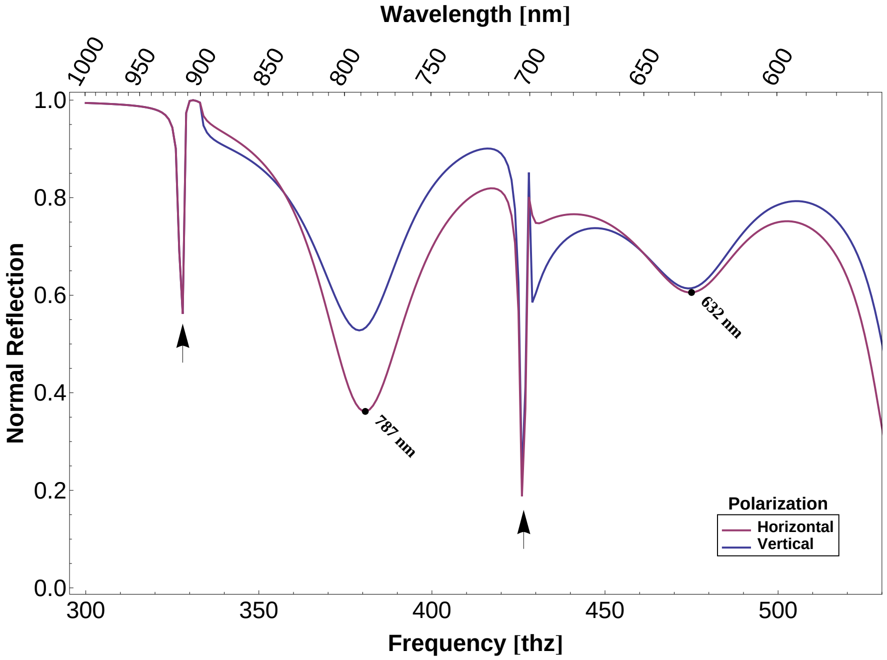

Figure 8.5: The simulated normal reflection intensity of the interspersed L-shaped cavity structure. The arrows point out the lowest order diffraction effects.

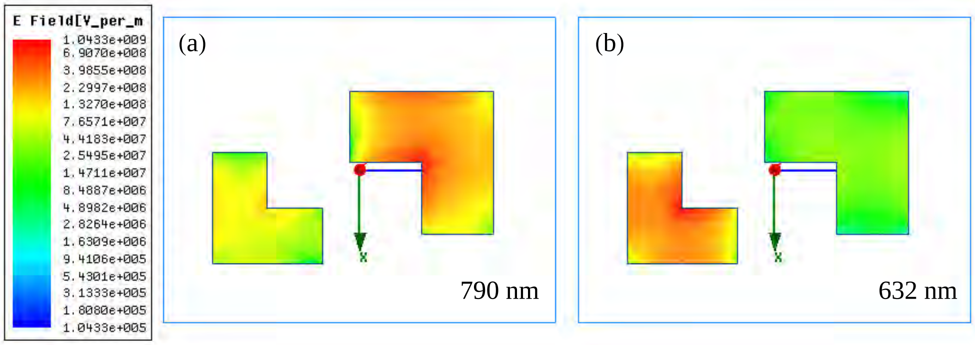

Figure 8.6: Magnitude of the electric field (log scale) at the opening of the L-shaped cavities at $\lambda = 790$ nm (a) representing the maximum excitation of the larger L structure and at $\lambda = 632.8$ nm (b) representing the maximum excitation of the smaller L structure.

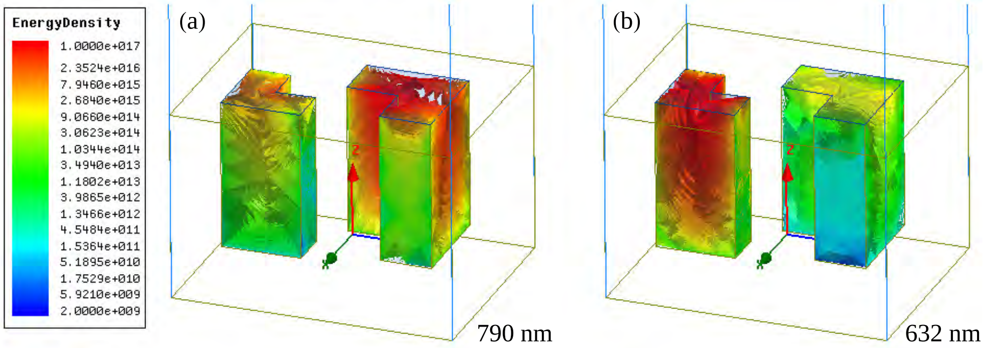

Figure 8.7: Simulated electromagnetic energy density (log scale) inside the cavities at $\lambda = 790$ nm (a) representing the maximum excitation of the larger L structure and at $\lambda = 632.8$ nm (b) representing the maximum excitation of the smaller L structure.

8.3.1 Light splitting and concentration metrics

To confirm that this response is due to the cavities, we calculate the energy stored by the fields in the cavities at the target wavelengths, shown in Fig. 8.7. Observe that when each of the resonances is excited at its associated resonant wavelength, the other structure is largely unexcited (note that the fields are plotted on a logarithmic scale). The ratio of either the energy density ρ or of total energy E in the excited structure versus the unexcited structure represents the quality of the light-splitting between the two cavities.

Thus, to calculate the light splitting efficiency, SE_n, we use the ratio of total electromagnetic energy captured in the desired cavity E_n to the total

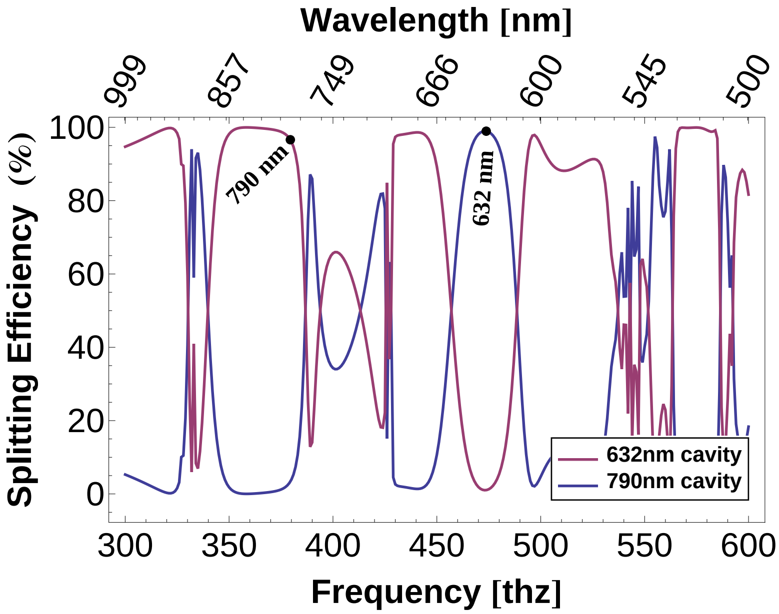

Figure 8.8: Simulated light splitting efficiency for both L structures for a range of frequencies. Targeted resonance locations are labeled.

energy in both cavities, $E_T = E_1 + E_2$

$$SE_n \equiv \frac{E_n}{E_T}, \tag{8.5}$$

i.e. the fraction of photons correctly split. Simulated values of this quantity over a range of frequencies is shown in Fig. 8.8. The targeted resonance locations are labeled. It remains to be understood why the splitting efficiency near the 790nm resonance is wider than at 632nm. The simulated values of E, ρ and SE at our target frequencies are summarized in Table 8.1. Our structures show very strong light splitting at the desired wavelengths. The ratio of total energy in the excited vs. unexcited structure is 387.96 (42.95), and the ratio of energy densities is 664.21 (25.87) at the 632.8 nm (790 nm) wavelength resonance. This corresponds to an extremely-high light separation efficiency of 99.74% (97.72%).

Note, however, that the splitting efficiency does not depend on the amount of light concentrated in the cavities relative to the superstrate, and, as such, must be considered together with the overall light concentration. The light concentration factor CF will depend on the relative increase in total energy E_n stored inside the cavity of volume V_n, as compared to the total energy stored in an equivalent volume of superstrate,

$$E_s^{eq} = \rho_s V_c, \tag{8.6}$$

where ρ_s is the average electromagnetic energy density in the superstrate, normalized by the fractional surface area of the unit cell used by the cavity opening, $S = S_s/S_n$. This is an analogous idea to the enhanced optical transmission metric used to characterize a structure's improvement in transmission.[17, 52] That is

$$CF_n \equiv S\left(\frac{E_n - E_s^{eq}}{E_s^{eq}}\right) = S\left(\frac{\rho_n}{\rho_s} - 1\right). \tag{8.7}$$

This value corresponds to the fractional increase in electromagnetic energy in the cavity compared to the superstrate due to the light-concentrating properties of the cavity.

Note that when the average energy density in the cavity is the same as in the superstrate ($\rho_n = \rho_s$), then CF is zero, i.e. there is no light concentration. Values of CF greater than zero correspond to a cavity resonance, where large, constructively interfering cavity mode fields are excited within the cavity. A concentration factor of one, for example, represents a 100% greater concentration of light in the cavity compared to the superstrate region. Negative values of CF correspond to light not actively coupling into a cavity mode, i.e. relatively *less* electromagnetic energy in the cavity than in the superstrate. The combination of a large concentration in one cavity and a small, or negative concentration factor in the other is also indicative of light splitting.

Additionally, note, that if the fractional surface area of the cavity can be decreased without decreasing the amount of energy stored in the cavity then the concentration factor increases. This directly quantizes the ability of the structures to efficiently channel light while minimizing the structure's surface area. This property, in principle, allows for a greater number of splitting cavities per unit cell, in turn, yielding the ability to construct multi-junction solar cells with the ability to capture a greater portion of the solar spectrum.

Simulated values of this quantity over a range of frequencies is shown in Fig. 8.9. The targeted resonance locations are labeled. It remains to be

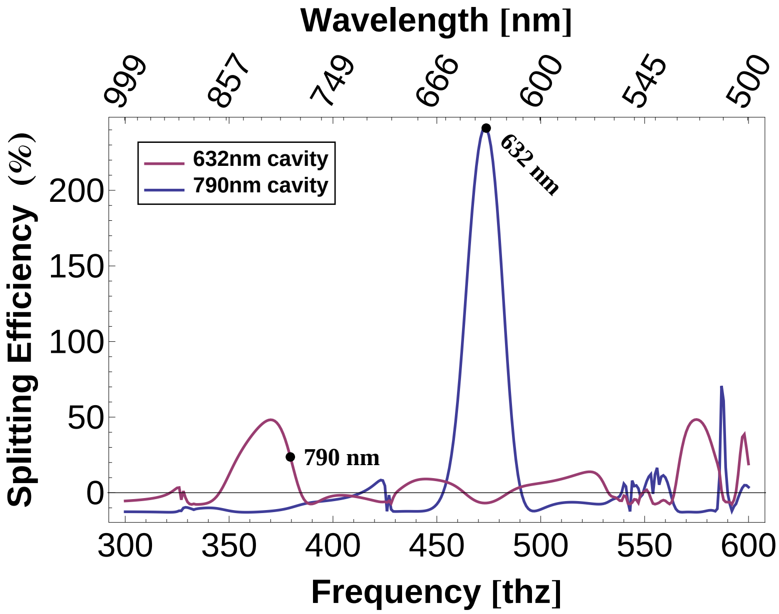

Figure 8.9: Simulated light concentration factor for both L structures for a range of frequencies. Targeted resonance locations are labeled, along with the CF peak.

understood why the concentration factor is not peaked at 790nm, where the resonance appears in the reflection analysis. Nevertheless, there is still significant light concentration at the desired wavelength. The simulated values for ρ and CF at our target frequencies are summarized in Table 8.2. Note that our structure shows very strong light concentration, with average energy densities in the cavity 23.56 (7.49) times the average superstrate energy density for 632.8 nm (790 nm) light. This corresponds to very high light concentration factors of 291.92 (50.57). Note that the negative values of CF for the cavities off-resonance acts as another illustration of the strong light

		Total Energy		Energy density		Splitting efficiency	
λ (nm)	f (THz)	E_1/E_2	E_2/E_1	ρ_1/ρ_2	ρ_2/ρ_1	E_1/E_T	E_2/E_T
632.8	473.8	387.96	0.00	644.21	0.00	99.74	0.26
790	379	0.02	42.95	0.04	25.87	2.28	97.72

Table 8.1: Total electromagnetic energy E, average energy density ρ and percent splitting efficiency SE at target wavelengths. Here, the subscript 1 corresponds to the cavity tuned to concentrate 632.8 nm light, and the subscript 2 corresponds to the cavity tuned to concentrate 790 nm light.

		Energy density		Concentration factor	
λ (nm)	f (THz)	ρ_1/ρ_s	ρ_2/ρ_s	CF_1	CF_2
632.8	473.8	23.56	0.04	291.92	-7.51
790	379	0.29	7.49	-9.19	50.57

Table 8.2: Average energy density ρ and concentration factor CF at target wavelengths. Here, the subscript 1 corresponds to the cavity tuned to concentrate 632.8 nm light, the subscript 2 corresponds to the cavity tuned to concentrate 790 nm light, and the subscript s corresponds to the superstrate.

splitting capabilities of this structure.

8.4 Results at optical frequencies

Having demonstrated that these devices are polarization independent and spatially split and concentrate light with frequency dependence with an ideal metal, we now turn to analyzing how these effects change with the introduction of real metal.

In this section we again describe rectangular and L-shaped cavities, where the resonances are chosen in the optical regime, nominally at 632nm and

790nm corresponding to two standard laser and fluorophore excitation wavelengths. These wavelengths were chosen as we initially intended to measure concentrated light splitting, however, this has not been realized experimentally. Furthermore, the resonances were not at the target wavelengths in the fabricated devices, for reasons which we will discuss.

There are four different structures which we have fabricated, simulated and tested. The first two are arrays of single rectangular cavities – a large and a small one – which display resonances but are polarization dependent in their response. The next is a compound cavity array, with both the large and small rectangles in a single unit cell. Finally, we present and comment on a double-L structure, essentially a scaled-down version of the structure discussed in the previous section.

8.4.1 Fabrication

We fabricated prototype devices using electron beam (e-beam) lithography. We begin with a bare, 4-inch single-side polished Si wafer. The wafer is cleaned with hot piranha etch (a mixture of sulfuric acid and hydrogen peroxide). A conductive seed layer, consisting of a 5 nm titanium adhesion layer followed by 100 nm of gold, is deposited using a electron gun evaporator. Next, a 300 nm thick NEB-31A3 e-beam resist is spun on top of the seed layer. The pattern is exposed with a dose of 35-40 C/cm^2. Figure 8.10(a) shows a scanning electron microscope (SEM) image the developed pattern in the resist.

The surface is mildly de-scummed in downstream plasma, and gold is plated around the resist features using pulse-plating in a non-cyanide electroplating solution. The gold thickness is measured at around 260 nm. Figures 8.10(b) and 8.10(c) show the surface after electroplating. The cavities are now defined by the L-shape of the resist. The resist is then stripped in acetone with the help of ultra-sonication followed by a short oxygen plasma de-scum. Figure 8.10(d) shows a top down view of a final resulting device.

Several shapes besides the L-shaped cavities have been fabricated in order to characterize the operation of the cavity structures in general, including one and two rectangular structures, as well as single L-shaped cavities per unit cell, as shown in Fig. 8.11. We will discuss the single and double rectangle apertures and the double L-shaped apertures.

8.4.2 Measurement and simulation results

The aggregate optical response of different structures (e.g. size, shape) is noticeably different, see Fig. 8.12. This apparent color difference is due to the frequency-dependence of the optical response. Others have also noted

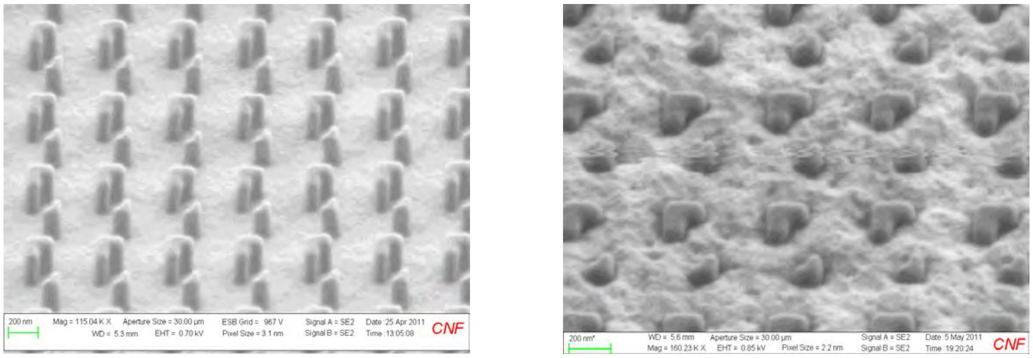

(a) SEM of the apertures patterned in e-beam resist.

(b) SEM of the surface after gold plating. At this step, the L-shaped resist is surrounded by metal, both on the sides and below.

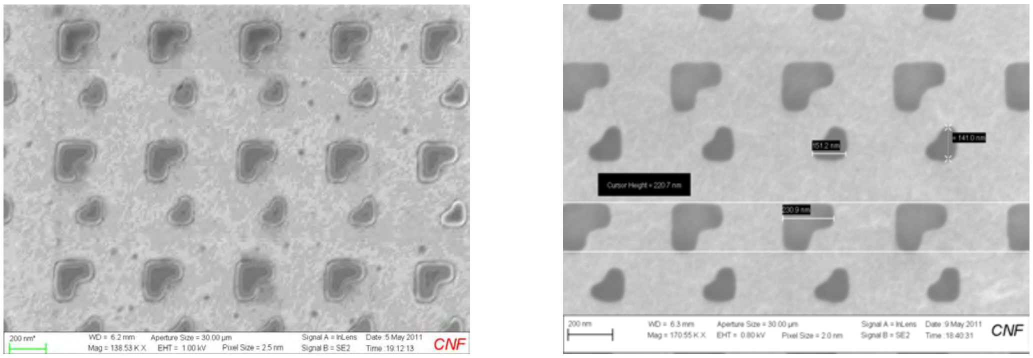

(c) Top down SEM of the surface after plating.

(d) SEM image of the final device after resist stripping.

Figure 8.10: The results of the fabrication process for making the L-shaped metamaterial.

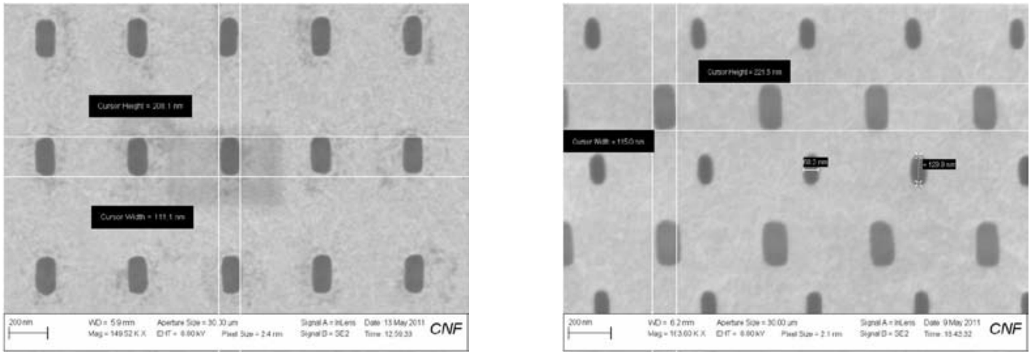

(a) One rectangle per unit cell.

(b) Two rectangles per unit cell.

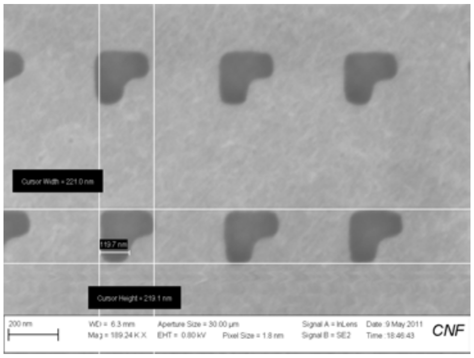

(c) One L per unit cell.

Figure 8.11: Assorted permutations of fabricated metamaterials.

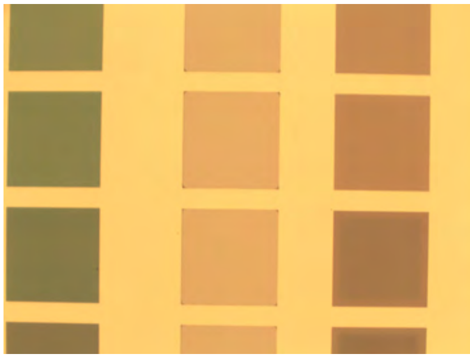

Figure 8.12: Optical microscope image of patches of different-sized and shaped cavities set in gold. The difference in optical response (green to reddish color) is due to the different cavity shapes and dimensions.

that the nanostructure of a metal film plays a large role in the apparent color of a metal film.[110] To quantify this response, we directly measured the frequency-dependent reflection response. Reflection measurements on these devices were carried out on a Newport Oriel MS 257 monochromator and imaging spectrograph. The patterned wafers were first treated in a hydroxy thiol solution, and then immersed in deionized water. The measurements are all of specular reflection, normalized with respect to the reflection of a un-patterned, gold coated silicon wafer.

Rectangular cavities

As discussed in Section 8.2.1, rectangular apertures are polarization sensitive. This applies to visible frequencies, as well. Figure 8.13 shows experimental and simulated specular reflection from arrays of rectangular cavities, which illustrates this property. Here, H polarization is along the short side of the cavities. We have labeled the cavity modes (CM) and diffracted modes (DM). There is decent agreement between the simulation and the measured results; any substantial differences are due to imperfections in the fabricated sample. That is, there is corner rounding, as seen in Fig. 8.11, and some variation in cavity sizes – both of which are not relevant in simulation – which shifts the cavity mode resonance.

The optical response of the compound structure, with both a large and the small cavity in each unit cell, is largely the sum of the response of the individual structures. Figure 8.14 shows a plot of experimental reflection from individual cavity arrays, as well as arrays with both cavities in a unit cell. The independence of each resonance is thus demonstrated, as there is negligible shifting of the resonances when both cavities are present.

L-shaped cavities

As discussed in Section 8.2.1, L-shaped structures are polarization independent. This applies to visible frequencies, as well, at least in simulation. Figure 8.15 shows experimental and simulated specular reflection from arrays of L-shaped cavities. The simulated response of the nominal design is largely polarization independent, as with the PEC case. However, the experimental

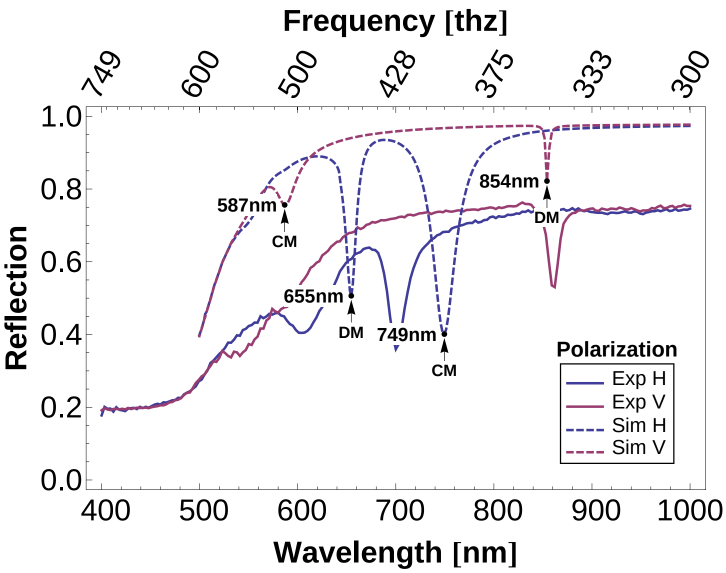

(a) Array of smaller rectangles.

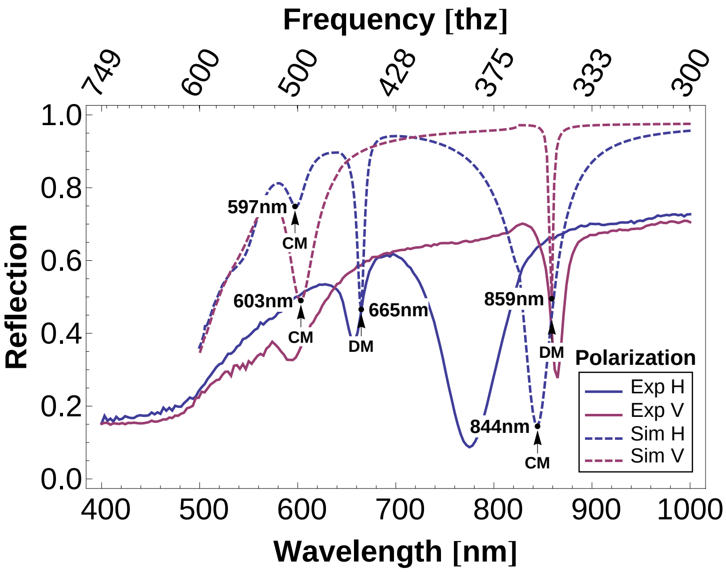

(b) Array of larger rectangles.

Figure 8.13: Frequency-dependent experimental (Exp) and simulated (Sim) reflection from arrays of rectangular cavities in gold immersed in water. H polarization is along the short side of the cavities. Cavity modes (CM) and diffraction modes (DM) are labeled.

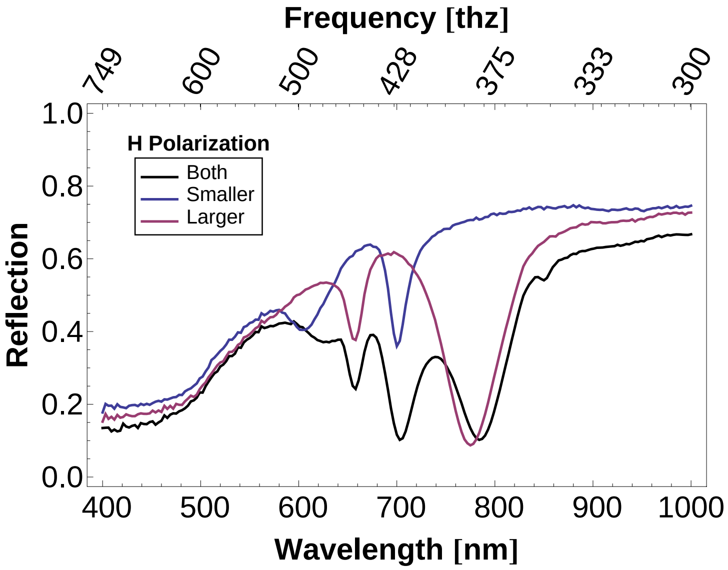

(a) Polarization along short side.

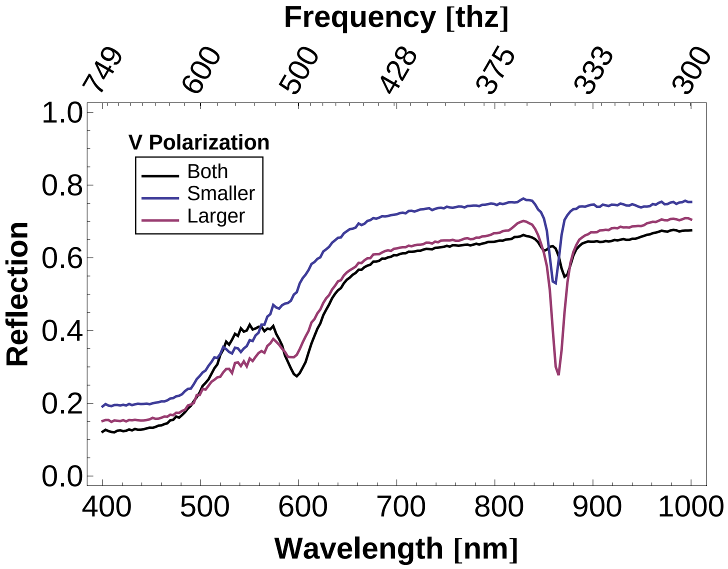

(b) Polarization along long side.

Figure 8.14: Frequency-dependent experimental reflection from arrays of individual (colored) and compound (black) rectangular cavities in gold. H polarization is along the short side of the cavities.

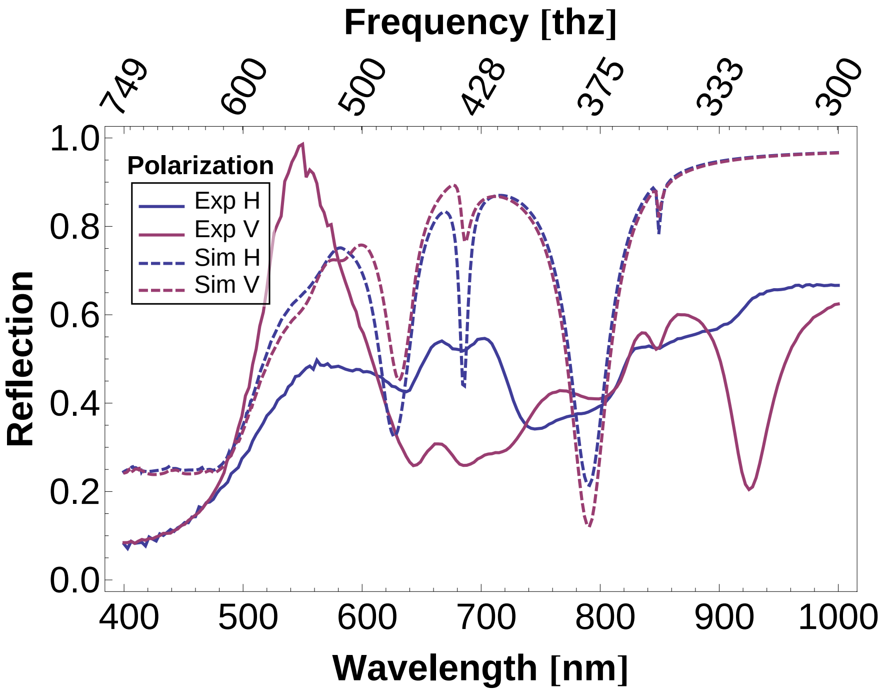

Figure 8.15: Frequency-dependent experimental (Exp) and simulated (Sim) reflection from arrays of L-shaped cavities in gold. This structure has two cavities per unit cell.

results, although vaguely reminiscent of the simulated values, are far from being polarization independent. The reason for this discrepancy is likely the misshapen L's that were realized in fabrication, see Fig. 8.10(d). As with the rectangles, the sharp edges and corners are rounded, yet the effect is greater in the more-complicated L-shaped cavities.

Rounding the corners of the L-shapes shifts the resonances towards longer wavelengths, see Fig. 8.16(a). Additionally, the structure begins to demonstrate different responses at different polarizations. While rounding the corners accounts for some features seen in the experimental measurements, it does not account for all of the features, see Fig. 8.16(b). Furthermore, unlike the rectangular cavities (Fig. 8.14), the response of the compound array with two L-shaped cavities is not the sum of the response of the individual structures, see Fig. 8.17. While it is difficult to fully explain all these discrepancies, a likely cause of some is the degree to which water actually penetrates into the cavities. If the cavities are not uniformly filled, or fill differently with different patterns, the optical response changes accordingly. It is not possible to simulate these more complicated situations with current computational resources; this question remains open for further analysis.

8.5 Conclusions and outlook

We have demonstrated the potential capability of L-shaped cavity metamaterials to both split and concentrate light, with high efficiency and concentrations. This response is mostly independent of the polarization of incident light under ideal, PEC conditions. These results do show some field coupling between cavities; other positions or orientations of the cavities with a unit cell (e.g. 45° rotation of one L structure) may decrease these effects, leading to complete polarization independence in the cavity response. Additionally, these structures have potential applications in polarization controlling meta-

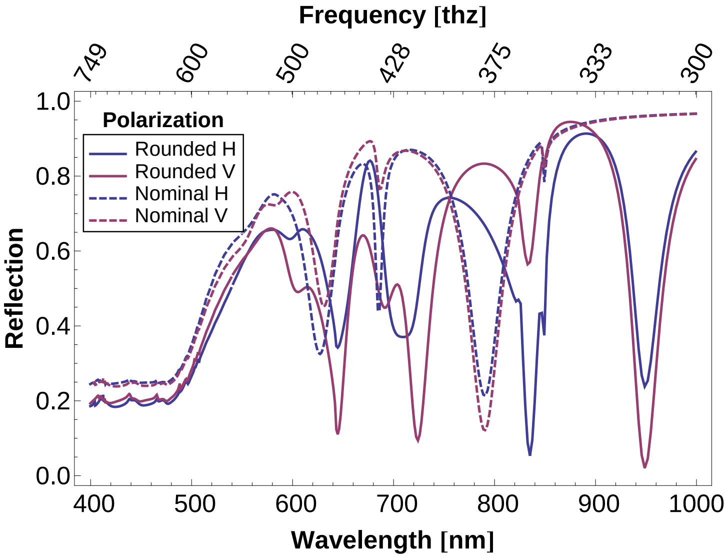

(a) Simulated specular reflection from arrays of nominal and rounded-corner L-shaped cavities in gold.

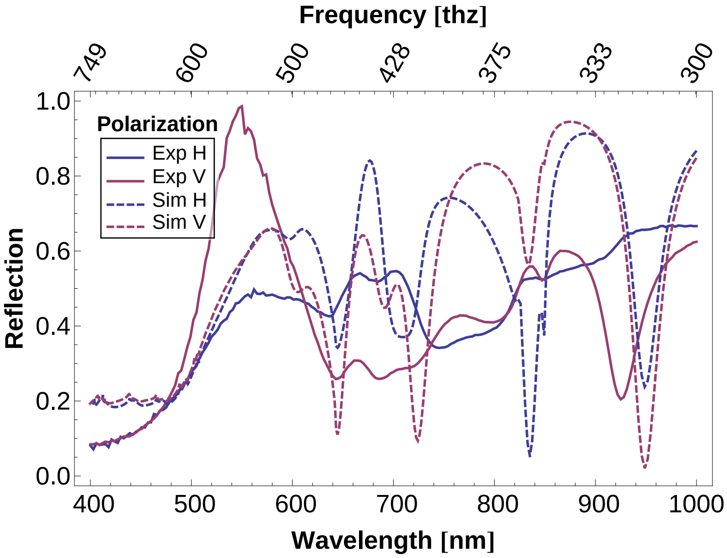

(b) Experimental and simulated specular reflection from arrays of rounded-corner L-shaped cavities in gold.

Figure 8.16: Frequency-dependent simulated and experimental specular reflection from arrays of rounded-corner L-shaped cavities is plotted in (b). The nominal and rounded-corner structure are compared in (a).

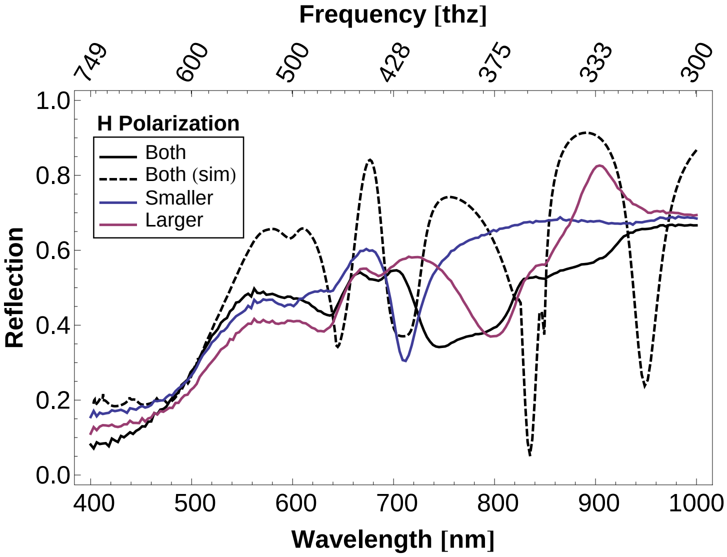

(a) H polarization.

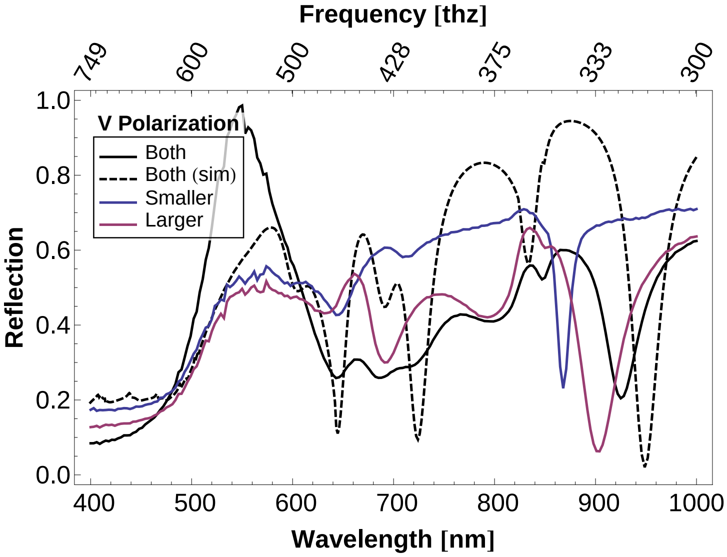

(b) V polarization.

Figure 8.17: Frequency-dependent experimental and simulated (black dashed) reflection from arrays of individual (colored dashed) and compound (black solid) and L-shaped cavities in gold.

materials, or possibly for non-reciprocal structures.

We computationally modeled, fabricated, and experimentally verified the polarization-dependent reflection response of rectangular nanostructures. Furthermore, we have shown experimentally how the resonances of arrays of single cavities of different sizes are independent, such that the response of a compound array matches the summed response of the individual arrays. Although we had promising predictions of polarization independence with L-shaped structures at optical frequencies from simulation, these were not realized experimentally due to the constraints of fabrication.

The L-shaped structures are made at the limits of this fabrication method. It is possible to simulate C-shaped structures with varying radii of curvature as a better model of fabricated devices, but they would be difficult to fabricate with consistent and controllable dimensions. Thus, despite some promising results, L-shaped structures are not an ideal candidate for a polarization independent, light splitting structure for solar energy applications. However, as we discuss in the next chapter, cylindrical cavities do not share all these difficulties.

Chapter 9

Cylindrical cavity arrays

9.1 Introduction

In this chapter we discuss the design, fabrication, and experimental characterization of a metamaterial which demonstrates light localization, photon sorting, and enhanced absorption at microwave frequencies. As in the previous chapter, the material is a compound subwavelength cavity array, here consisting of multiple cylindrical cavities. The device spatially splits incoming microwave radiation into two spectral ranges, individually channeling the separate spectral bands to different cavities within each spatially repeating unit cell.

Further, the target spectral bands are absorbed within each associated set of cavities. The photon sorting mechanism, the design methodology, and experimental methods used are all described. A spectral splitting efficiency of 93-96% and absorption of 91-92% at the two spectral bands is obtained for the structure. This corresponds to an absorption enhancement over 600% as compared to the absorption in the same thickness of absorbing material.

We fabricate and experimentally measure the reflection response of this structure. Furthermore, we probe some near-field effects at resonance to experimentally verify the photon sorting. Both the reflection and estimated efficiencies from the experimental measurements are comparable to the simulated values.

We also discuss the path towards the application of these concepts to the optical spectrum. Unlike the complicated L-shaped structures of Chapter 8, which required unattainable sharp edges and corners to maintain the desired effect, cylindrical cavities can be fabricated in a controlled manner with very small radii. Furthermore, the existence of transparent, high dielectrics in the optical regime allows multiple cavities per unit cell, while maintaining a small-enough periodicity to minimize the detrimental effects of diffraction.

9.2 Metamaterial design

The structure discussed in this chapter is a two-dimensional square array of subwavelength cylindrical cavities embedded in aluminum. Each unit cell contains two cavities of different radii, a_1 and a_2, and identical heights, h,

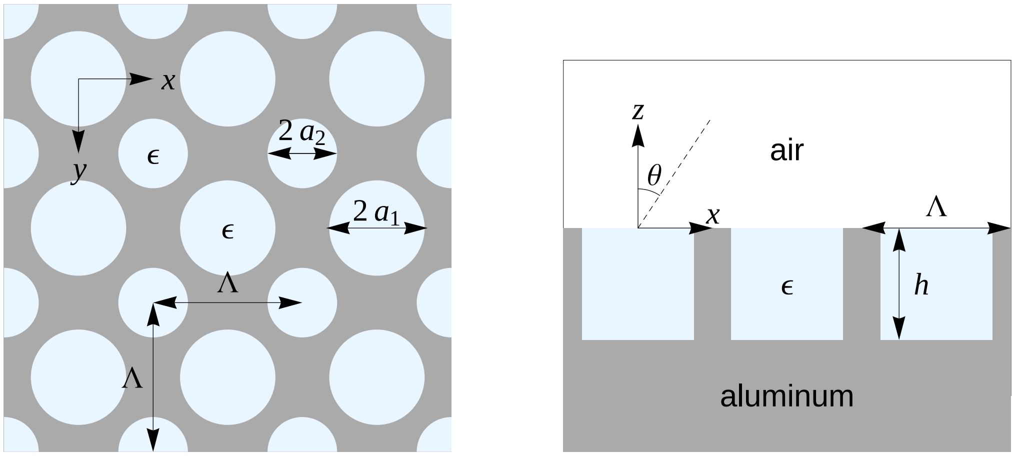

(a) A top-down view of the structure under consideration.

(b) A cross section view of the structure under consideration.

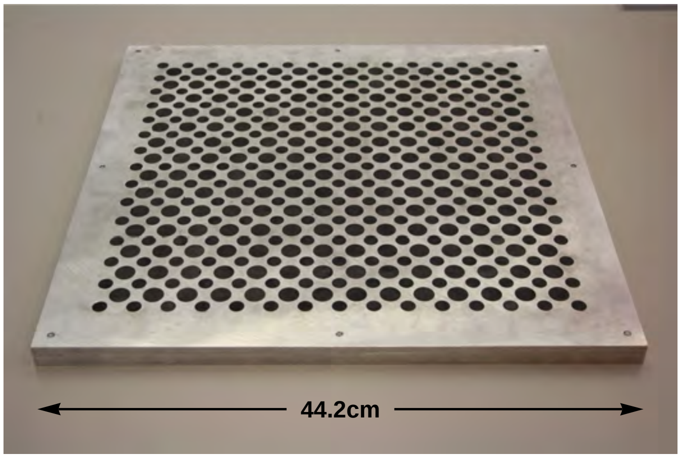

(c) The final fabricated device.

Figure 9.1: A schematic of periodic cylindrical cavities in a metal is shown from top down (a), in a cross section through one set of cavities (b), and the final fabricated device (c). The gray region represents the metal, the light blue regions are the dielectric-filled apertures, and the white is the superstrate (air) above the cavities. Here $\Lambda = 26$ mm, $a_1 = 8.03$ mm, $a_2 = 5.74$ mm, $h = 7$ mm, and θ is the angle of incidence.

arranged in a rhombic lattice, see Fig. 9.1. The individual cavities within the unit cell are designed to support an effective cavity resonance or cavity mode (CM) with amplified electromagnetic fields, where the lowest order mode's frequency dependence is given by Eq. 4.10. Thus, the structure's resonance response is tuned by adjusting the radii a_n and heights, of the cavities, and the periodicity, Λ of the array. The two individual-cavity periodic structures are then combined, placing two cavities within one unit cell and their dimensions are optimized to maximize photon sorting and absorption, and to minimize coupled cavity effects that can occur within cavity arrays of this sort.

Because the purpose of the device is to absorb the spectrally-sort photons, an absorbing material is placed within the cavities; this material is an absorbing silicone elastomer dielectric (Sylgard 184), doped with graphite (which is responsible for the absorption), whose dielectric value, ϵ, can be adjusting by controlling the concentration of graphite inside the material, see Fig. 9.2.

It is important to note that as the dielectric loss tangent (ϵ''/ϵ') of the material increases, the resonances broaden, essentially overdamping the CM resonance. By choosing a lower graphite concentration we are able to maximize the absorption and maintain independent cavity resonances. We found

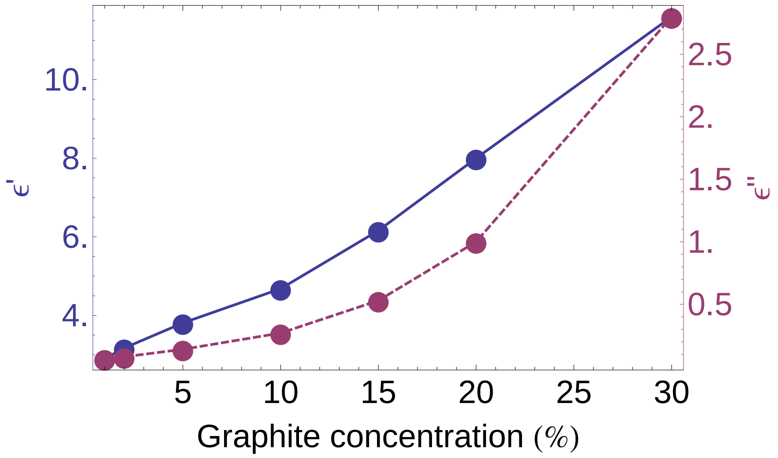

Figure 9.2: Variation in the silicone elastomer complex dielectric permittivity ϵ at 9 GHz as a function of graphite concentration. Blue-solid (red-dashed) curve is the real (imaginary) portion of ϵ.

that a graphite concentration of 8.36%, which gives a complex dielectric permittivity of $\epsilon = 4.33 + 0.22i$ was able to absorb the maximum quantity of incident power, while still maintaining clearly defined resonances, see Fig. 9.3. Optimum coupling occurs when the probability of radiative decay (i.e. lifetime of the mode) is equal to that of nonradiative decay. Our result was found numerically, and future study is required to develop a complete analytical model of this effect.

The goal of this device was to have two absorption peaks that are well separated with respect to each other, while maintaining absorption peaks with as large of a bandwidth as possible for each peak. The target frequencies of the absorption peaks were chosen to be below the onset of far-field

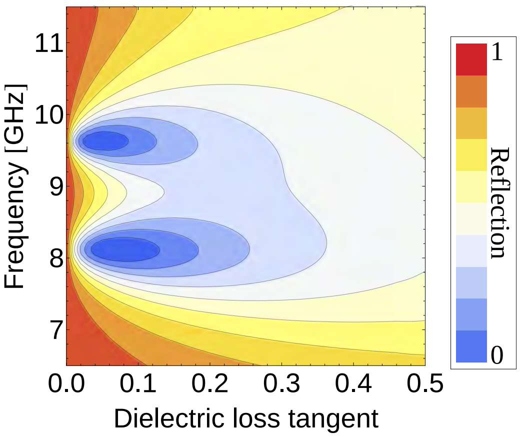

Figure 9.3: Variation in resonance properties of a dual-cavity structure as a function of the dielectric loss tangent in the silicone elastomer dielectric. Too small of a loss tangent will not provide enough absorption; too large a loss tangent will overdamp the resonances and ruin the enhanced absorption.

diffraction, as these diffraction modes carry energy away from the material surface, and thus compete with the CMs for the energy of the incident beam. This competition between back-scattered far-field diffracted modes and CMs imposes an important constraint on the design that ultimately limits the number of different cavities that can fit within one unit cell.

9.2.1 Simulation

Once the preliminary design was obtained using Eq. 4.10, the device was further optimized and analyzed using HFSS. With HFSS, the structures were simulated using periodic boundary conditions in the transverse directions and a Floquet port for the incident beam. We simulated the metal using the aluminum material parameters from the HFSS library with a surface boundary condition, and used the experimentally determined dielectric properties for the elastomer. It is important to note that there is some degree of uncertainty in the measurements of dielectric constants, which can cause a substantial deviation from the results of simulations.

The resonant properties of the cavity modes can be analyzed using direct and indirect methods, see Section 6.2.2. In the direct method, the volume loss density (i.e. the fraction of incident energy absorbed in a particular region) derived from the solved electromagnetic fields can be directly integrated over the volume of each of the cavities. At cavity resonance this quantity will exhibit a maximum. Off resonance, the field in the cavities are not excited and the total volume loss will be minimized. To calculate the photon sorting efficiency, SE_n, we use the ratio of total electromagnetic energy absorbed in the desired cavity E_n to the total energy absorbed by both cavities, $E_T = E_1 + E_2$

$$SE_n \equiv \frac{E_n}{E_T}, \tag{9.1}$$

i.e. the fraction of absorbed energy that was correctly split. This is a similar expression to Eq. 8.5, however here we use the calculated absorption, rather than the electromagnetic energy.

Alternatively, the cavity resonances can be determined indirectly from the reflection intensity. In the absence of absorbing materials, the total reflection remains essentially constant, decreasing slightly due to small amounts of surface loss at the metal surfaces. However, with absorption, we can characterize a resonance in frequency-space by a dip in reflection intensity. In practice, we utilize the simulated S-parameters to determine the reflection. This metric is useful for a simple comparison to experimental measurements, however it does not, by itself, determine where, spatially, in a structure the absorption occurs.

9.2.2 Fabrication and measurement

The fabrication and measurement of this device was done by Ian K. Hooper at the Electromagnetics Materials Laboratory at the University of Exeter. An Anritsu M4640A vector network analyzer (VNA) was used to record the measured complex S-parameters of the graphite loaded elastomers in an 8-12 GHz waveguide. The dielectric properties of the elastomer composites were subsequently extracted using the Nicholson-Ross-Weir algorithm.[111, 112] An aluminum plate was machined by CNC to the requisite design, and preformed tablets of the selected elastomer composite were inserted into the cavities.

To take reflection measurements, the sample was surrounded by pyrami-

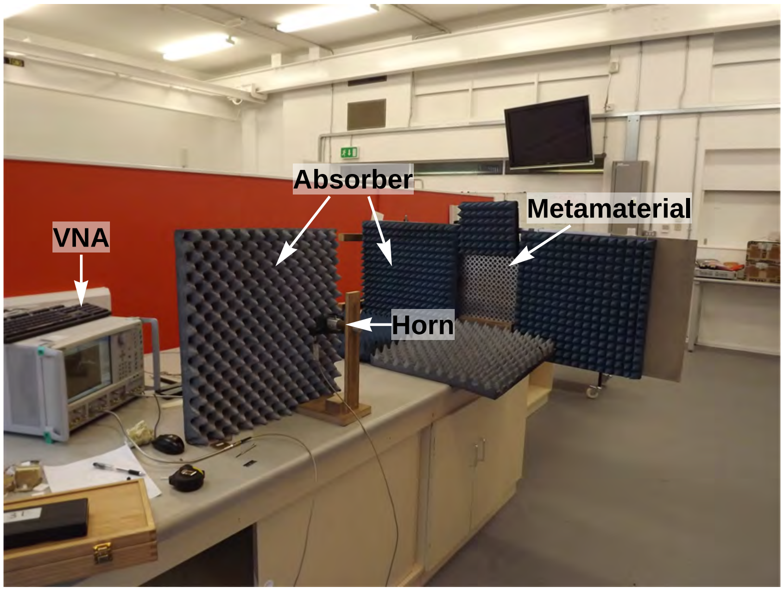

Figure 9.4: Experimental setup for measuring reflection response from the metamaterial. There is another horn on the other side of the leftmost pyramidal absorber sheet.

dal absorbers to limit scattering and the free-space p- and s-polarized reflectivity of the sample was measured using the VNA with broadband horns between frequencies of 7.5 and 15.0 GHz, for angles of incidence between 5 and 35 degrees, see Fig. 9.4.

The field profiles were measured using the VNA with a broadband horn for excitation above the metamaterial, see Fig. 9.5(a), with a local probing antenna consisting of an exposed section of coaxial cable aligned along the polarization direction, see Fig. 9.5(b). The probe antenna was computer controlled by a three-axis translation stage, which allowed us to measure the

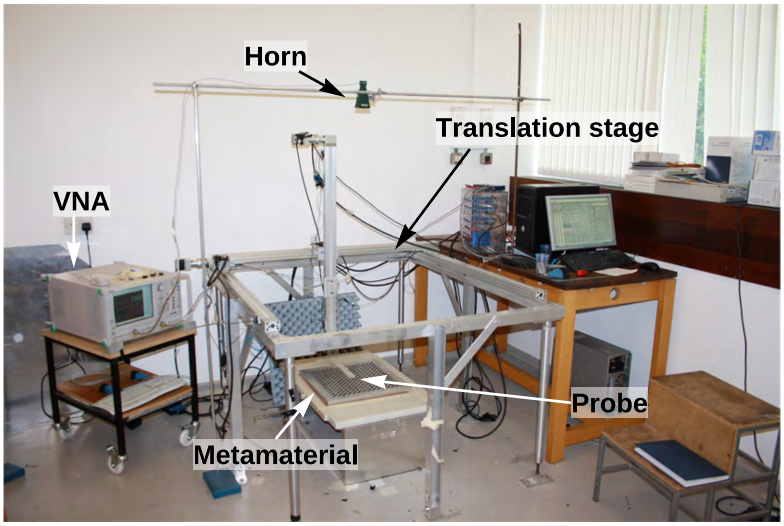

(a) The complete field profile setup.

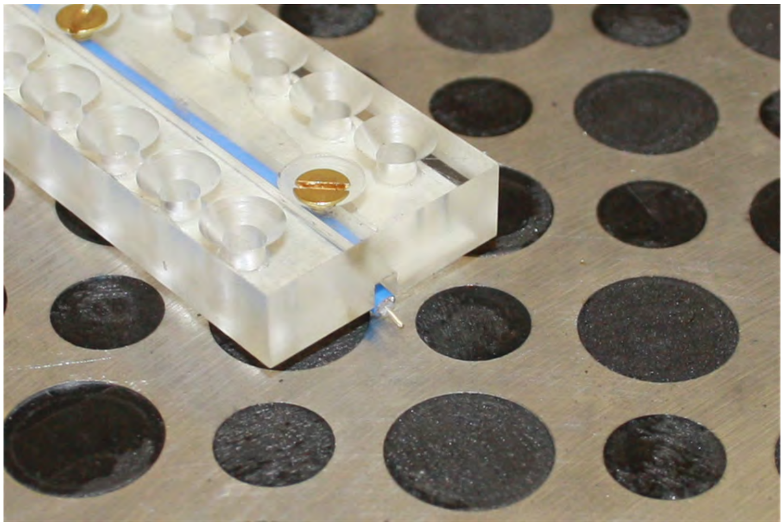

(b) The local probing antenna.

Figure 9.5: Experimental setup for measuring the spatial dependence of the electric field strength.

spatial dependence of the fields.

9.3 Results

9.3.1 Optimized structures

Two-band structure

After the simulation process described earlier, we developed an optimal structure. This was based on the measured dielectric properties (Fig. 9.2) and the CNC machine's fabrication limitations. Taking these considerations into account, the optimal simulated device has a periodicity of $\Lambda = 25.96$ mm, and the two cavities with identical heights of $h = 7.07$ mm, but different radii of $a_1 = 7.99$ mm and $a_2 = 5.83$ mm. This device resonates at frequencies of 8.1 GHz and 9.6 GHz. Fig. 9.6(a) shows a plot of the total reflection from this structure as a function of frequency under one polarization. There is a tiny absolute difference in the reflection response between polarizations no greater than 1%, see Fig. 9.6(b).

This device absorbs 96% (93%) of incident radiation at 8.1 GHz (9.6 GHz), with a splitting efficiency (Eq. 9.1) of 99% (95%). That is, the fields are channeled to and into smaller (larger) of the two cavities, where the resonant fields are strongly, and locally absorbed. These results are summarized in Table 9.1. This device was the nominal structure we fabricated and tested.

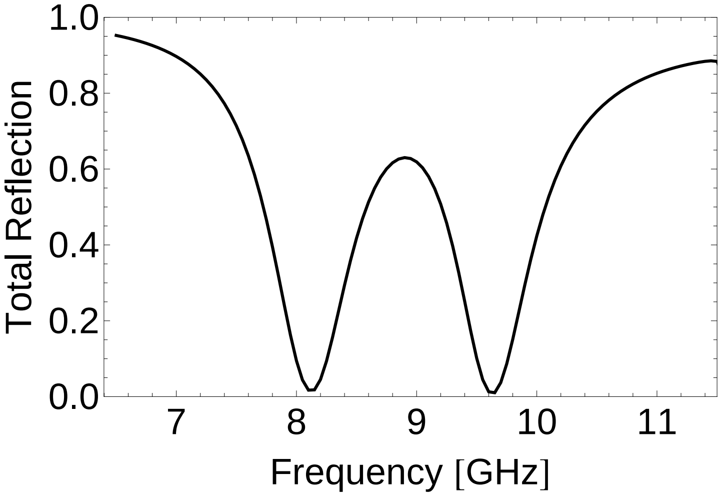

(a) Total simulated reflection from the optimized structure.

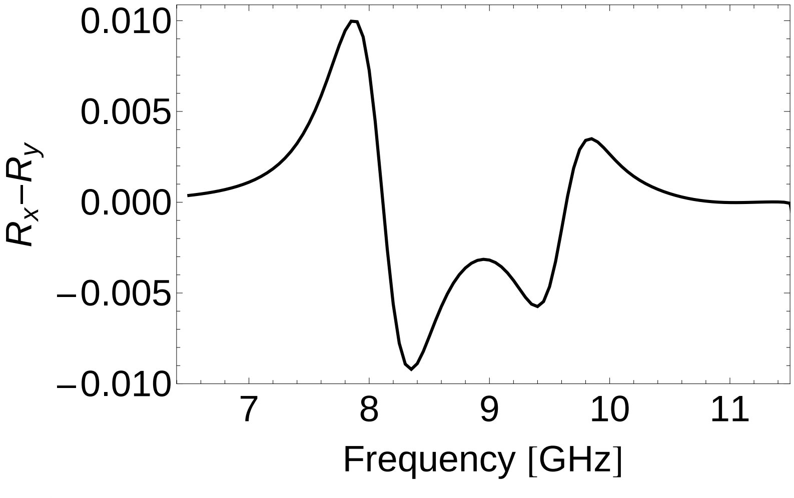

(b) Difference between simulated reflection under different polarizations.

Figure 9.6: Simulated reflection from an optimal two-band photon sorting structure.

	Absolute absorption (%)		Splitting efficiency (%)	
Frequency (GHz)	E_1	E_2	E_1/E_T	E_2/E_T
8.1	96	1	99	1
9.6	5	93	5	95

Table 9.1: Percentage of the total electromagnetic energy absorbed E and fractional splitting efficiency SE at target frequencies in an optimized two-band structure. Here, the subscript 1 (2) corresponds to the cavity tuned to concentrate 8.1 GHz (9.6 GHz) radiation. Note that the absolute absorption numbers do not sum to 100%, as there is some reflected radiation.

Three-band structure

To make a three-band structure, with three independent resonances, we started with the preceding two-band structure, and added a third hole, see Fig. 9.7. Then, we used HFSS's optimizer to improve on the initial structure. The optimal simulated device has a periodicity of $\Lambda = 24.75$ mm, and the three cavities with identical heights of $h = 8.01$ mm, but different radii of $a_1 = 7.25$ mm, $a_2 = 5.45$ mm, and $a_3 = 4.5$ mm. In this structure, the dielectric in the cavities is $\epsilon = 4.46 + 0.05i$. This device resonates at frequencies of 8.05 GHz, 9.6 GHz, and 11.25 GHz. Fig. 9.8(a) shows a plot of the total reflection from this structure as a function of frequency under one polarization. As with the two band structure, there is a small absolute difference in the reflection response between polarizations, here no greater than 0.6%, see Fig. 9.8(b).

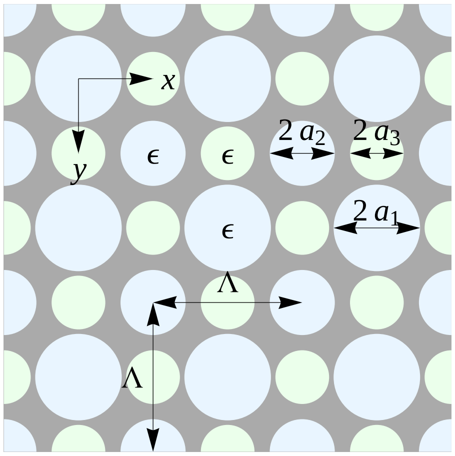

Figure 9.7: A top-down view of the three-band light splitting structure. New cavities are highlighted in green.

This device absorbs 93% (82%) [82%] of incident radiation at 8.05 GHz (9.6 GHz) [11.25 GHz], with a splitting efficiency of 97% (90%) [93%]. That is, the fields are channeled to and into the appropriate cavity, where the resonant fields are strongly, and locally absorbed. These results are summarized in Table 9.2. Although this demonstration is for microwave structures, it shows that polarization independent photon sorting is, in principle, possible with three bands, thus increasing the potential efficiency of a multi-junction device based on this approach.

9.3.2 Experimental results

The fabricated device has a periodicity of $\Lambda = 26$ mm, and the two cavities with identical heights of $h = 7$ mm, but different radii of $a_1 = 8.03$ mm and

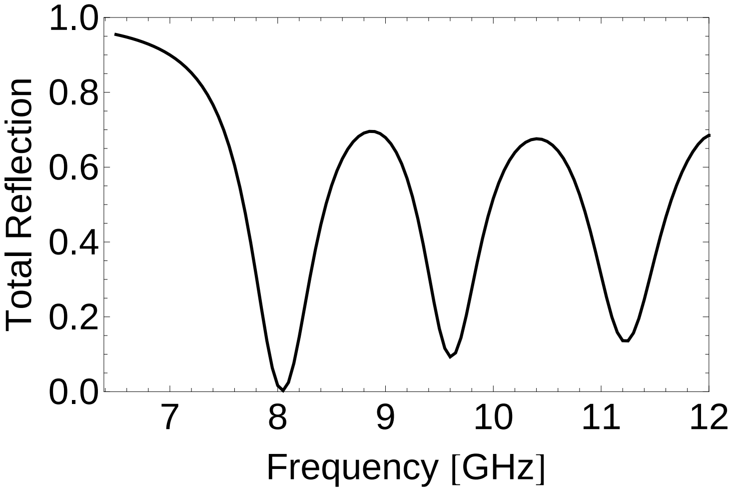

(a) Total simulated reflection from the optimized structure.

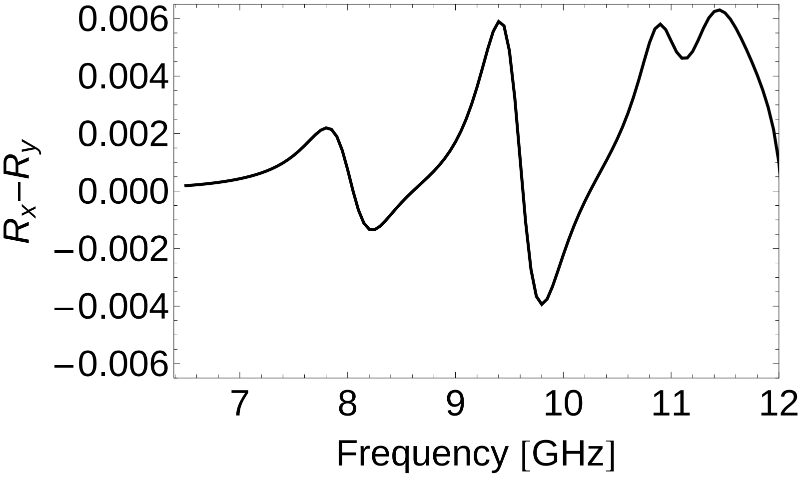

(b) Difference between simulated reflection under different polarizations.

Figure 9.8: Simulated reflection from an optimal photon sorting structure.

	Absolute absorption (%)			Splitting efficiency (%)		
Frequency (GHz)	E_1	E_2	E_3	E_1/E_T	E_2/E_T	E_3/E_T
8.05	93	2	1	97	2	1
9.6	6	82	3	6	90	3
11.25	3	3	82	3	4	93

Table 9.2: Percentage of the total electromagnetic energy absorbed E and fractional splitting efficiency SE at target frequencies in an optimized three-band structure. Here, the subscript 1 (2) [3] corresponds to the cavity tuned to concentrate 8.05 GHz (9.6 GHz) [11.25 GHz] radiation. Note that the absolute absorption numbers do not sum to 100%, as there is some reflected radiation.

$a_2 = 5.74$ mm, slightly different than the optimal structure. It resonates at frequencies of 8.10 GHz and 9.25 GHz. Fig. 9.9 shows the simulated and measured reflection intensity of s-polarized microwave radiation specularly reflected from the material surface at an angle of incidence $\theta = 17$ degrees. There is strong agreement between the simulated and experimental results.

There are two likely sources of error in the experiment as compared to the optimal simulation. First of all, the pre-formed tablets of the elastomer composite fit with different amounts of tightness in the large and small holes, thus leading to a slight dielectric mismatch between the two cavities. Additionally, the elastomer was squeezed into the smaller hole, leading to a small amount of elastomer sticking out above the top of the cavities. Any discrepancies between simulated and experimental results have been accounted for

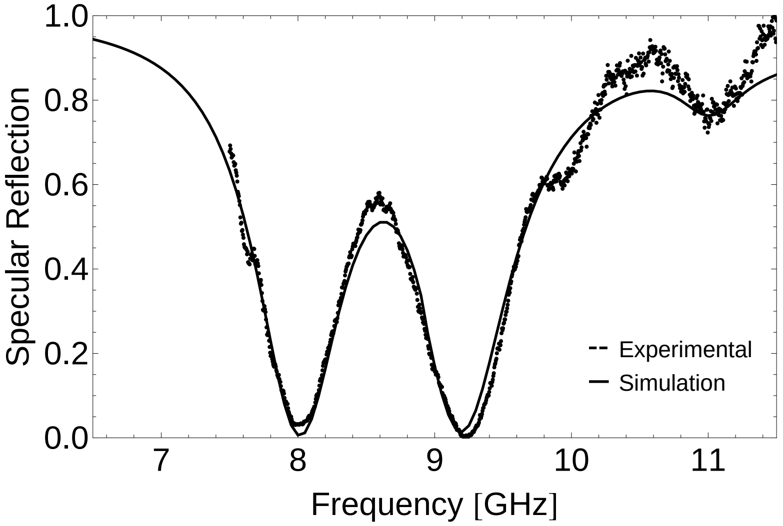

Figure 9.9: Experimental and simulated specular reflection intensity from the material surface for s-polarized radiation at $\theta = 17°$ angle of incidence. The two dips in reflection intensity correspond to the two cavity resonances.

by adjusting these two parameters in simulation within a reasonable range.

We have also studied the dependence of these results on angle of incidence; it is difficult to measure the reflection from this structure for normal incidence. For radiation that is p-polarized, there is a variation in the reflection (and thus, absorption) as a function of angle of incidence, see Fig. 9.10(a). This is caused by the changes in the properties of evanescent fields above the cavities in this polarization, which extends the effective height in Eq. 4.8 and decreases the resonant frequency. However, in the s-polarization, where the evanescent fields are largely unaffected, there is negligible variation over a broad range of angles, see Fig. 9.10(b). At normal incidence the absorption response of this structure is polarization independent, and for shallow angles ($< 20°$) the response is largely polarization independent. Here, as well, there is strong agreement between simulated values and experimental results, with the differences accounted for by considering variation in material parameters.

Absorption enhancement and photon sorting

These results show that the expected photon sorting and absorption is occurring as the theory and modeling predicts. Namely, as 8.1 GHz (9.25 GHz) radiation approaches the structure from above a unit cell, 91% (92%) of the incident energy is absorbed by the structure. The absorption enhancement can be calculated by normalizing the absorption with respect to the fractional surface area,

$$S_n = \Lambda^2/(\pi a_n^2), \tag{9.2}$$

of each cavity, which is a standard metric used with enhanced optical transmission.[17] This corresponds to an enhanced absorption of 303% (600%) at 8.1 GHz (9.25 GHz). Another way of calculating the enhanced efficiency of this device is to compare it to the absorption E_s in a 7 mm thick slab of the absorbing dielectric that fills the cavities. This metric gives a enhanced absorption of 610% (452%).

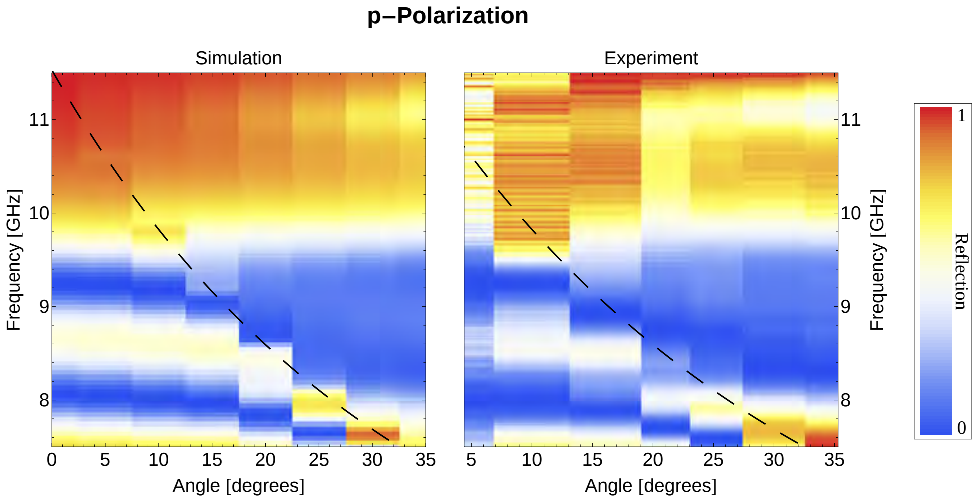

(a) Specular reflection from the material for a p-polarized incident beam. The dashed line shows the onset of diffraction.

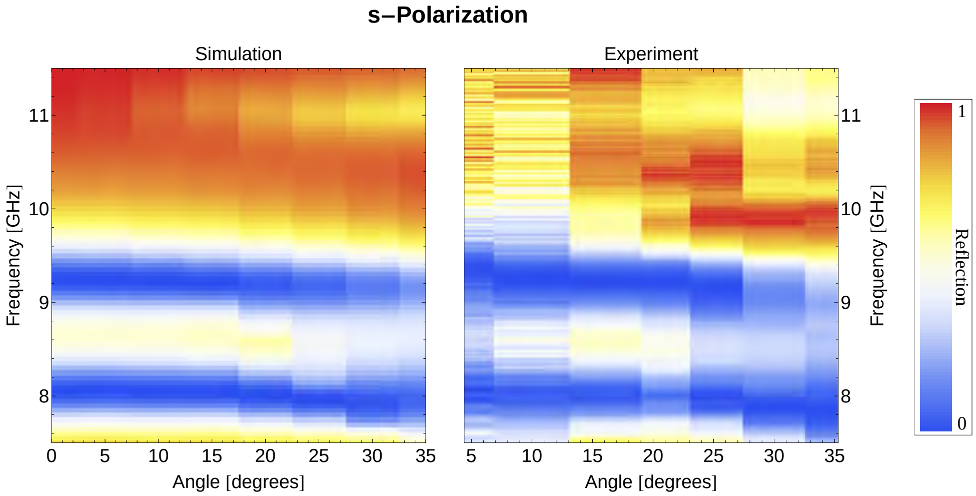

(b) Specular reflection from the material for a s-polarized incident beam.

Figure 9.10: The reflection from the material for both s- and p-polarizations. Simulated results shown on the left, with experimental results on the right. For shallow angles, the reflection response varies only slightly.

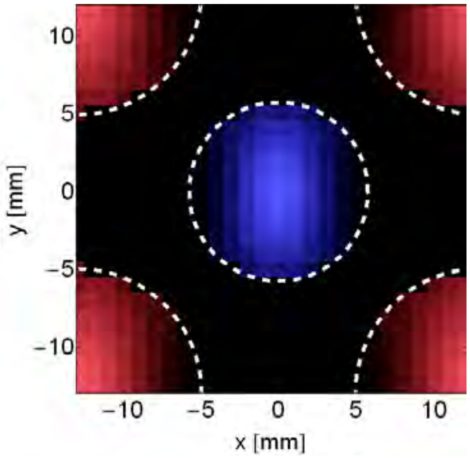

Figure 9.11: Pseudo-color plot of the simulated volume loss density at a height of 3.5 mm inside the cavities at the two frequencies. The red (blue) color corresponds to the 8.1 GHz (9.25 GHz) resonances, which are overlayed to see the photon sorting. The dashed circles are the edges of the cavities.

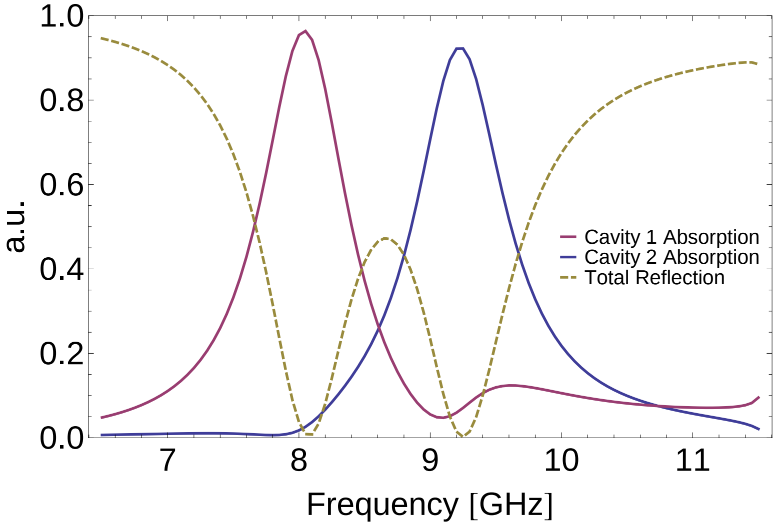

Figure 9.12: Simulated total reflection intensity from the material surface for normal incidence compared to energy absorption inside each cavity. The two dips in reflection intensity correspond to the two maxima in cavity absorptions.

There is a very high spatial selectively to the absorption response at the different resonances. Figure 9.11 is a pseudo-color plot of the volume loss density in a cut-plane midway through the cavities; the spatially localized nature of the absorption is readily seen. Additionally, the two dips in reflection intensity correspond to maxima in the integrated volume loss density within the two separate cavities, see Figure 9.12. That is, the fields are channeled to and into smaller (larger) of the two cavities, where the resonant fields are strongly, and locally absorbed. To calculate the photon sorting efficiency, SE_n, we use Eq. 8.5, which gives the ratio of total electromagnetic energy absorbed in the desired cavity E_n to the total energy absorbed by both cavities, $E_T = E_1 + E_2$, i.e. the fraction of absorbed energy that was correctly split. At each resonance the absorption is highly localized within the cavity tuned for that resonance. This structure has a simulated splitting efficiency of 96% (93%). These results are summarized in Table 9.3.

We were also able to experimentally verify that this device spatially splits the incident photons. Figure 9.13 shows a pseudo-color plot of the electric field component along the polarization direction, measured 1 mm above the metamaterial surface. The red (blue) color corresponds to the magnitude of this field at the 8.1 GHz (9.25 GHz) resonances, which are overlayed to see the photon sorting. The dashed circles are the approximate edges of

	Absolute absorption (%)		Enhanced absorption (%)		Splitting efficiency (%)	
Frequency (GHz)	E_1	E_2	S_nE_n	E_n/E_s	E_1/E_T	E_2/E_T
8.1	91	4	303	610	96	4
9.25	7	92	600	452	7	93

Table 9.3: Percentage of the total electromagnetic energy absorbed E, enhanced absorption of the structure, and fractional splitting efficiency SE at target frequencies in the fabricated structure, calculated from simulation. Here, the subscript 1 (2) corresponds to the cavity tuned to concentrate 8.1 GHz (9.25 GHz) radiation. Note that the absolute absorption numbers do not sum to 100%, as there is some reflected radiation.

the cavities below. This figure demonstrates that, at each resonance, the fields are predominantly isolated in the regions immediately above the target cavities. It is this light channeling property of the device that which leads to the enhanced absorption. Note, that the vertically-oriented “stripes” of blue between the larger apertures are artifacts of the measurement, likely caused by scattering from the probe wire. This is supported by the fact that rotating the sample does not change the orientation of the stripes, while rotating the source and probe rotates these lines.

We can use the measured field strength F just above the surface of the metamaterial to calculate an approximate splitting efficiency. Instead of calculating the ratio of energy absorbed in each cavity, we can use the ratio

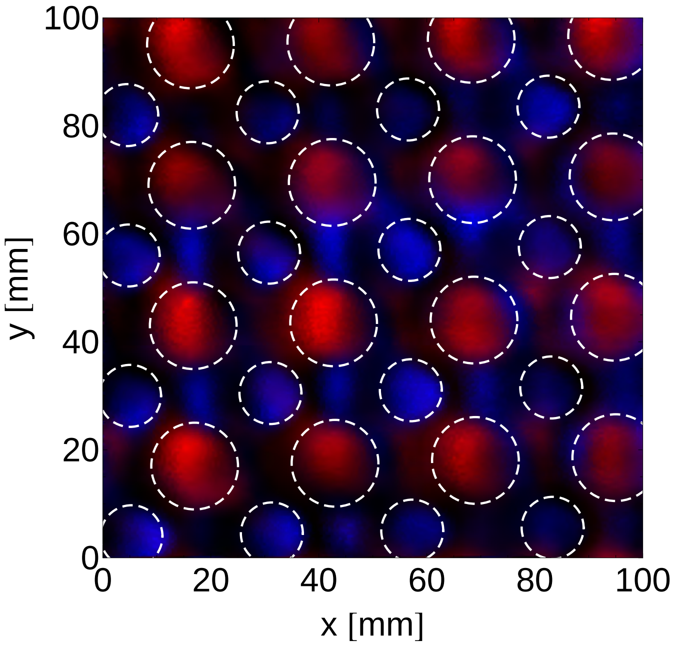

Figure 9.13: Pseudo-color plot of the electric field (component along polarization direction) measured 1 mm above the metamaterial. The red (blue) color corresponds to the 8.1 GHz (9.25 GHz) resonances, which are overlayed to see the photon sorting. The dashed circles are the approximate edges of the cavities below.

of field strengths above the cavities, and estimate the splitting efficiency by

$$SE_n \approx \frac{F_n}{F_T}, \tag{9.3}$$

where F_n is the field strength above a cavity and $F_T = F_1 + F_2$ is the total field strength. Figures 9.14(a) and (b) show the average field strength (line) along lines crossing the large and small cavities. The standard deviation of these values are shown in the shaded region. The ratio of relative field strengths is shown in Fig. 9.14(c) and the measured, approximate splitting efficiency is

Frequency (GHz)	Simulated splitting efficiency (%)	Measured approximate splitting efficiency (%)
8.1	96	98
9.25	93	92

Table 9.4: Comparison of the simulated and measured approximate splitting efficiencies.

shown in Fig. 9.14(d). Using this approach, and averaging over a few peaks, gives an estimated splitting efficiency of 98% (92%) at 8.1 GHz (9.25 GHz). These values compare favorably to the calculated values from simulation, see Table 9.4. The estimated SE is higher at 9.25 GHz, as this is a measure of field strength, not directly of the absorption; although the fields are higher above the smaller cavity, the absorption may be lower. Additionally, the value of the SE at this frequency is less precise due to the experimental artifact. Thus, this is an experimental verification of the photon sorting mechanism described throughout this thesis.

9.4 A path towards an optical device

Modifying a device which operates at microwave frequencies to operate optical frequencies primarily consists of scaling down all the dimensions of the device. However, for all the reasons discussed elsewhere in this thesis (i.e. changing metal properties, fabrication limitations, etc.) there are additional

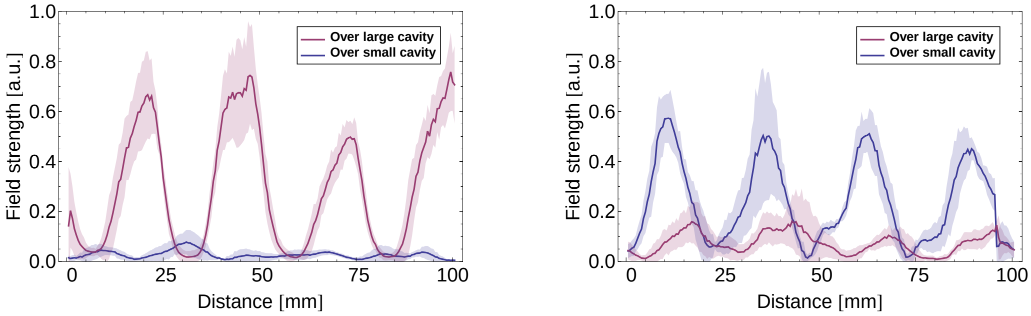

(a) Field strength on a line crossing the large and small cavities at 8.1 GHz.

(b) Field strength on a line crossing the large and small cavities at 9.25 GHz.

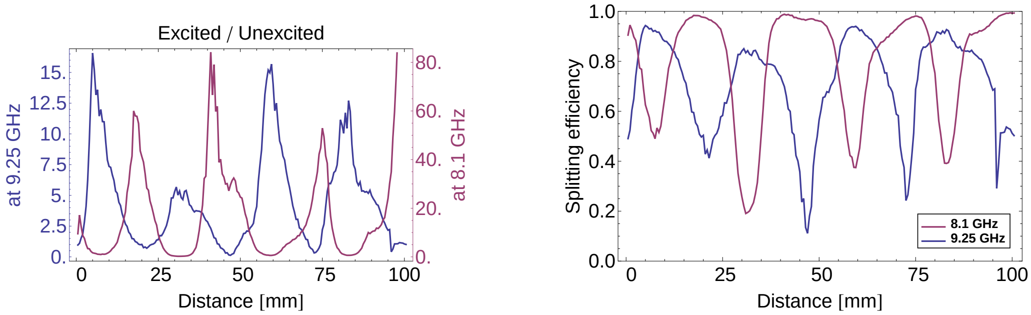

(c) The ratio of the field strength above the excited cavity to the strength above the unexcited cavity.

(d) Splitting efficiency estimated using ratios of field strength.

Figure 9.14: Experimental measurement of light splitting using field strength above the cavities.

complications. We outline some of these issues, and discuss some methods of overcoming them.

Firstly, the cavity resonances should ideally be below diffraction. As discussed in Section 4.3, the coupling of incident fields to the cavity is via the evanescent scattered modes, thus any propagating diffracted mode inherently decreases the energy available to the cavity by carrying the fields away from the metamaterial. Operating at optical frequencies requires a fairly small pitch, typically less than 450 nm, and smaller if there is a dielectric layer above the metamaterial. Therefore, in order to have multiple cavities per unit cell, they must be filled with a high dielectric, thereby increasing the effective cavity size. These dielectrics, however, must be highly transparent at optical frequencies to minimize absorption in the dielectric; generally different materials are required in the IR and visible regimes.

These small sizes require advanced lithography techniques. Nevertheless, unlike rectangles or L-shapes, cylinders can be fabricated, see Fig. 9.15, and their radii can be accurately controlled. In this approach, the dielectric – in this case, amorphous silicon (a-Si) – is patterned and etched, and metal – in this case, gold – is electroplated to create the film. A device using a-Si would operate in the IR regime; this method will also work with titanium dioxide dielectrics for a visible regime device.

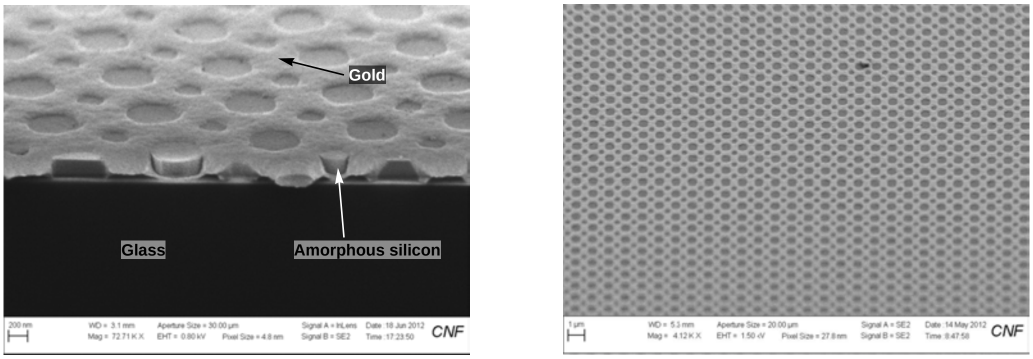

(a) Close-up, cross-section view of a fabricated structure.

(b) Large-scale view of a fabricated structure.

Figure 9.15: Fabricated nano-scale dielectric cylinders in a gold film. Cavity radii can be accurately controlled.

As discussed many times in this thesis, metals at optical frequencies can be quite lossy. For a device designed to merely absorb light, this may be a feature. However, if the absorption is to occurs preferentially within a particular cavity this serves as a detriment. Ultimately, there are very few things that can be done to overcome this problem. Any light splitting device which operates at optical frequencies will have an intrinsic loss due to metal absorption which will effect overall transmission or preferred absorption.

For example, consider a near-IR photon sorting transmission array (i.e. open aperture), with a periodicity of $\Lambda = 500$ nm, and the two apertures filled with a-Si embedded through a gold film of thickness $h = 200$ nm, with aperture radii of $a_1 = 145$ nm and $a_2 = 66$ nm. Figure 9.16 shows a plot of the reflection from, transmission through, and calculated loss in this structure,

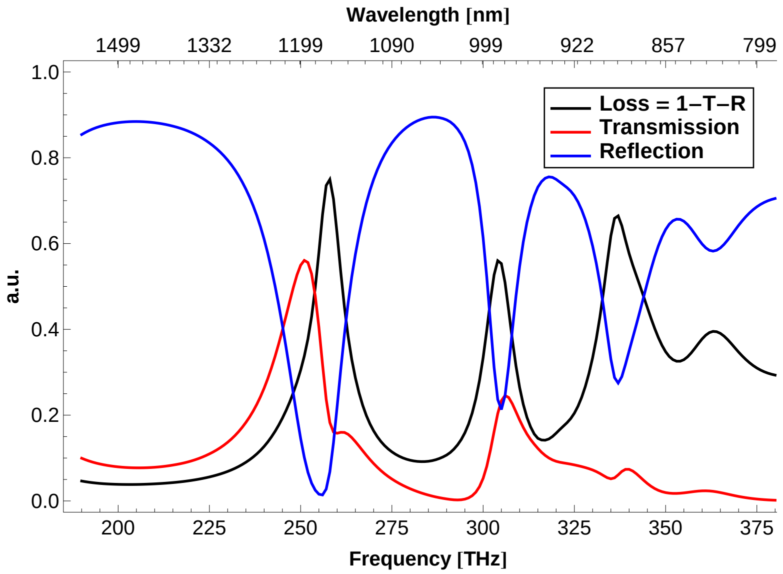

Figure 9.16: Reflection from, transmission through, and loss in a simulated IR transmission structure.

with light incident through a fused silica superstrate (in fabrication the fused silica acts as a substrate). Where there are peaks in transmission, there are also peaks in absorption.

Nevertheless, this transmission is localized, with light exiting different holes at different frequencies. Figure 9.17 shows a plot of the z-component of the Poynting vector at the bottom surface of the film, and photon sorting is clearly seen by the relative strength of the power flow through each cavity. However, although this structure demonstrates very strong coupling to incident light (99% [79%] at 252 THz [306 THz]), the transmission is quite low (56% [25%] at 252 THz [306 THz]). This is due to losses in the metal,

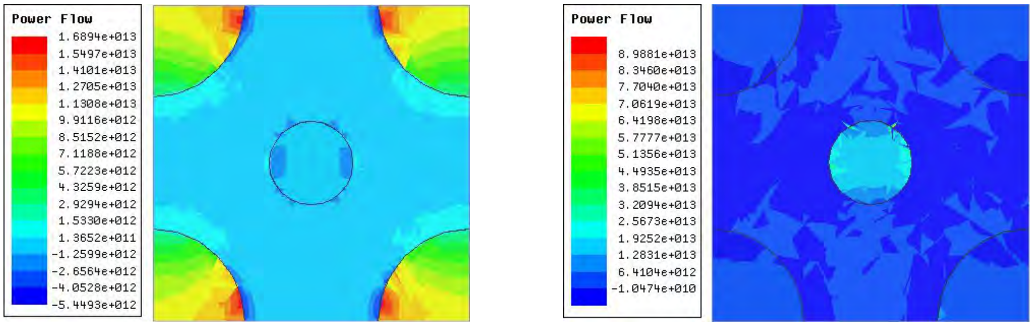

(a) Power flow through the bottom of the film at 252 THz.

(b) Power flow through the bottom of the film at 306 THz.

Figure 9.17: Simulated power flow at the exit (bottom) of the metal film at the two peaks in transmission: 252 THz (a) and 306 THz (a). Photon sorting is seen by the strength of the power flow through each cavity.

which can be seen by looking at the volume loss density plotted in various regions, see Fig. 9.18. At both of these frequencies, the loss is entirely within the metallic regions of the structure.

Specific considerations for a solar cell

Additional complications arise when using these devices in a horizontally-oriented, multi-junction solar cell. Ideally, the different junctions of this cell should be connected in parallel. This requires all of the cavities of one size to be electrically isolated from the cavities of other sizes. One possible route to achieve this is by running metal strips below the cavities, isolated from the adjacent strips and the upper metamaterial layer, via a dielectric (such as silicon dioxide, which has a high dielectric breakdown voltage). Figure 9.19

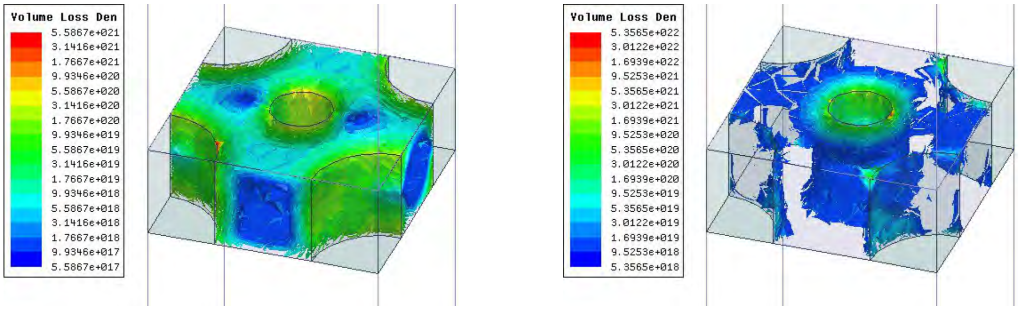

(a) Regions of energy loss at 252 THz. (b) Regions of energy loss at 306 THz.

Figure 9.18: Volume loss density in the simulated IR transmission structure is plotted on a log scale at the two peaks in transmission: 252 THz (a) and 306 THz (a). The loss is entirely in the metallic regions of the structure.

a schematic cross-section illustration of the proposed structure and an SEM image of a proof-of-concept fabrication attempt. Careful alignment of the structures are necessary, but this should be achievable within the tolerances of existing fabrication capabilities. In this structure the absorbing compounds would be fixed at the bottom of the cavities. One potential disadvantage of this approach, therefore, is the decreased volume over which absorption occurs.

9.5 Conclusions and outlook

We have demonstrated the capability of a compound subwavelength cavity array to spatially split, concentrate and absorb microwave radiation, with extremely high efficiency and concentrations. This response is polarization

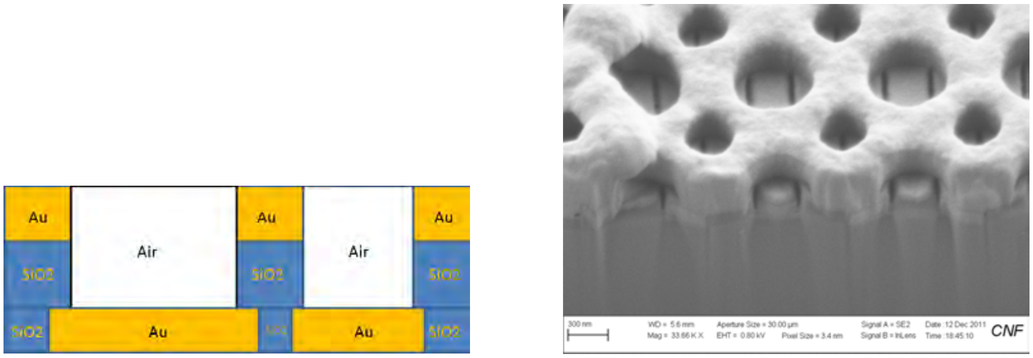

(a) Cross-section schematic of contact isolation. The top gold is the metamaterial; the bottom gold makes the electrical contact.

(b) Fabricated proof-of-concept device.

Figure 9.19: One possible approach for electrical isolation.

independent for shallow angles. This structure can also, in principle, be extended to absorb additional bands by including additional cavities in each unit cell, as long as the periodicity can stay small. With higher values of the real portion of the cavity dielectric it is possible to decrease the cavity radii while maintaining the resonance location. This would allow additional cavities to be added, without sacrificing the sub-diffraction periodicity. Furthermore, this device could be improved by shifting the modes further down in frequency, or by reducing the pitch.

Although this structure was designed to operate in the microwave regime, with appropriate scaling it can be adjusted to other wavelength ranges, where it has applications in multi-junction solar energy absorption. For optical frequencies, however, there are additional difficulties to overcome, including fabrication limitations and increased metal loss. Other structures with narrower bandwidth absorption peaks and more absorption peaks are possible and may be useful in developing multi-wavelength microbolometers or photodetectors.

Bibliography

[1] S. John. Strong localization of photons in certain disordered dielectric superlattices. *Phys. Rev. Lett.*, 58:2486–2489, June 1987.

[2] E. Yablonovitch. Inhibited spontaneous emission in solid-state physics and electronics. *Phys. Rev. Lett.*, 58:2059–2062, May 1987.

[3] R. A. Shelby, D. R. Smith, S. C. Nemat-Nasser, and S. Schultz. Microwave transmission through a two-dimensional, isotropic, left-handed metamaterial. *Appl. Phys. Lett.*, 78(4):489–491, 2001.

[4] R. A. Shelby, D. R. Smith, and S. Schultz. Experimental verification of a negative index of refraction. *Science*, 292(5514):77–79, 2001.

[5] Q. Zhao, L. Kang, B. Du, B. Li, J. Zhou, H. Tang, X. Liang, and B. Zhang. Electrically tunable negative permeability metamaterials based on nematic liquid crystals. *Appl. Phys. Lett.*, 90(1):011112, 2007.

[6] S. Xiao, U. K. Chettiar, A. V. Kildishev, V. Drachev, I. C. Khoo, and V. M. Shalaev. Tunable magnetic response of metamaterials. *Appl. Phys. Lett.*, 95(3):033115, 2009.

[7] D. Schurig, J. J. Mock, B. J. Justice, S. A. Cummer, J. B. Pendry, A. F. Starr, and D. R. Smith. Metamaterial electromagnetic cloak at microwave frequencies. *Science*, 314(5801):977–980, 2006.

[8] W. Cai, U. K. Chettiar, A. V. Kildishev, and V. M. Shalaev. Optical cloaking with metamaterials. *Nat. Photon.*, 1(4):224–227, April 2007.

[9] M. Yan, Z. Ruan, and M. Qiu. Scattering characteristics of simplified cylindrical invisibility cloaks. *Opt. Express*, 15(26):17772–17782, December 2007.

[10] J. Valentine, J. Li, T. Zentgraf, G. Bartal, and X. Zhang. An optical cloak made of dielectrics. *Nat. Mater.*, 8(7):568–571, July 2009.

[11] D. Crouse, E. Jaquay, A. Maikal, and A. P. Hibbins. Light circulation and weaving in periodically patterned structures. *Phys. Rev. B*, 77(19):195437, May 2008.

[12] M. Bayindir, B. Temelkuran, and E. Ozbay. Photonic-crystal-based beam splitters. *Appl. Phys. Lett.*, 77(24):3902–3904, 2000.

[13] N. Wongkasem and A. Akyurtlu. Light splitting effects in chiral metamaterials. *Journal of Optics*, 12(3):035101, 2010.

[14] J. B. Pendry. Negative refraction makes a perfect lens. *Phys. Rev. Lett.*, 85:3966–3969, October 2000.

[15] A. Grbic and G. V. Eleftheriades. Overcoming the diffraction limit with a planar left-handed transmission-line lens. *Phys. Rev. Lett.*, 92:117403, March 2004.

[16] W. Cai, D. A. Genov, and V. M. Shalaev. Superlens based on metal-dielectric composites. *Phys. Rev. B*, 72:193101, November 2005.

[17] T. W. Ebbesen, H. J. Lezec, H. F. Ghaemil, T. Thiol, and P. A. Wolff. Extraordinary optical transmission through sub-wavelength hole arrays. *Nature*, 391(6668):667–669, February 1998.

[18] *Encyclopædia Britannica Online*. United States Bullion Depository: gold storage. [Photograph]. Accessed: July 2012.

[19] Image. Freedigitalphotos.net.

[20] J. C. Lansey. Gateway arch, June 2012.

[21] E. Lansey, N. Pishbin, J. N. Gollub, and D. T. Crouse. Analytical analysis of the resonance response of subwavelength nanoscale cylindrical apertures in metal at near-ultraviolet, optical, and near-infrared frequencies. *J. Opt. Soc. Am. B*, 29(3):262–267, March 2012.

[22] E. Lansey, J. N. Gollub, and D. T. Crouse. Dispersion analysis of subwavelength square apertures at optical frequencies. *Physics and Simulation of Optoelectronic Devices XX*, 8255(1):82550R, 2012.

[23] E. Lansey, J. Gollub, T. L. James, and D. T. Crouse. A polarization-independent wavelength-tuned metamaterial for solar energy applications. In *OSA Technical Digest (CD)*, page PWD2. Optical Society of America, November 2011.

[24] J. Jackson. *Classical Electrodynamics.* John Wiley & Sons, Inc., 2nd edition, 1975.

[25] N. W. Ashcroft and N. D. Mermin. *Solid State Physics.* Brooks Cole, 1st edition, 1976.

[26] M. A. Ordal, R. J. Bell, J. R. W. Alexander, L. L. Long, and M. R. Querry. Optical properties of fourteen metals in the infrared and far infrared: Al, Co, Cu, Au, Fe, Pb, Mo, Ni, Pd, Pt, Ag, Ti, V, and W. *Appl. Opt.*, 24(24):4493–4499, December 1985.

[27] S. Kawata and V. M. Shalaev, editors. *Tip Enhancement.* Elsevier Science, 2007.

[28] L. Novotny and C. Hafner. Light propagation in a cylindrical waveguide with a complex, metallic, dielectric function. *Phys. Rev. E*, 50:4094–4106, November 1994.

[29] H. Shin, P. B. Catrysse, and S. Fan. Effect of the plasmonic dispersion relation on the transmission properties of subwavelength cylindrical holes. *Phys. Rev. B*, 72:085436, August 2005.

[30] P. B. Catrysse and S. Fan. Propagating plasmonic mode in nanoscale apertures and its implications for extraordinary transmission. *Journal of Nanophotonics*, 2:021790, 2008.

[31] A. Sudbo. Why are accurate computations of mode fields in rectangular dielectric waveguides difficult? *J. Lightwave Technol.*, 10(4):418 –419, April 1992.

[32] G. R. Hadley. High-accuracy finite-difference equations for dielectric waveguide analysis II: Dielectric corners. *J. Lightwave Technol.*, 20(7):1219, July 2002.

[33] P. Lalanne, C. Sauvan, and J. Hugonin. Photon confinement in photonic crystal nanocavities. *Laser & Photonics Reviews*, 2(6):514–526, 2008.

[34] H. Lezec and T. Thio. Diffracted evanescent wave model for enhanced and suppressed optical transmission through subwavelength hole arrays. *Opt. Express*, 12(16):3629–3651, August 2004.

[35] F. J. García-Vidal, L. Martín-Moreno, T. W. Ebbesen, and L. Kuipers. Light passing through subwavelength apertures. *Rev. Mod. Phys.*, 82(1):729–787, March 2010.

[36] F. J. García-Vidal and L. Martín-Moreno. Transmission and focusing of light in one-dimensional periodically nanostructured metals. *Phys. Rev. B*, 66(15):155412, October 2002.

[37] R. Ulrich and M. Tacke. Submillimeter waveguiding on periodic metal structure. *Appl. Phys. Lett.*, 22(5):251–253, 1973.

[38] H. A. Bethe. Theory of diffraction by small holes. *Phys. Rev.*, 66(7-8):163–182, October 1944.

[39] R. Gordon. Bethe's aperture theory for arrays. *Phys. Rev. A*, 76(5):053806, November 2007.

[40] F. J. García de Abajo and J. J. Sáenz. Electromagnetic surface modes in structured perfect-conductor surfaces. *Phys. Rev. Lett.*, 95:233901, November 2005.

[41] H. F. Ghaemi, T. Thio, D. E. Grupp, T. W. Ebbesen, and H. J. Lezec. Surface plasmons enhance optical transmission through subwavelength holes. *Phys. Rev. B*, 58:6779–6782, September 1998.

[42] A. Krishnan, T. Thio, T. J. Kim, H. J. Lezec, T. W. Ebbesen, P. A. Wolff, J. Pendry, L. Martin-Moreno, and F. J. Garcia-Vidal. Evanescently coupled resonance in surface plasmon enhanced transmission. *Opt. Commun.*, 200(1-6):1 – 7, 2001.

[43] J. B. Pendry, L. Martn-Moreno, and F. J. Garcia-Vidal. Mimicking surface plasmons with structured surfaces. *Science*, 305(5685):847–848, 2004.

[44] D. Crouse and P. Keshavareddy. Role of optical and surface plasmon modes in enhanced transmission and applications. *Opt. Express*, 13(20):7760–7771, October 2005.

[45] H. Liu and P. Lalanne. Microscopic theory of the extraordinary optical transmission. *Nature*, 452(7188):728–731, April 2008.

[46] F. J. Garcia-Vidal, L. Martin-Moreno, T. W. Ebbesen, and L. Kuipers. Light passing through subwavelength apertures. *Rev. Mod. Phys.*, 82(1):729–, March 2010.

[47] K. J. K. Koerkamp, S. Enoch, F. B. Segerink, N. van Hulst, and L. Kuipers. Strong influence of hole shape on extraordinary transmission through periodic arrays of subwavelength holes. *Phys. Rev. Lett.*, 92(18):183901, May 2004.

[48] K. van der Molen, K. J. K. Koerkamp, S. Enoch, F. B. Segerink, N. F. van Hulst, and L. Kuipers. Role of shape and localized resonances in extraordinary transmission through periodic arrays of subwavelength holes: Experiment and theory. *Phys. Rev. B: Condens. Matter Mater. Phys.*, 72(4):045421, 2005.

[49] T. Thio, H. F. Ghaemi, H. J. Lezec, P. A. Wolff, and T. W. Ebbesen. Surface-plasmon-enhanced transmission through hole arrays in cr films. *J. Opt. Soc. Am. B*, 16(10):1743–1748, October 1999.

[50] M. Sarrazin and J.-P. Vigneron. Optical properties of tungsten thin films perforated with a bidimensional array of subwavelength holes. *Phys. Rev. E*, 68:016603, July 2003.

[51] R. Gordon and A. Brolo. Increased cut-off wavelength for a subwavelength hole in a real metal. *Opt. Express*, 13(6):1933–1938, March 2005.

[52] Z. Ruan and M. Qiu. Enhanced transmission through periodic arrays of subwavelength holes: The role of localized waveguide resonances. *Phys. Rev. Lett.*, 96(23):233901, June 2006.

[53] S. Collin, F. Pardo, and J.-L. Pelouard. Waveguiding in nanoscale metallic apertures. *Opt. Express*, 15(7):4310–4320, April 2007.

[54] L. Moreno and F. García-Vidal. Optical transmission through circular hole arrays in optically thick metal films. *Opt. Express*, 12(16):3619–3628, August 2004.

[55] V. Delgado, R. Marqués, and L. Jelinek. Analytical theory of extraordinary optical transmission through realistic metallic screens. *Opt. Express*, 18(7):6506–6515, March 2010.

[56] A. D. Papadopoulos and E. N. Glytsis. Optical waveguide grating couplers: 2nd-order and 4th-order finite-difference time-domain analysis. *Appl. Opt.*, 48(27):5164–5175, September 2009.

[57] I. Bendoym, N. Pishbin, E. Lansey, and D. T. Crouse. Rapidly optimizing optoelectronic devices using full wave 3d simulation software. *Physics and Simulation of Optoelectronic Devices XIX*, 7933:793327, 2011.

[58] Y. Takakura. Optical resonance in a narrow slit in a thick metallic screen. *Phys. Rev. Lett.*, 86:5601–5603, June 2001.

[59] D. Crouse and P. Keshavareddy. Polarization independent enhanced optical transmission in one-dimensional gratings and device applications. *Opt. Express*, 15(4):1415–1427, 2007.

[60] D. Crouse, A. P. Hibbins, and M. J. Lockyear. Tuning the polarization state of enhanced transmission in gratings. *Appl. Phys. Lett.*, 92(19):191105, 2008.

[61] M. Gorkunov, E. Podivilov, and B. Sturman. Transmission and scattering properties of subwavelength slits in metals. *Phys. Rev. B*, 83:035414, January 2011.

[62] M. Guillaumée, L. A. Dunbar, and R. P. Stanley. Description of the modes governing the optical transmission through metal gratings. *Opt. Express*, 19(5):4740–4755, February 2011.

[63] Z. Fan, L. Zhan, X. Hu, and Y. Xia. Critical process of extraordinary optical transmission through periodic subwavelength hole array: Hole-assisted evanescent-field coupling. *Opt. Commun.*, 281(21):5467 – 5471, 2008.

[64] L. Li. New formulation of the fourier modal method for crossed surface-relief gratings. *J. Opt. Soc. Am. A*, 14(10):2758–2767, October 1997.

[65] A. Y. Nikitin, D. Zueco, F. J. García-Vidal, and L. Martín-Moreno. Electromagnetic wave transmission through a small hole in a perfect electric conductor of finite thickness. *Phys. Rev. B*, 78(16):165429–, October 2008.

[66] E. Popov, M. Nevire, S. Enoch, and R. Reinisch. Theory of light transmission through subwavelength periodic hole arrays. *Phys. Rev. B*, 62(23):16100–16108, December 2000.

[67] S. Enoch, E. Popov, M. Neviere, and R. Reinisch. Enhanced light transmission by hole arrays. *Journal of Optics A: Pure and Applied Optics*, 4(5):S83, 2002.

[68] A. V. Kats, M. L. Nesterov, and A. Y. Nikitin. Polarization properties of a periodically-modulated metal film in regions of anomalous optical transparency. *Phys. Rev. B*, 72(19):193405–, November 2005.

[69] P. Lalanne, J. C. Rodier, and J. P. Hugonin. Surface plasmons of metallic surfaces perforated by nanohole arrays. *Journal of Optics A: Pure and Applied Optics*, 7(8):422, 2005.

[70] S. A. Darmanyan, M. Nevire, and A. V. Zayats. Analytical theory of optical transmission through periodically structured metal films via tunnel-coupled surface polariton modes. *Phys. Rev. B*, 70(7):075103–, August 2004.

[71] T. Senior. Impedance boundary conditions for imperfectly conducting surfaces. *Applied Scientific Research, Section B*, 8:418–436, 1960.

[72] Z. Godzinski. The surface impedance concept and the structure of radio waves over real earth. *Proceedings of the IEE - Part C: Monographs*, 108(14):362–373, 1961.

[73] S. Yuferev and N. Ida. Selection of the surface impedance boundary conditions for a given problem. *IEEE T. Magn.*, 35(3):1486–1489, 1999.

[74] D. Lay. *Linear Algebra and Its Applications.* Addison-Wesley, Reading, MA, 3rd edition, 2003.

[75] R. F. Harrington. *Field Computation by Moment Methods.* Wiley-IEEE Press, 1993.

[76] Ansys Inc. *HFSS Online Help*, May 2012.

[77] G. Beer, I. Smith, and C. Duenser. *The Boundary Element Method with Programming.* Springer, 2008.

[78] G. M. Hale and M. R. Querry. Optical constants of water in the 200-nm to 200-μm wavelength region. *Appl. Opt.*, 12(3):555–563, March 1973.

[79] J. C. Lansey. Glory, January 2005.

[80] R. Schoenberg. Optimization with the quasi-newton method. Technical report, Aptech Systems, Inc., Maple Valley, WA, 2001.

[81] I. Newton. *Methodus fluxionum et serierum infinitarum.* 1736.

[82] N. S. Lewis and D. G. Nocera. Powering the planet: Chemical challenges in solar energy utilization. *Proceedings of the National Academy of Sciences*, 103(43):15729–15735, 2006.

[83] B. O'Regan and M. Gratzel. A low-cost, high-efficiency solar cell based on dye-sensitized colloidal tio2 films. *Nature*, 353(6346):737–740, October 1991.

[84] R. D. McConnell. Assessment of the dye-sensitized solar cell. *Renewable and Sustainable Energy Reviews*, 6(3):271–293, September 2002.

[85] H.-J. Koo, S. T. Chang, J. M. Slocik, R. R. Naik, and O. D. Velev. Aqueous soft matter based photovoltaic devices. *J. Mater. Chem.*, 21(1):72–79, 2011.

[86] Y.-C. Hsu, H. Zheng, J. T'suen Lin, and K.-C. Ho. On the structural variations of Ru(II) complexes for dye-sensitized solar cells. *Solar Energy Materials and Solar Cells*, 87(1-4):357–367, May 2005.

[87] L. L. Kazmerski. Best research solar cell efficiencies. April 2011.

[88] A. Luque and S. Hegedus, editors. *Handbook of Photovoltaic Science and Engineering*. Wiley, 2003.

[89] Fraunhofer Institute for Solar Energy Systems. Structure of a multi-junction solar cell. January 2010.

[90] J. M. Román. State-of-the-art of III-V solar cell fabrication technologies, device designs and applications. In *Advanced Photovoltaic Cell Design*, 2004.

[91] A. Barnett, C. Honsberg, D. Kirkpatrick, S. Kurtz, D. Moore, D. Salzman, R. Schwartz, J. Gray, S. Bowden, K. Goossen, M. Haney, D. Aiken, M. Wanlass, and K. Emery. 50% efficient solar cell architectures and designs. In *Conference Record of the 2006 IEEE 4th World Conference on Photovoltaic Energy Conversion*, volume 2, pages 2560–2564, 2006.

[92] D. Kirkpatrick, E. Eisenstadt, and A. Haspert. DARPA's push for photovoltaics. In *Conference Record of the 2006 IEEE 4th World Conference on Photovoltaic Energy Conversion*, volume 2, pages 2556–2559, 2006.

[93] A. Barnett, D. Kirkpatrick, C. Honsberg, D. Moore, M. Wanlass, K. Emery, R. Schwartz, D. Carlson, S. Bowden, D. Aiken, A. Gray, S. Kurtz, L. Kazmerski, M. Steiner, J. Gray, T. Davenport, R. Buelow, L. Takacs, N. Shatz, J. Bortz, O. Jani, K. Goossen, F. Kiamilev, A. Doolittle, I. Ferguson, B. Unger, G. Schmidt, E. Christensen, and D. Salzman. Very high efficiency solar cell modules. *Progress in Photovoltaics: Research and Applications*, 17(1):75–83, 2009.

[94] J. Koch, A. A. Houck, K. L. Hur, and S. M. Girvin. Time-reversal-symmetry breaking in circuit-qed-based photon lattices. *Phys. Rev. A*, 82:043811, October 2010.

[95] G. Airy. On the diffraction of an object-glass with circular aperture. *Trans. Cambridge Philos. Soc.*, 5:283–291, 1835.

[96] J. Huang, T.-K. Wu, and S.-W. Lee. Tri-band frequency selective surface with circular ring elements. *Antennas and Propagation, IEEE Transactions on*, 42(2):166 –175, February 1994.

[97] T.-K. Wu. Four-band frequency selective surface with double-square-loop patch elements. *Antennas and Propagation, IEEE Transactions on*, 42(12):1659 –1663, December 1994.

[98] M. Ohira, H. Deguchi, M. Tsuji, and H. Shigesawa. Multiband single-layer frequency selective surface designed by combination of genetic algorithm and geometry-refinement technique. *Antennas and Propagation, IEEE Transactions on*, 52(11):2925 – 2931, November 2004.

[99] T. Shegai, S. Chen, V. D. Miljkovic, G. Zengin, P. Johansson, and M. Kall. A bimetallic nanoantenna for directional colour routing. *Nat Commun*, 2:481, September 2011.

[100] E. Laux, C. Genet, T. Skauli, and T. W. Ebbesen. Plasmonic photon sorters for spectral and polarimetric imaging. *Nat Photon*, 2(3):161–164, March 2008.

[101] D. Crouse. Numerical modeling and electromagnetic resonant modes in complex grating structures and optoelectronic device applications. *IEEE Trans Electron Devices*, 52(11):2365 – 2373, November 2005.

[102] D. Crouse and P. Keshavareddy. A method for designing electromagnetic resonance enhanced silicon-on-insulator metalsemiconductormetal photodetectors. *Journal of Optics A: Pure and Applied Optics*, 8(2):175, 2006.

[103] J. D. Edmunds, E. Hendry, A. P. Hibbins, J. R. Sambles, and I. J. Youngs. Multi-modal transmission of microwaves through hole arrays. *Opt. Express*, 19(15):13793–13805, July 2011.

[104] F. I. Baida. Spatiotemporal sub-wavelength near-field light localization. *Opt. Express*, 18(14):14812–14819, July 2010.

[105] A. P. Hibbins, J. R. Sambles, C. R. Lawrence, and J. R. Brown. Squeezing millimeter waves into microns. *Phys. Rev. Lett.*, 92(14):143904–, April 2004.

[106] J. S. White, G. Veronis, Z. Yu, E. S. Barnard, A. Chandran, S. Fan, and M. L. Brongersma. Extraordinary optical absorption through subwavelength slits. *Opt. Lett.*, 34(5):686–688, March 2009.

[107] J. Le Perchec, Y. Desieres, N. Rochat, and R. E. de Lamaestre. Subwavelength optical absorber with an integrated photon sorter. *Appl. Phys. Lett.*, 100(11):113305–4, March 2012.

[108] T. Li, H. Liu, S.-M. Wang, X.-G. Yin, F.-M. Wang, S.-N. Zhu, and X. Zhang. Manipulating optical rotation in extraordinary transmission by hybrid plasmonic excitations. *Appl. Phys. Lett.*, 93(2):021110, 2008.

[109] T. Li, S. M. Wang, J. X. Cao, H. Liu, and S. N. Zhu. Cavity-involved plasmonic metamaterial for optical polarization conversion. *Appl. Phys. Lett.*, 97(26):261113, 2010.

[110] J. Zhang, J.-Y. Ou, N. Papasimakis, Y. Chen, K. F. MacDonald, and N. I. Zheludev. Continuous metal plasmonic frequency selective surfaces. *Opt. Express*, 19(23):23279–23285, November 2011.

[111] A. M. Nicolson and G. F. Ross. Measurement of the intrinsic properties of materials by time-domain techniques. *Instrumentation and Measurement, IEEE Transactions on*, 19(4):377 –382, November 1970.

[112] W. Weir. Automatic measurement of complex dielectric constant and permeability at microwave frequencies. *Proc. IEEE*, 62(1):33 – 36, January 1974.